UNIVERSITY OF CALIFORNIA, SAN DIEGO

Hollow Nanoshells for Cancer Diagnostics and Therapy

A dissertation submitted in partial satisfaction of the

requirements for the degree

Doctor of Philosophy

in

Bioengineering

by

Sergio Sandoval

Committee in charge:

Professor Andrew C. Kummel, Chair
Professor Michael J. Heller, Co-Chair
Professor Xiaohua Huang
Professor William C. Trogler
Professor Liangfang Zhang

2012

The dissertation of Sergio Sandoval is approved, and it is acceptable in quality and form for publication on microfilm and electronically:

Co-Chair

Chair

University of California, San Diego

2012

DEDICATION

To my mom

.

EPIGRAPH

“ Be silent, or say something better than silence.”

Pythogoras

TABLE OF CONTENTS

Signature Page iii

Dedication iv

Epigraph v

Table of Contents vi

List of Abbreviations and Symbols xii

List of Figures xiii

List of Tables xviii

Acknowledgements xx

Vita xxii

Abstract of the Disseration xxiv

Chapter 1. Introduction 1

1.1 Nanoparticles in Biomedical Field 1

1.2 Silica Nanoparticles 1

1.3 Titania Nanoparticles 2

1.4 Rare Earth Ions as Luminescent Reporters for Nanoparticles 3

1.5 Silica and Titania as a Europium Ion Host 3

1.6 Europium Doped Silica Nanoshells 4

1.7 Europium Doped Titania Nanoshells 5

1.8 Reasoning for Nanoparticle Encapsulation and Targeting 5

1.9 Folate as a Cancer Targeting Ligand 6

1.10 Previous Work on Quantification of Cellular Uptake and Surface Adhesion of Nanoparticles 7

1.11 Quantification of Folate Targeted Nanoshell Cell Interations by Performing a Novel Fluorescent Ratio Analysis on Captured Microscopy Images 8

1.12 Acknowledgments 8

1.13 References 8

Chapter 2. Red-luminescent Europium (III) Doped Silica Nanoshells: Synthesis, Characterization and Their Interaction with HeLa Cells 20

2.1 Introduction 20

2.2 Experimental Methods and Materials 22

2.2.1 Materials 22

2.2.2 Preparation of Europium Doped Silica Nanoshells (NS) 22

2.2.3 Characterization of Silica Nanoshells (NS) 23

2.2.4 Cell Culture 23

2.2.5 Cell Adhesion/Endocytosis Experiments 23

2.2.6 Two-Photon (2-P) Microscopy of Silica Nanoshells Engaging HeLa Cells in vitro 24

2.3 Results and Discussion 24

2.3.1 Synthesis of Eu-SiO_2 Nanoshells 24

2.3.2 Optical Properties 27

2.3.3 Dynamic Light Scattering (DLS) and Zeta potential Measurements 27

2.3.4 Adhesion/Endocytosis Experiments and Image Analysis 29

2.4 Conclusions 33

2.5 Acknowledgements 34

2.6 References 34

Chapter 3. Europium Doped TiO_2 Hollow Nanoshells: Two-Photon Imaging of Cell Binding 38

3.1 Introduction 38

3.2 Experimental Methods and Materials 41

3.2.1 Materials 41

3.2.2 Preparation of Europium-Doped Hollow Titania Nanoshells 41

3.2.3 Modification of Eu/TiO_2 Hallow Nanoshells with Poly(ethylenimine) 42

3.2.4 Characterization of Eu/TiO_2 Hallow Nanoshells 42

3.2.5 Cell Culture 42

3.2.6 Cell Adhesion/Endocytosis Experiments 43

3.2.7 Two-Photon (2-P) Microscopy of HeLa Cell Interactions with Europium-Doped Nanoshells *In Vitro* 43

3.3 Results and Discussion 44

3.3.1 Synthesis of Eu^{3+}-Doped Hollow Titania Nanoshells 44

3.3.2 Electron Microscopy and Dynamic Light Scattering Measurements 47

3.3.3 X-Ray Diffraction Measurements 50

3.3.4 Optical Properties 51

3.3.5 Endocytosis Experiments 53

3.4 Conclusion 58

3.5 Acknowledgements 58

3.6 References 59

Chapter 4. Targeting of Cervical Cancer Cells using Folate Functionalized SiO_2 Hollow Nanoshells 68

4.1 Introduction 68

4.2 Experimental Methods 71

4.2.1 Materials 71

4.2.2 Preparation of Hollow Silica Nanoshells 71

4.2.3 Preparation of NHS-Folate and NHS-mPEG 72

4.2.4 Amine Surface Functionalization of SiO_2 Hollow Nanoshells with APTES 72

4.2.5 Surface Modification of SiO_2 Hollow Nanoshells with FITC-Isothiocynate and NHS-Folate or NHS-mPEG 72

4.2.6 Characterization of Functionalized SiO_2 Hollow Nanoshells 73

4.2.7 Cell Culture – HeLa Cell Only Samples..... 73

4.2.8 Cell Culture – Nanoshell Selectivity Experiments 74

4.2.9 Cell Adhesion/Endocytosis Experiments 74

4.2.10 Fluorescence Microscopy of Nanoshell Cell Adhesion..... 75

4.2.11 Confocal Microscopy of Nanoshell Uptake by HeLa Cells 75

4.3 Results/Discussion 75

4.3.1 Characterization of Functionalized SiO_2 Hollow Nanoshell 75

4.3.2 Quantification of Maximum Amount of Folate on NS Surfaces 79

4.3.3 NS HeLa Cell Adhesion Experiments and Fluorescent Microscopy Image Analysis 81

4.3.4 NS HeLa Cell Adhesion Experiments and Fluorescent Microscopy Image Analysis 85

4.3.5 NS Selectivity Experiments and Image Analysis 91

4.4 Conclusions 94

4.5 Acknowledgments 95

4.6 References 96

Chapter 5. Conclusions and Future Directions 102

5.1 Conclusions 102

5.1.1 Europium Doped Silica NS 102

5.1.2 Europium Doped Titania NS 102

5.1.3 Folate Functionalized Silica NS 103

5.2 Future Directions 104

5.2.1 NS Payload Encapsulation and Possible Drug Delivery Peripheral Instrumentation 104

5.2.2 Folate Functionalization of Titania NS 104

5.2.3 Folate NS Targeting In Vivo Properties 104

5.2.4 Incorporation of Iron Oxide in NS Structure for Potential Use Magnetic Therapy 105

5.3 References 105

LIST OF ABBREVIATIONS AND SYMBOLS

APS	Amino Polystyrene
CMFDA	5-Chloromethylfluorescein Diacetate
DLS	Dynamic Light Scattering
EDS	Energy Dispersive X-Ray Spectroscopy
PEI	Polyethyleneimine
NS	Nanoshell
SEM	Scanning Electron Microscope
TEM	Transmission Electron Microscope

LIST OF FIGURES

Figure 2.1: SEM and TME images of europium doped silica nanoshells from 200 nm (a) and 100 nm (b) APS templates with europium of 0.54% mole and 1.35% mole, respectively. Scale bars in SEM and TEM images are 200 nm. 25

Figure 2.2: Excitation (A) and emission (B) of 100 nm silica nanoshells, europium silica nanoshells (doped with 1.35% mole europium), and europium silica nanoshells surfaced functionalized with PEI. 27

Figure 2.3: Adhesion/Endocytosis Imaging of Eu-SiO_2 NS on HeLa Cells. HeLa cells, stained with CMFDA (green), appear to have a red ring of NS around their cellular membrane when incubated with Eu-SiO_2-PEI NS (red) for 24 hrs [Panel A]. Results were confirmed by performing a background subtraction on samples incubated with [Panel C] and without [Panel D] Eu-SiO_2-PEI NS. 30

Figure 2.4: Fluorescent intensity ratio analysis of adhesion/endocytosis experiments. Panel (a), shows outline areas just outside [(a)-2 and (a)-3] or inside [(a)-4 and (a)-5] HeLa cells for a typical control sample, while Panel (b), shows similar outlines for cells incubated with Eu-SiO_2-PEI NS. Outlines on individual images that were used to determine the red to green mean luminescence ratios for each sample set are shown. The average emission intensity ratio of areas just outside the cell membrane wall was typically 223% more luminescently intense for samples incubated with Eu-SiO_2-PEI NS, when compared to HeLa cells controls stained only with CMFDA. All outlines were based on the location of the green cytoplasmic cell stain images. 33

Figure 3.1: SEM and TEM Images of 200 nm plain and europium-doped titania nanoshells prepared using 0.025% $Eu(NO_3)_3 \cdot 5H_2O$. A: SEM images of amino polystyrene templates, B: Nondoped TiO_2 core-shells, C: Plain TiO_2 hollow NS, D: Eu^{3+}-doped TiO_2 core-shells, and E: Eu^{3+}-doped TiO_2 hollow NS. Small amounts of broken shells in the europium-doped image are identified by black arrows in E;

F: TEM image of europium-doped TiO_2 hollow NS showing some colloidal TiO_2 fused onto the outer NS surface; G: EDS spectrum analysis of Eu^{3+}-doped TiO_2 hollow NS showing X-rays characteristic of both Ti and Eu. 45

Figure 3.2: X-ray Diffraction Patterns of Thin Films of Plain and Eu^{3+} Doped TiO_2 Hollow Nanoshells. The percentages shown are the mass percent of $Eu(NO_3)_3 \cdot 5H_2O$ used during the sol-gel synthesis. 51

Figure 3.3: Photoluminescence Spectra of Eu3+ Doped Core-shell and Hollow Nanoshells. The percentages showed in legend are the mass percent of $Eu(NO_3)_3 \cdot 5H_2O$ used during the sol-gel synthesis. 52

Figure 3.4: Two-Photon Microscopy Images of Non-Doped and Eu Doped 200 nm TiO_2 Nanoshells Incubated with HeLa Cells. A: HeLa cells, stained with CMFDA (green) dye; B: HeLa cells incubated with 500 μg/mL of undoped TiO_2 PEI-coated NSs for 24 h; C: HeLa cells incubated with 500 μg/mL of Eu-TiO_2-PEI NS (red) for 24 h (0.025% $Eu(NO_3)_3 \cdot 5H_2O$). Identical settings and gains were used across all microscopy images. 54

Figure 3.5: Imaging of 200 nm Eu-doped TiO_2 Nanoshells Adhering to HeLa Cells. Two-photon dual colored captured images of cell only samples (Panel 1) and cell samples incubated with 500μg/mL of TiO_2-PEI NS (Panel 2) or Eu-TiO2-PEI NS (Panel 3), were split into their individual green and red image components (1.b/1.c, 2.b/2.c, and 3.b/3.c) and a background subtraction between these images was performed (1d, 2d, 3d) using Image J. 55

Figure 3.6: Luminescence Intensity Ratio Analysis of Nanoshell Cell Adhesion/Endocytosis from Figure 5. Panel 1: Green and red channel images of outlines of areas just outside (1b and 1c) or inside (1d and 1e) HeLa cells for a control sample. Panel 2: Corresponding image outlines for cells incubated with 200 nm Eu-TiO2-PEI NSs. All outlines were based on the location of the green

cytoplasmic cell stain images and used to calculate the fluorescence ratios in Table 3.4. 56

Figure 4.1: Schematic of Nanoshell (NS) Synthesis and Functionalization. Folate was used as a targeting ligand because folate receptor (FR) type α is frequently over-expressed in certain tumor cells and epithelial lineage tumors. Polyethylene glycol (PEG) was functionalized on the NS surface, at the same molar ratio as folate to NS, in order to have non-targeted, similar size, NS controls. 76

Figure 4.2: SEM Images of 100nm Nanoshells (NS) Functionalized with FITC, Folate, and/or PEG. No morphological differences can be seen before or after surface modification by SEM analysis. All SEM images were taken at 36,000x magnification. 79

Figure 4.3: Estimated Maximum Amount of Folate Molecules and Number of Folate Molecules Per nm^2 on a Nanoshell (NS). Supernatants used to functionalize NS with 20 or 200 ug of folate were collected. Using UV Vis, amount of folate molecules functionalized on NS surfaces was calculated. A: Average number of folate molecules functionalized on an individual NS. B: Average number of folate molecules per nm^2..... 80

Figure 4.4: Effect of Increasing Folate Targeting Ligand on SiO_2 NS on Cellular Adhesion/Endocytosis by Fluorescent Microscopy. A: HeLa cells stained with WGA membrane stain (Red) and Hoechst nuclear stain (Blue); B: HeLa cells incubated with 100 μg/mL of NS functionalized with 20 μg FITC (Green); C: HeLa cells incubated with 100 μg/mL of NS functionalized with 20 μg FITC and 2 μg Folate; D: HeLa cells incubated with 100 μg/mL of NS functionalized with 20 μg FITC and 20 μg Folate; E: HeLa cells incubated with 100 μg/mL of NS functionalized with 20 μg FITC and 200 μg Folate. Increase in green fluorescence around cells indicates increase in NS adhesion/endocytosis. 81

Figure 4.5: Comparison of Targeted and Non-Targeted Nanoshells (NS) Cell Adhesion/Endocytosis by Fluorescent Microscopy. HeLa cells were incubated with 100 μg/mL of targeted NS functionalized with (A.1) 20 μg FITC and 2 μg folate, (A.2) 20 μg FITC and 20 μg folate, (A.3) 20 μg FITC and 200 μg folate or non-targeted NS functionalized with (B.1) 20 μg FITC and 9 μg PEG, (B.2) 20 μg FITC and 90 μg PEG, or (B.3) 20 μg FITC and 900 μg PEG. All cells were stained with Hoescht and WGA. Average NS sizes were determined by DLS measurements. 83

Figure 4.6: Confocal Microscopy Cross Sectional Images of Endocytosed Nanoshells (NS) in HeLa Cancer Cells. A: Schematic depicting z-stack depth of consecutive confocal cross sections (B.1 to B.3) within HeLa cancer cells. B.1-B.3: A series of confocal microscopy images of HeLa cells, stained with WGA (Red) and Hoechst (Blue), incubated with 100 μg/mL of NS functionalized with 20 μg of FITC and 200 μg folate (Green), with arrows pointing to (B.1) top of cells, (B.2) proceeding cell cross section, or (B.3) cells at their center cross section. 85

Figure 4.7: Confocal Microscopy Center Cross Sectional Images of HeLa Cells Incubated with Targeted or Non-Targeted Nanoshells (NS). A: HeLa cells, stained with WGA (Red) and Hoechst (Blue); B: : HeLa cells incubated with 100 μg/mL of non-targeted NS functionalized with 20 μg FITC and 900 μg PEG; C: HeLa cells incubated with 100 μg/mL of targeted NS functionalized with 20 μg FITC and 200 μg folate; D: Same as (C) except with blue channel turned off. Identical settings and gains were used across all microscopy images. 86

Figure 4.8: Outlining HeLa Cells from Confocal Z-Stack Images. (A) - (D) A series of consecutive confocal images showing different cells being outlined at different z-stack planes. Each individual cell was outline only once at its center cross section, which was identified as the z-stack slice where an individual cell had its largest area. All outlines were based on the location of the red membrane stain images. 87

Figure 4.9: Fluorescent Microscopy Images of Differential Uptake of Non-Targeted and Targeted Nanoshells (NS) by HeLa and HFF-1 cells. A: HeLa cancer cells, stained with CMPTX (Red), and normal Human Forskin Fibroblast (HFF-1), stained with CMAC (Blue); B: HeLa and HFF-1 cells incubated with 50 μg/mL of non-targeted NS functionalized with 20 μg FITC and 900 μg PEG; C: HeLa and HFF-1 cells incubated with 50 μg/mL of targeted NS functionalized with 20 μg FITC and 200 μg folate. White markings are cell outlines used to quantify NS cell selectivity. . . 92

LIST OF TABLES

Table 2.1: Content of Europium(III) in Silica Nanoshells 26

Table 2.2: Size and Zeta Potential of Silica Nanoshells in Aqueous Suspension[a] 28

Table 2.3: Emission Ratio Analysis Results 32

Table 3.1: Yield of Hollow TiO_2 Nanoshells and Their Europium Content. 47

Table 3.2: Average Diameters of Eu^{3+}-Doped Core-shell and Hollow Nanoshells from SEM Images[1]. 48

Table 3.3: Dynamic Light Scattering Measurements of Eu^{3+}-Doped and Undoped Core-shell and Hollow Nanoshells[1]. 50

Table 3.4: Luminescence Intensity Ratio Analysis for 200 nm PEI-Coated TiO_2 NSs Made Using 0.025% $Eu(NO_3)_3 \cdot 5H_2O$[1]. 57

Table 4.1: Dynamic Light Scattering (DLS) Size and Zeta Potentials of 100nm SiO_2 Nanoshells (NS) in Aqueous Suspension[1]. 78

Table 4.2: Nanoshell (NS) Cell Adhesion Fluorescence Quantification Ratio on HeLa Cells. 82

Table 4.3: Differences in Nanoshells (NS) HeLa Cell Adhesion/Endocytosis between Folate NS and PEG NS Counterparts by Fluorescence Microscopy. 85

Table 4.4: Quantification of Nanoshell (NS) Cell Endocytosis by HeLa Cells using Confocal Cross-Sectional Image Analysis. 88

Table 4.5: Differences in Nanoshells (NS) endocytosis by HeLa Cells between Folate NS and PEG NS Counterparts using Confocal Cross-Sectional Images. 89

Table 4.6: Number of Confocal Cell Outlines with a Sample Ratio over 1, 0.8, and 0.6. 90

Table 4.7: Quantification of Nanoshells (NS) Selective Cell Adhesion/adhesion by Fluorescence Microscopy. 94

ACKNOWLEDGEMENTS

First and foremost, I am extremely grateful to my advisor Professor Andrew Kummel for the opportunity to do cutting-edge research and for his continuous feedback and involvement in my work. I would also like to acknowledge my co-advisor Professor Michael Heller for his steady support. I would like to thank Professor William Trogler for his support and feedback which was instrumental to the success of my research. I am also thankful to the rest of my doctoral committee, Professors Liangfang Zhang and Xiaohua Huang, for their thoughtful comments and encouragement.

I am deeply grateful to the collaborators I had the chance to work with: Dr. Robbin Newlin from the Sanford-Burham Medical Research Institute, and Drs. Milan Mikale, Breda Walsh, Kersi Pestonjamasp, and Dennis Heath from UCSD Moore's Cancer Center.

I am thankful to everyone in the NanoTumor Center for making my research enjoyable. For their support of my work, I acknowledge Professor Jian Yang, Dr. María José Cortés-Mateos, Dr. Ana Sanchez, Dr. Davorka Messmer, Professor Jessica Wang-Rodriguez, Professor Sarah Blair, Dr. Jennifer Marciniak, and Professor Ivan Schuller. I am very grateful to graduate students I had the opportunity to work with for their encouragement: Dr. Manuel Ruidiaz, Dr. David Martin, Casey Ta, Dr. Henry Paul Martinez, Dr. Kristina K.P. Mitchell, Dr. Corbin Clawson, Dr. Marta Sartor, Dr. Jack Hu, Gen Yong, Casey Chiang, Carolyn Schutt, Dr. Stuart Ibsen. For dedication and contributions to my research I am thankful to Larissa Low and the undergraduate students: Alex Liberman, Jesus Alfaro, Sharraya Aschemeyer, Diana Lopez, Melissa Aillaud, and Natalie Mendez.

I am extremely grateful for the financial support I received through the National Institute of Health's NanoTumor Center: 5 U54 CA119335-02, the Center of Nanotechnology for Treatment, Understanding, and Monitoring of Cancer, CURE

Research Supplements to Promote Diversity in Health Related Research, and the National Science Foundation's Bridge to the Doctorate Fellowship Program..

Last but not least, I would like to acknowledge the support I have received from my family and friends, especially Abigail Ruiz, thank you for all you're love and support throughout this long journey.

The text and figures of Chapter 2 are a reprint of a published paper, Yang J., Sandoval S., Alfaro J.G., Aschemeyer S., Liberman, A., Martin D.T., Makale M., Kummel A.C., Trogler W.C., Red-luminescent Europium(III) Doped Silica Nanoshells: Synthesis, Characterization and Two-Photon Imaging of Their Interaction with HeLa Cells, *Journal of Biomedical Optics*, 2011, Jun;16(6): 066012. Copyright 2011. The dissertation author was the primary researcher and author of this work.

The contents of Chapter 3 are part of a manuscript in preparation, Sandoval S., Yang J., Alfaro J.G., Aschemeyer S., Liberman, A., Mikale M., Chiang C., Schuller I., Kummel A.C., Trogler W.C. "Europium Doped TiO_2 Hollow Nanoshells: Two-Photon Imaging of Cell Binding." The dissertation author was the primary researcher and author of this work.

The contents of Chapter 4 are part of a manuscript in preparation, Liberman, A., Alfaro J.G., Yang J., Aschemeyer S., Kummel A.C., Trogler W.C. "Targeting of Ovarian Cancer Cells using Folate Functionalized SiO_2 hollow nanoparticles." The dissertation author was dissertation author was the primary researcher and author of this work.

VITA

2003	B.S. in Chemical Engineering, University of California, Irvine
2008	M.S. in Bioengineering, University of California, San Diego
2012	Ph.D. in Bioengineering, University of California, San Diego

PUBLICATIONS

Ruidiaz M.E., Cortes-Mateos M.J., **Sandoval S.**, Martin D.T., Wang-Rodriguez J., Hasteh F., Wallace A., Vose J., Kummel A.C., Blair S.L.; Quantitative Comparison of Surgical Margin Histology Following Excision with Traditional Electrosurgery and a Low-Thermal-Injury Dissection Device., *Journal of Surgical Oncology*., 2011, Jul 8. doi: 10.1002/jso.22012.

Martin D.T., **Sandoval S.**, Carter A., Rodwell M., Smith S., Kummel A. C., Messmer D., Fabrication of Silicon on Borosilicate Glass Microarrays for Quantitative Live Cell Imaging, 2011 *Materials Research Society Symposium Proceedings*. Vol. 1346, aa04-02, DOI: 10.1557/opl.2011.1076.

Yang J., **Sandoval S.**, Alfaro J.G., Aschemeyer S., Liberman, A., Martin D.T., Makale M., Kummel A.C., Trogler W.C., Red-luminescent Europium(III) Doped Silica Nanoshells: Synthesis, Characterization and Two-Photon Imaging of Their Interaction with HeLa Cells, *Journal of Biomedical Optics*, 2011, Jun;16(6) : 066012.

Martin D.T., **Sandoval S.**, Ta C.N., Ruidiaz M. E., Cortes M. J., Messmer D., Kummel A. C., Blair S. L., Wang-Rodriguez J., Quantitative Automated Image Analysis System with Automated Debris Filtering for the Detection of Breast Carcinoma Cells, *Acta Cytologica*, 2011, 55(3) : 271-80., Epub 2011 Apr 27.

Martinez H.P., Kono Y., Blair S.L., **Sandoval S.**, Wang-Rodriguez J., Mattrey R.F., Kummel A.C., Trogler W.C., Hard shell gas-filled contrast enhancement particles for color Doppler ultrasound imaging of tumors, *Med. Chem. Comm.*, 2010, **1**, 266-270.

Cortes-Mateos M.J., Martin D., **Sandoval S**., Ruidiaz M.E., Messmer D., Wang-Rodriguez J., Trogler W., Kummel A.C., Blair S.L., Automated microscopy to evaluate surgical specimens via touch prep in breast cancer., *Annals of Surgical Oncology*, 2009 Mar;16(3):709-20.

Blair S.L., Wang-Rodriguez J., Cortes-Mateos M.J., Messmer D., **Sandoval S.**, Messmer B., Trogler W., and Kummel A., 2007. Enhanced touch preps improve the ease of interpretation of intra-operative breast cancer margins, *American Journal of Surgery*. Oct;73(10):973-6.

ABSTRACT OF THE DISSERATION

Hollow Nanoshells for Cancer Diagnostics and Therapy

by

Sergio Sandoval

Doctor of Philosophy in Bioengineering

University of California, San Diego, 2012

Professor Andrew C. Kummel, Chair

Professor Michael J. Heller, Co-Chair

An important area of biomedical nanotechnology is based on the interaction of living systems with inorganic and organic materials at the nanoscale. Silica nanoshells (NS) are attractive biomaterials because of their advantages as readily functionalized transport and imaging devices. Some of the advantages of silica include: the porous structure of amorphous silica allows small molecule storage; the surface can be modified easily with trimethoxysilyl reagents; silica has low biotoxicity and good biocompatibility. In addition, titanium and titanium alloys have a long history in medical applications due to the excellent biocompatibility of its surface oxides, and more recently, titania (TiO_2) nanomaterials have gained interest in cancer research due to TiO_2 nanoparticles producing photo-induced electrons and holes under ultra-violet (UV) excitation leading to their possible use as photodynamic therapy agents. Consequently, silica and titania nanoshells potentially have multiple biomedical

applications such as imaging agents, targeted drug delivery agents, or gene transferring motherships.

Simple scalable methods to fabricate uniform luminescent europium-doped, hollow silica or titania NS with 200 nm diameters are reported in this thesis. Fluorophore reporter, Eu^{3+} ions, were incorporated directly into the NS matrix, leaving the surface free for targeting functionalization, while also leaving the nanoshell interior free for drug or other payload encapsulation. Amino polystyrene beads were used as templates and a 5-10 nm thick silica or titania gel coating was formed by the sol-gel reaction. After removing template by calcination, porous dehydrated silica gel or predominately anatase titania phase nanoshells of uniform size were obtained. The structure of the nanoshells were characterized by transmission electron microscopy measurements and XRD analysis, while particle size and zetapotentials of the particles suspended in aqueous solution were characterized by dynamic light scattering and their emission and excitation spectra were analyzed using a luminescence spectrometer. Furthermore, the surfaces of SiO_2 NS were functionalized with folic acid in order to specifically target cancer cells.

Folic acid, also known as vitamin B9 or folate, is essential for the synthesis of nucleotide bases and binds with high affinity to folate receptors, which are frequently over-expressed in tumor cells such as certain ovarian and cervical carcinomas, for example. With the use of fluorescent and confocal microscopy, it was found that as the amount of folate on the surface of the NS was increased, a higher amount of NS adhered and endocytosed into HeLa cancer cells, a cervical cancer cell line, when compared to non-targeted NS. In addition, a selectivity experiment demonstrated that folate targeted NS did selectively target the folate receptor rich HeLa cancer cells at a higher rate when they were mixed in with human foreskin fibroblast (HFF-1), a normal cell line. Nanoshell interactions with HeLa cervical cancer cells *in vitro* were also studied and quantified using a luminescence ratio analysis to assess nanoshells adhesion and cell endocytosis.

Chapter 1. Introduction

1.1 Nanoparticles in Biomedical Field

Currently a plethora of nanoparticle based technologies are being developed for biomedical applications. These nanoparticles are typically synthesized using polymeric [1-4], liposomal [5-8], or inorganic formulations [9-12]. The purposes of these technologies are to further improve medical treatments in applications such as therapeutic delivery [1-4], ablative therapy sensitizers [13-15], and biomedical imaging [16-18]. Two highly critical parameters which define nanoparticle efficacy are *in vivo* circulation time and cellular accumulation or adhesion. The longer a particle can survive and circulate *in vivo*, the higher probability it can accumulate at a desired target or provide other capabilities. Additionally, there are many advantages to intracellular delivery of nanoparticles, specifically in therapeutic delivery.

1.2 Silica Nanoparticles

An important area of biomedical nanotechnology is based on the interaction of living systems with inorganic and organic materials at the nanoscale. Silica nanoparticles (NPs) are attractive biomaterials because of their advantages as readily functionalized transport and imaging devices [19-21]: silica has low cellular biotoxicity and good biocompatibility [22]; the surface of silica can be modified readily with trimethoxysilyl reagents [23, 24] which allows for easy surface modification such as the attachment of biomolecules [23, 25] ; and silica can be used to encapsulate small molecules [26]. Silica NPs potentially have multiple biomedical applications as imaging agents, targeted drug delivery agents, or gene transferring motherships [27-30].

Fluorescent silica NPs have been used for imaging in cell culture and animal *in vivo* studies [31, 32]. The organic fluorescent dyes used are either covalently conjugated to the surface of silica [33] or encapsulated in the SiO_2 core [34]. Organic dyes are limited by their broad emission range, photobleaching, short fluorescence lifetimes, and high cost. Furthermore, functionalization of the silica surface with dye

molecules reduces the reactive surface sites available for coupling targeting agents to the NPs. Other groups have synthesized silica NPs with different inorganic luminescent quantum dot (QD) sources [35-37] ; however these NPs do not have a viable future in human *in vivo* studies due to the toxicity of the QD components.

1.3 Titania Nanoparticles

Titania nanomaterials and hybrid derivatives have attracted interest because of their broad range of industrial applications, such as in photovoltaic devices [38, 39], chemical/gas sensors [40], catalysis [41, 42], waste water treatment [43, 44], and in filtration and sorption media [45]. Titania nanomaterials and their compound hybrid composites are also intriguing for medical applications [46-52] and several studies of applications in anti-cancer research [53-56] have appeared. When TiO_2 nanoparticles undergo photoexcition with ultraviolet (UV) light, photo-induced electrons and holes are produced. These electrons and holes can react with hydroxyl ions or water to produce reactive hydroxyl radicals (·OH) and perhydroxyl radicals (HO_2·). These oxygen species not only react with organic wastes in the environment and decompose them into non-toxic molecules, but are also highly reactive with cells and can cause DNA strand breaking through genotoxicity [53, 57]. This characteristic gives titania nanomaterials the potential to be used as photodynamic therapy agents in cancer treatments [58, 59]. Furthermore, the use of various titania and hybrid titania nanocomposites made up of gold [60], silver [61], copper [62], platinum [54, 63], and iron cooperatives [49], as well as titania nanoparticles combined with specific antibodies [64], have potential as cancer therapies such as, photodynamic therapy or magnetic therapy (Fe composites).

Several methods have been described for the synthesis of TiO_2 nanospheres. Caruso and co-workers [65, 66] used a layer-by-layer (LbL) self-assembly technique to fabricate both SiO_2 and TiO_2 hollow spheres. For the TiO_2 spheres, a positively charged TiO_2 colloid was used to form a shell around polymer templates through the absorption of polyelectrolytes. Repeated absorption of polyelectrolytes and TiO_2 precursors increased the thickness and integrity of the shell wall. Xia, *et al* [67]

prepared hollow TiO_2 spheres by using crystalline arrays of polystyrene beads as a template. Well-defined TiO_2 spheres could be fabricated from these methods, but multiple steps are needed, which makes these methods challenging for the large-scale fabrication needed in biomedical applications. Similar templating methods using activated carbon [68] or polymers [69-72] as cores have also been reported. Alternative methods, such as ultrasonic spray pyrolysis [73], diffusion flame synthesis [74], and supercritical fluid methods [75, 76] have been used as potentially scalable routes to create TiO_2 spheres; these processes tend to produce nanoparticles with a wide range of sizes and/or have fragile shell structures.

1.4 Rare Earth Ions as Luminescent Reporters for Nanoparticles

Another active research area has been the development of nanoparticles that incorporate rare-earth ions within their structures. Rare-earth materials have attractive properties that include increased photostability, reduced light scattering, narrow emission spectra, large emissive Stokes shifts, long luminescence lifetimes, and allow for simple functionalization strategies [77, 78]. In addition, rare-earth ions are believed to be non-cytotoxic [79]. Rare-earth ions such as europium (Eu^{3+}), erbium (Er^{3+}), or yttrium (Y^{3+}) doped into insulators often yield efficient inorganic luminescent centers. Europium is particularly advantageous because europium(III) ions produce red photoluminescence with narrow atomic emission profiles when doped in inorganic lattices.

1.5 Silica and Titania as a Europium Ion Host

Silica makes an excellent host for europium ions due to its porous material properties which allows for easy material impregnation [80]. This type of impregnation is typically performed using a silica sol-gel method, which has been used to impregnate materials such as Ag [81], In_2O_3 [82], and CdSe [83] within different silica sol-gel matrices. In addition to these works, a number of studies have been presented on Eu^{3+} sol-gel silica systems, which have demonstrated that after heating of the silica sol-gel,

Eu^{3+} ion lose water and solvent coordination, which consequently results in a more rigid silica cage which entraps Eu^{3+}ions within the remaining amorphous silica structure [84-89].

Being that TiO_2 has a similar structure to SiO_2, and a mentioned earlier, has photoactive properties which can be applied to cancer therapy [58, 59], the idea of titania as a europuim host for cancer applications was explored. Due to its high transparency to visible light and its robust thermal, chemical, and mechanical properties [90-92], titania in particular was found to be an ideal host material for Eu^{3+}. Several Eu^{3+} doped TiO_2 films, nanocrystals, and particles have already been reported [90, 91, 93-102]. The high efficiency of reactive oxygen production during near-UV irradiation of TiO_2 leads to enhanced photobleaching of organic dyes [103] in aerobic environments. Thus, europium provides an inexpensive, long lifetime, low cytotoxicity, and safe method for fluorescence imaging compared to organic fluorophores [77, 104].

1.6 Europium Doped Silica Nanoshells

We previously reported a simple method of synthesis of silica and titania nanoshells (NS) particles with amino polystyrene (APS) beads as templates [10]. In the second chapter of this thesis, a method for preparing Eu^{3+} doped silica NS is reported. The uniqueness of these NS particles lies in the fact that the fluorophore reporter is directly incorporated in the NS matrix, leaving the entire NS surface free for future targeting or biomolecule functionalization while also leaving the NS interior free for drug or biomolecule encapsulation. Hydrolyzed tetramethyl orthosilicate (TMOS) was used as a precursor of silica. APS beads were used as templates in the sol-gel reaction, and $Eu(NO_3)_3$ was added as the dopant. The reaction occurred in ethanol at room temperature, and the APS cores were removed by calcination. The size of NS could be controlled by using APS beads with different diameters. The NS had uniform and robust silica walls of 8-10 nm thickness with Eu^{3+} doping levels below 3% mole fraction. When the Eu^{3+} content exceeded 3%, only irregularly sized colloidal material was obtained. The Eu^{3+} doped silica NS showed a narrow emission at 615 nm under UV excitation. This provides a simple, inexpensive and scalable method to prepare

Eu^{3+} doped silica NS for imaging studies. The long-lived atomic emission of Eu^{3+} makes it an efficient two-photon absorber. This chapter also reports on the interaction of these luminescent silica spheres with HeLa cancer cells as probed by two-photon (2-P) spectroscopy.

1.7 Europium Doped Titania Nanoshells

Chapter three of this thesis describes a simple method of synthesizing uniform, monodispersed, europium-doped, hollow TiO_2 nanoshells (NS) that have rigid shell walls. The utility of this NS design is that the long lived fluorophore reporter, Eu^{3+}, is incorporated directly into the NS matrix, leaving the surface free for functionalization and the NS interior free for payload encapsulation. APS beads were used as templates in the synthesis. Titanium(IV) *t*-butoxide was used as the precursor for titania deposition in order to reduce the rate of hydrolysis and suppress nontemplated growth. The sol-gel hydrolysis of titanium(IV) *t*-butoxide was catalyzed on the surface of amine functionalized PS beads to form a thin, porous titania shell. Doping was effected by using 95% ethanol and dissolved europium(III) nitrate. After removing the PS core by calcination hollow, nanoporous TiO_2 NS with red luminescence, characteristic of doping by Eu^{3+}, were isolated. This protocol provides a simple, inexpensive, and scalable method to prepare Eu^{3+} doped titania NS for imaging studies. Furthermore, a cationic polymer, poly(ethylenimine) (PEI) was coated on the surface of Eu/TiO_2 NS to alter the surface charge from negative to positive, allowing the NS to adhere to HeLa cervical cancer cells. Cell to NS interactions were imaged using 2-P microscopy and quantified using a previously reported luminescence ratio analysis [105].

1.8 Reasoning for Nanoparticle Encapsulation and Targeting

Many cancer therapeutics are hydrophobic and have poor bioavailability and *in vivo* stability. As a result, these drugs are packaged with a variety of surfactants and other products, such as Cremophor EL, which can have adverse side effects [106]. In the case of other therapeutics currently in development, such as siRNA, or various catalytic enzymes and other nucleic acid based therapies, the *in vivo* half-life (minutes

to 2 hours for unmodified siRNA varying by report) is too short to be an effective therapy without some form of delivery vehicle [107]. In both of these cases, encapsulation within a nanoparticle can aid in intracellular delivery. For instance, targeted particles could be utilized to locally raise the drug concentration rather than subjecting the entire body to the adverse effects of chemotherapeutics. This can potentially allow for lower drug dosing while also resulting in a more effective therapeutic.

1.9 Folate as a Cancer Targeting Ligand

A variety of methods have been studied to create targeted nanoparticles. Folate targeting, for instance, has been investigated over the past several years as a method to specifically target and deliver nanoparticles to various types of cancers [108-111]. Folate, or Vitamin B_9, is required by cells for the biosynthesis of nucleotides [112, 113], a process necessary in DNA replication; it is the DNA replication process that becomes uninhibited in many cancers, causing unregulated cell growth and proliferation [114]. Folate is an ideal candidate for use as a cancer targeting ligand primarily due to: (a) the overexpression of folate receptor α (FR) found on a wide variety of human cancers including ovarian, breast, and colorectal cancers [115-125], (b) FRs high binding affinity for folic acid ($K_d \approx 0.1$ nM) [126], and (c) the low risk of folate targeted nanoparticles interacting with normal tissue due to those few FRs that are expressed in normal cells being highly inaccessible due to their location on the apical (i.e. lumen facing) surface of polarized epithelia [127-129]. Thus, the overexpression of the folate receptor suggests that it may be possible to concentrate a toxic dose at the cancerous tissues while sparing the normal tissue from exposure to potent chemotherapeutics [125].

Previous studies have shown that surface functionalization of the nanoparticles with folate does, in fact, increase uptake of nanoparticles by cancer cells [130-134]. For example, Rosenholm *et al*. showed that the addition of folic acid to the surface of mesoporous silica nanoparticles, which were also functionalized with fluorescent reporter FITC, increased the number of HeLa cells which uptake particles from 24% to

52% after 24 hours [130]. Another study by Werner *et al*. showed mice treated with folate targeted PLGA nanoparticles loaded with paclitaxel and a radiosensitizer, survived an additional 30 days at 50% survival, compared to those treated with non-targeted nanoparticles [133].

1.10 Previous Work on Quantification of Cellular Uptake and Surface Adhesion of Nanoparticles

A wide variety of techniques have been previously employed in quantifying cellular uptake and/or surface adhesion of nanoparticles. These techniques primarily involve quantification through fluorescence and mass spectroscopy or atomic spectroscopy [135-142]. Inductively coupled plasma-atomic emission spectroscopy **(**ICP-AES) has been used to calculate the uptake of gold particles into HeLa cells as a function of size, concentration, aspect ratio, and incubation time [136], as well as to quantify the uptake of superparamagnetic, folate/polyethylene glycol (PEG) functionalized magnetite particles in BT20 human breast cancer cells and in RAW 264.7 mouse macrophage cells [137]. The latter study found that functionalizing the surface of the particles with folate and PEG reduced protein adsorption and facilitated the uptake of particles. Although, methods such as fluorescence, mass, and atomic spectroscopy can be used to quantify the amount of nanoparticles present in cells [142], they cannot distinguish between internalized particles and those only adhered to the cell surface. Often times, one way to get around this problem, multiple methods must be used to quantify nanoparticle uptake. For example in the study by Yin *et al.*, the efficiency of targeted PLGA particle uptake in Caco-2 in human colon adenocarcinoma cells were examined by detecting fluorescent markers with a fluorescence micro-plate reader, after performing multiple and rigorous washing steps and lysing the plated cells. The data then had to be confirmed qualitatively with CLSM, Cryo-SEM, and TEM in order to confirm if the nanoparticles were actually internalized within cells [140] and not just adhered to the cell surface.

1.11 Quantification of Folate Targeted Nanoshell Cell Interations by Performing a Novel Fluorescent Ratio Analysis on Captured Microscopy Images

In chapter four of this thesis, a simple method to functionalize hollow silica nanoshells with folate as a cancer targeting ligand and FITC as a fluorescent reporter is described. In addition, a novel fluorescent ratio analysis method is conveyed, which was performed exclusively on fluorescence and confocal microscopy images in order to quantify nanoparticle cell adhesion and intracellular uptake, as well as cancer cell selectivity, of fluorescently labeled, hollow silica nanoshells, while also demonstrating the advantage of folate targeting compared to non-targeted silica nanoshells.

1.12 Acknowledgments

Kristina K. Pohaku Mitchell is acknowledged for her thoughtful comments that greatly improved this chapter.

1.13 References

1. Chan, J.M., et al., *PLGA-lecithin-PEG coreshell nanoparticles for controlled drug delivery.* Biomaterials, 2009. **30**(8): p. 1627-1634.

2. Cheng, J., et al., *Formulation of functionalized PLGA-PEG nanoparticles for in vivo targeted drug delivery.* Biomaterials, 2007. **28**(5): p. 869-876.

3. de Salamanca, A.E., et al., *Chitosan Nanoparticles as a Potential Drug Delivery System for the Ocular Surface: Toxicity, Uptake Mechanism and In Vivo Tolerance.* Investigative Ophthalmology & Visual Science, 2006. **47**(4): p. 1416-1425.

4. Davis, M.E., *The First Targeted Delivery of siRNA in Humans via a Self-Assembling, Cyclodextrin Polymer-Based Nanoparticle: From Concept to Clinic.* Molecular Pharmaceutics, 2009. **6**(3): p. 659-668.

5. Kong, G., et al., *Efficacy of Liposomes and Hyperthermia in a Human Tumor Xenograft Model: Importance of Triggered Drug Release.* Cancer Research, 2000. **60**(24): p. 6950-6957.

6. Ibsen, S., et al., *A novel nested liposome drug delivery vehicle capable of ultrasound triggered release of its payload.* Journal of Controlled Release, 2011. **155**(3): p. 358-366.

7. Bandekar, A., et al., *Antitumor efficacy following the intracellular and interstitial release of liposomal doxorubicin.* Biomaterials, 2012. **33**(17): p. 4345-4352.

8. Muthu, M.S., et al., *Theranostic liposomes of TPGS coating for targeted co-delivery of docetaxel and quantum dots.* Biomaterials, 2012. **33**(12): p. 3494-3501.

9. Kong, S.D., et al., *Magnetically Vectored Nanocapsules for Tumor Penetration and Remotely Switchable On-Demand Drug Release.* Nano Letters, 2010. **10**(12): p. 5088-5092.

10. Yang, J., J.U. Lind, and W.C. Trogler, *Synthesis of Hollow Silica and Titania Nanospheres.* Chemistry of Materials, 2008. **20**(9): p. 2875-2877.

11. Podsiadlo, P., et al., *Gold Nanoparticles Enhance the Anti-Leukemia Action of a 6-Mercaptopurine Chemotherapeutic Agent.* Langmuir, 2007. **24**(2): p. 568-574.

12. Gupta, A.K. and M. Gupta, *Synthesis and surface engineering of iron oxide nanoparticles for biomedical applications.* Biomaterials, 2005. **26**(18): p. 3995-4021.

13. Yoshida, M., et al., *Tumor local chemohyperthermia using docetaxel-embedded magnetoliposomes: Interaction of chemotherapy and hyperthermia.* Journal of Gastroenterology and Hepatology, 2012. **27**(2): p. 406-411.

14. Hocine, O., et al., *Silicalites and Mesoporous Silica Nanoparticles for photodynamic therapy.* International Journal of Pharmaceutics, 2010. **402**(1,2): p. 221-230.

15. Wang, X., et al., *Perfluorohexane-Encapsulated Mesoporous Silica Nanocapsules as Enhancement Agents for Highly Efficient High Intensity Focused Ultrasound (HIFU).* Advanced Materials, 2012. **24**(6): p. 785-791.

16. Liberman, A., et al., *Hollow silica and silica-boron nano/microparticles for contrast-enhanced ultrasound to detect small tumors.* Biomaterials, 2012. **33**(20): p. 5124-5129.

17. Michalet, X., et al., *Quantum Dots for Live Cells, in Vivo Imaging, and Diagnostics.* Science, 2005. **307**(5709): p. 538-544.

18. Sharma, P., et al., *Nanoparticles for bioimaging.* Advances in Colloid and Interface Science, 2006. **123,126**(0): p. 471-485.

19. Barbe, C., et al., *Silica particles: A novel drug-delivery system.* Advanced Materials, 2004. **16**(21): p. 1959-1966.

20. Sharrna, P., et al., *Nanoparticles for bioimaging.* Advances in Colloid and Interface Science, 2006. **123**: p. 471-485.

21. Lai, C.W., Hsiao, J.K., Chen, Y.C., Chou, P.T., *Nanomaterials for the Life Sciences*. Spherical and Anisotropic Silica Shell Nanomaterials. Vol. 3, Chapter 10. 2009: Wiley-VCH.

22. Jin, Y., Lohstreter, S., Zhao, J.X. , *Nanomaterials for the Life Sciences*. Toxicity of Spherical and Anisotropic Nano Silica. Vol. 2, Chapter 1. 2009: Wiley-VCH.

23. Lipski, A.M., et al., *Nanoscale engineering of biomaterial surfaces.* Advanced Materials, 2007. **19**(4): p. 553-+.

24. Smith, J.E., L. Wang, and W.T. Tan, *Bioconjugated silica-coated nanoparticles for bioseparation and bioanalysis.* Trac-Trends in Analytical Chemistry, 2006. **25**(9): p. 848-855.

25. Choi, H. and I.W. Chen, *Surface-modified silica colloid for diagnostic imaging.* Journal of Colloid and Interface Science, 2003. **258**(2): p. 435-437.

26. Jain, T.K., et al., *Nanometer Silica Particles Encapsulating Active Compounds: A Novel Ceramic Drug Carrier.* Journal of the American Chemical Society, 1998. **120**(43): p. 11092-11095.

27. Kim, T.H., K.H. Lee, and Y.K. Kwon, *Monodisperse hollow titania nanospheres prepared using a cationic colloidal template.* Journal of Colloid and Interface Science, 2006. **304**(2): p. 370-377.

28. Bharali, D.J., et al., *Organically modified silica nanoparticles: A nonviral vector for in vivo gene delivery and expression in the brain.* Proceedings of the National Academy of Sciences of the United States of America, 2005. **102**(32): p. 11539-11544.

29. Torney, F., et al., *Mesoporous silica nanoparticles deliver DNA and chemicals into plants.* Nature Nanotechnology, 2007. **2**(5): p. 295-300.

30. Tan, W.H., et al., *Bionanotechnology based on silica nanoparticles.* Medicinal Research Reviews, 2004. **24**(5): p. 621-638.

31. Burns, A., H. Ow, and U. Wiesner, *Fluorescent core-shell silica nanoparticles: towards "Lab on a Particle" architectures for nanobiotechnology.* Chemical Society Reviews, 2006. **35**(11): p. 1028-1042.

32. Knopp, D., D.P. Tang, and R. Niessner, *Bioanalytical applications of biomolecule-functionalized nanometer-sized doped silica particles.* Analytica Chimica Acta, 2009. **647**(1): p. 14-30.

33. Cauda, V., et al., *Multiple Core-Shell Functionalized Colloidal Mesoporous Silica Nanoparticles.* Journal of the American Chemical Society, 2009. **131**(32): p. 11361-11370.

34. Estevez, M.C., et al., *Highly Fluorescent Dye-Doped Silica Nanoparticles Increase Flow Cytometry Sensitivity for Cancer Cell Monitoring.* Nano Research, 2009. **2**(6): p. 448-461.

35. Xu, Y., et al., *Multifunctional Fe3O4 Cored Magnetic-Quantum Dot Fluorescent Nanocomposites for RF Nanohyperthermia of Cancer Cells.* Journal of Physical Chemistry C, 2010. **114**(11): p. 5020-5026.

36. Lim, Y.T., et al., *Multifunctional Silica Nanocapsule with a Single Surface Hole.* Small, 2009. **5**(3): p. 324-328.

37. Chen, L.Y., et al., *CdTe quantum dot functionalized silica nanosphere labels for ultrasensitive detection of biomarker.* Chemical Communications, 2009(19): p. 2670-2672.

38. Ma, L., et al., *Fabrication and properties of meso-macroporous electrodes screen-printed from mesoporous titania nanoparticles for dye-sensitized solar cells.* Mater Chem Phys, 2009. **118**(2-3): p. 477-483.

39. Vlachopoulos, N., et al., *Very efficient visible light energy harvesting and conversion by spectral sensitization of high surface area polycrystalline titanium dioxide films.* J Amer Chem Soc, 1988. **110**(4): p. 1216-1220.

40. Mohammadi, M.R., D.J. Fray, and M.C. Cordero-Cabrera, *Sensor performance of nanostructured TiO2 thin films derived from particulate sol-gel route and polymeric fugitive agents.* Sens Actuators B, 2007. **124**(1): p. 74-83.

41. Xu, J., et al., *Synthesis of Gd-doped TiO2 nanoparticles under mild condition and their photocatalytic activity.* Colloids Surf A, 2009. **334**(1-3): p. 107-111.

42. Li, Y., T. Kunitake, and S. Fujikawa, *Efficient Fabrication and Enhanced Photocatalytic Activities of 3D-Ordered Films of Titania Hollow Spheres.* The Journal of Physical Chemistry B, 2006. **110**(26): p. 13000-13004.

43. Lee, S.-A., et al., *Use of Ultrafiltration Membranes for the Separation of TiO2 Photocatalysts in Drinking Water Treatment.* Indus Eng Chem Res, 2001. **40**(7): p. 1712-1719.

44. Park, Y., et al., *Organic dye-sensitized TiO_2 for the redox conversion of water pollutants under visible light.* Chemical Communications, 2010. **46**(14): p. 2477-2479.

45. Arabatzis, I.M. and P. Falaras, *Synthesis of Porous Nanocrystalline TiO_2 Foam.* Nano Letters, 2002. **3**(2): p. 249-251.

46. Macak, J.M., et al., *TiO2 nanotubes: Self-organized electrochemical formation, properties and applications.* Curr Opin Solid State and Mater Sci, 2007. **11**(1-2): p. 3-18.

47. Cao, J., O. Rusina, and H. Sieber, *Processing of porous TiO2-ceramics from biological preforms.* Ceram Int, 2004. **30**(7): p. 1971-1974.

48. Necula, B.S., et al., *In vitro antibacterial activity of porous TiO_2-Ag composite layers against methicillin-resistant Staphylococcus aureus.* Acta Biomaterialia, 2009. **5**(9): p. 3573-3580.

49. Tsuang, Y.-H., et al., *Studies of Photokilling of Bacteria Using Titanium Dioxide Nanoparticles.* Artificial Organs, 2008. **32**(2): p. 167-174.

50. Paunesku, T., et al., *Biology of TiO_2-oligonucleotide nanocomposites.* Nat Mater, 2003. **2**(5): p. 343-346.

51. Wu, H.-P., T.-L. Cheng, and W.-L. Tseng, *Phosphate-Modified TiO_2 Nanoparticles for Selective Detection of Dopamine, Levodopa, Adrenaline, and Catechol Based on Fluorescence Quenching.* Langmuir, 2007. **23**(14): p. 7880-7885.

52. Roy, S.C., M. Paulose, and C.A. Grimes, *The effect of TiO_2 nanotubes in the enhancement of blood clotting for the control of hemorrhage.* Biomaterials, 2007. **28**(31): p. 4667-4672.

53. Zhu, R.R., et al., *Bio-effects of Nano-TiO2 on DNA and cellular ultrastructure with different polymorph and size.* Mater Sci Eng C, 2009. **29**(3): p. 691-696.

54. Lopez, T., et al., *Catalytic nanomedicine: A new field in antitumor treatment using supported platinum nanoparticles. In vitro DNA degradation and in vivo tests with C6 animal model on Wistar rats.* Eur J Med Chem, 2010. **45**(5): p. 1982-1990.

55. Kubota, Y., et al., *Photokilling of T-24 Human Bladder-Cancer Cells with Titanium-Dioxide.* British Journal of Cancer, 1994. **70**(6): p. 1107-1111.

56. Kalbacova, M., et al., *TiO(2) nanotubes: photocatalyst for cancer cell killing.* Phys Stat Solidi - Rapid Res Lett, 2008. **2**(4): p. 194-196.

57. Trouiller, B., et al., *Titanium Dioxide Nanoparticles Induce DNA Damage and Genetic Instability In vivo in Mice.* Cancer Research, 2009. **69**(22): p. 8784-8789.

58. Chen, W. and J. Zhang, *Using Nanoparticles to Enable Simultaneous Radiation and Photodynamic Therapies for Cancer Treatment.* J Nanosci Nanaotechnol, 2006. **6**: p. 1159-1166.

59. Rozhkova, E.A., et al., *A High-Performance Nanobio Photocatalyst for Targeted Brain Cancer Therapy.* Nano Letters, 2009. **9**(9): p. 3337-3342.

60. Abdulla-Al-Mamun, M., et al., *Enhanced Photocatalytic Cytotoxic Activity of Au@TiO2 Nanopellets against Human Epithelial Carcinoma (HeLa) Cells.* Chem Lett, 2009. **38**(10): p. 950-951.

61. Abdulla-Al-Mamun, M., Y. Kusumoto, and M.S. Islam, *Cytotoxic Evaluation of Ag@TiO2 Core-Shell Composite Nanoclusters against Cancer Cells.* Chem Lett, 2009. **38**(10): p. 980-981.

62. Abdulla-Al-Mamun, M. and Y. Kusumoto, *New Simple Synthesis of Cu-TiO2 Nanocomposite: Highly Enhanced Photocatalytic Killing of Epithelia Carcinoma (HeLa) Cells.* Chem Lett, 2009. **38**(8): p. 826-827.

63. Lopez, T., et al., *Pt/TiO_2 brain biocompatible nanoparticles: GBM treatment using the C6 model in Wistar rats.* Acta Biomaterialia, 2008. **4**(6): p. 2037-2044.

64. Xu, J., et al., *Photokilling cancer cells using highly cell-specific antibody-TiO_2 bioconjugates and electroporation.* Bioelectrochemistry, 2007. **71**(2): p. 217-222.

65. Caruso, R.A., A. Susha, and F. Caruso, *Multilayered Titania, Silica, and Laponite Nanoparticle Coatings on Polystyrene Colloidal Templates and Resulting Inorganic Hollow Spheres.* Chem Mater, 2001. **13**(2): p. 400-409.

66. Meyer, U., et al., *Templating of Porous Polymeric Beads to Form Porous Silica and Titania Spheres.* Adv Mater, 2002. **14**(23): p. 1768-1772.

67. Zhong, Z., et al., *Preparation of Mesoscale Hollow Spheres of TiO2 and SnO2 by Templating Against Crystalline Arrays of Polystyrene Beads.* Adv Mater, 2000. **12**(3): p. 206-209.

68. Lei, Z., et al., *Two-step Templating Route to Macroporous or Hollow Sphere Oxides.* J Mater Chem, 2001. **11**: p. 2930-2933.

69. Kim, T.H., K.H. Lee, and Y.K. Kwon, *Monodisperse hollow titania nanospheres prepared using a cationic colloidal template.* J Colloid Interfac Sci, 2006. **304**(2): p. 370-377.

70. Sun, X., J. Liu, and Y. Li, *Use of Carbonaceous Polysaccharide Microspheres as Templates for Fabricating Metal Oxide Hollow Spheres.* Chemistry - A European Journal, 2006. **12**(7): p. 2039-2047.

71. Wang, D., et al., *Preparation and characterization of TiO_2 hollow spheres.* Materials Letters, 2006. **60**(1): p. 77-80.

72. Yang, Z., et al., *Templated Synthesis of Inorganic Hollow Spheres with a Tunable Cavity Size onto Coreâ€"Shell Gel Particles.* Angew Chem Int Ed, 2003. **42**(17): p. 1943-1945.

73. Blešić, M.D., et al., *TiO2 films prepared by ultrasonic spray pyrolysis of nanosize precursor.* Mater Lett, 2002. **54**(4): p. 298-302.

74. Karan, N.S., et al., *Diffusion flame synthesis of hollow, anatase TiO2 nanoparticles.* Mater Sci Eng B, 2009. **163**(2): p. 128-133.

75. Zhang, C., et al., *Preparation of silica and titanium-containing silica hollow spheres at supercritical CO2/H2O interface.* J Supercrit Fluid, 2007. **42**(1): p. 142-149.

76. Wu, C.-I., et al., *Preparation of TiO2 nanoparticles by supercritical carbon dioxide.* Mater Lett, 2008. **62**(12–13): p. 1923-1926.

77. Bouzigues, C., T. Gacoin, and A. Alexandrou, *Biological Applications of Rare-Earth Based Nanoparticles.* ACS Nano, 2011. **5**(11): p. 8488-8505.

78. Lo, W.S., et al., *Impressive Europium Red Emission Induced by Two-Photon Excitation for Biological Applications.* Inorganic Chemistry, 2011. **50**(12): p. 5309-5311.

79. Andelman, T., et al., *Synthesis and Cytotoxicity of Y2O3 Nanoparticles of Various Morphologies.* Nanoscale Research Letters, 2010. **5**(2): p. 263-273.

80. Taghavinia, N., et al., *Europium-doped yttrium silicate nanoparticles embedded in a porous SiO2 matrix.* Nanotechnology, 2004. **15**(11): p. 1549-1553.

81. Cai, W.P. and L.D. Zhang, *Synthesis and structural and optical properties of mesoporous silica containing silver nanoparticles.* Journal of Physics-Condensed Matter, 1997. **9**(34): p. 7257-7267.

82. Zhou, H., W. Cai, and L. Zhang, *Synthesis and structure of indium oxide nanoparticles dispersed within pores of mesoporous silica.* Materials Research Bulletin, 1999. **34**(6): p. 845-849.

83. Coffer, J.L., G. Beauchamp, and T. Waldek Zerda, *Porous silica glasses doped with quantum-confined cadmium selenide.* Journal of Non-Crystalline Solids, 1992. **142**(0): p. 208-214.

84. Lochhead, M.J. and K.L. Bray, *Spectroscopic characterization of doped sol-gel silica gels and glasses: evidence of inner-sphere complexation of europium(III).* Journal of Non-Crystalline Solids, 1994. **170**(2): p. 143-154.

85. McDonagh, C., et al., *Characterisation of sol-gel glasses using optical probes.* Journal of Non-Crystalline Solids, 1992. **147–148**(0): p. 97-101.

86. Devlin, K., et al., *A structural study of the sol-gel process by optical fluorescence and decay time spectroscopy.* Journal of Non-Crystalline Solids, 1991. **135**(1): p. 8-14.

87. Ferrari, M., et al., *Spectroscopy of trivalent europium in gel-derived silica glasses.* Philosophical Magazine Part B, 1992. **65**(2): p. 251-260.

88. Campostrini, R., et al., *Luminescence of Eu^{3+} ions during thermal densification of SiO_2 gel.* Journal of Materials Research, 1992 **7**(3): p. 745-753.

89. Levy, D., R. Reisfeld, and D. Avnir, *Fluorescence of europium(III) trapped in silica gel-glass as a probe for cation binding and for changes in cage symmetry during gel dehydration.* Chemical Physics Letters, 1984. **109**(6): p. 593-597.

90. Conde-Gallardo, A., et al., *Photoluminescence properties of the Eu[3+] activator ion in the TiO2 host matrix.* Appl Phys Lett, 2001. **78**(22): p. 3436-3436.

91. Li, J.-G., et al., *Phase Structure and Luminescence Properties of Eu3+-Doped TiO2 Nanocrystals Synthesized by Ar/O2 Radio Frequency Thermal Plasma Oxidation of Liquid Precursor Mists.* J Phys Chem B, 2006. **110**(3): p. 1121-1127.

92. Yin, J.B., L.Q. Xiang, and X.P. Zhao, *Monodisperse spherical mesoporous Eu-doped TiO2 phosphor particles and the luminescence properties.* Appl Phys Lett, 2007. **90**(11): p. -.

93. Ghosh, P. and A. Patra, *Influence of Surface Coating on Physical Properties of TiO2/Eu3+ Nanocrystals.* J Phys Chem C, 2007. **111**(19): p. 7004-7010.

94. Julian, B., et al., *One-pot synthesis and optical properties of $Eu^{[3+]}$ -doped nanocrystalline TiO_2 and ZrO_2.* Nanotechnology, 2005. **16**(11): p. 2707-2713.

95. Luo, M., et al., *Enhanced Luminescence of Eu-Doped TiO2 Nanodots.* Nanoscale Res Lett, 2009. **4**(8): p. 809-813.

96. Aihua, P., et al., *Photoluminescence properties of TiO2: Eu3 + thin films deposited on different substrates.* Mater Lett, 2005. **59**(29-30): p. 3866-3869.

97. Tan, M., et al., *Synthesis and characterization of titania-based monodisperse fluorescent europium nanoparticles for biolabeling.* J Lumin, 2006. **117**(1): p. 20-28.

98. Xie, Y. and C. Yuan, *Transparent TiO2 sol nanocrystallites mediated homogeneous-like photocatalytic reaction and hydrosol recycling process.* J Mater Sci, 2005. **40**(24): p. 6375-6383.

99. Xu, Z., et al., *Structure, luminescence properties and photocatalytic activity of europium doped-TiO2 nanoparticles.* J Mater Sci, 2005. **40**(6): p. 1539-1541.

100. Yi, S.-s., et al., *Highly enhanced luminescence of nanocrystalline TiO2:Eu3+ phosphors.* Opt Mater, 2006. **28**(6-7): p. 610-614.

101. Zeng, Q.G., Z.J. Ding, and Z.M. Zhang, *Synthesis, structure and optical properties of Eu3+/TiO2 nanocrystals at room temperature.* J Lumin, 2006. **118**(2): p. 301-307.

102. Zhao, Z., et al., *Optical properties of Eu3+-doped TiO2 nanocrystalline under high pressure.* J Lumin, 2006. **122-123**: p. 862-865.

103. Epling, G.A. and C. Lin, *Photoassisted bleaching of dyes utilizing TiO_2 and visible light.* Chemosphere, 2002. **46**(4): p. 561-570.

104. Andelman, T., et al., *Synthesis and Cytotoxicity of Y2O3 Nanoparticles of Various Morphologies.* Nano Res Lett, 2010. **5**(2): p. 263-273.

105. Yang, J., et al., *Red-luminescent europium (III) doped silica nanoshells: synthesis, characterization, and their interaction with HeLa cells.* Journal of Biomedical Optics, 2011. **16**(6).

106. Gelderblom, H., et al., *Cremophor EL: the drawbacks and advantages of vehicle selection for drug formulation.* European Journal of Cancer, 2001. **37**(13): p. 1590-1598.

107. Behlke, M.A., *Progress towards in Vivo Use of siRNAs.* Mol Ther, 2006. **13**(4): p. 644-670.

108. Zhang, Y., N. Kohler, and M.Q. Zhang, *Surface modification of superparamagnetic magnetite nanoparticles and their intracellular uptake.* Biomaterials, 2002. **23**(7): p. 1553-1561.

109. Oyewumi, M.O. and R.J. Mumper, *Influence of formulation parameters on gadolinium entrapment and tumor cell uptake using folate-coated nanoparticles.* International Journal of Pharmaceutics, 2003. **251**(1-2): p. 85-97.

110. Kukowska-Latallo, J.F., et al., *Nanoparticle Targeting of Anticancer Drug Improves Therapeutic Response in Animal Model of Human Epithelial Cancer.* Cancer Research, 2005. **65**(12): p. 5317-5324.

111. Kularatne, S.A. and P.S. Low, *Targeting of Nanoparticles: Folate Receptor*. Cancer Nanotechnology: Methods in Molecular BiologyVol. Volume 624. 2010: Springer.

112. James, S.J., et al., *The Essentiality of Folate for the Maintenance of Deoxynucleotide Precursor Pools, DNA-Synthesis, and Cell-Cycle Progression in Pha-Stimulated Lymphocytes.* Environmental Health Perspectives, 1993. **101**: p. 173-178.

113. Ulrich, C.M., *Folate and cancer prevention: a closer look at a complex picture.* American Journal of Clinical Nutrition, 2007. **86**(2): p. 271-273.

114. Hilgenbrink, A.R. and P.S. Low, *Folate receptor-mediated drug targeting: From therapeutics to diagnostics.* Journal of Pharmaceutical Sciences, 2005. **94**(10): p. 2135-2146.

115. Campbell, I.G., et al., *Folate-Binding Protein Is a Marker for Ovarian-Cancer.* Cancer Research, 1991. **51**(19): p. 5329-5338.

116. Weitman, S.D., et al., *Distribution of the Folate Receptor Gp38 in Normal and Malignant-Cell Lines and Tissues.* Cancer Research, 1992. **52**(12): p. 3396-3401.

117. Weitman, S.D., K.M. Frazier, and B.A. Kamen, *The Folate Receptor in Central-Nervous-System Malignancies of Childhood.* Journal of Neuro-Oncology, 1994. **21**(2): p. 107-112.

118. Toffoli, G., et al., *Overexpression of folate binding protein in ovarian cancers.* International Journal of Cancer, 1997. **74**(2): p. 193-198.

119. Holm, J., et al., *Characterization of a high-affinity folate receptor in normal and malignant human testicular tissue.* Bioscience Reports, 1999. **19**(6): p. 571-580.

120. Ross, J.F., et al., *Folate receptor type beta is a neutrophilic lineage marker and is differentially expressed in myeloid leukemia.* Cancer, 1999. **85**(2): p. 348-357.

121. Bueno, R., et al., *The alpha folate receptor is highly activated in malignant pleural mesothelioma.* Journal of Thoracic and Cardiovascular Surgery, 2001. **121**(2): p. 225-233.

122. Shia, J., et al., *Immunohistochemical expression of folate receptor α in colorectal carcinoma: patterns and biological significance.* Human Pathology, 2008. **39**(4): p. 498-505.

123. Sudimack, J. and R.J. Lee, *Targeted drug delivery via the folate receptor.* Advanced Drug Delivery Reviews, 2000. **41**(2): p. 147-162.

124. Garinchesa, P., et al., *Trophoblast and Ovarian-Cancer Antigen-Lk26 - Sensitivity and Specificity in Immunopathology and Molecular-Identification as a Folate-Binding Protein.* American Journal of Pathology, 1993. **142**(2): p. 557-567.

125. Ross, J.F., P.K. Chaudhuri, and M. Ratnam, *Differential regulation of folate receptor isoforms in normal and malignant tissues in vivo and in established cell lines. Physiologic and clinical implications.* Cancer, 1994. **73**(9): p. 2432-2443.

126. Wang, X., et al., *Differential Stereospecificities and Affinities of Folate Receptor Isoforms for Folate Compounds and Antifolates.* Biochemical Pharmacology, 1992. **44**(9): p. 1898-1901.

127. Lu, Y.J., et al., *Folate receptor-targeted immunotherapy of cancer: mechanism and therapeutic potential.* Advanced Drug Delivery Reviews, 2004. **56**(8): p. 1161-1176.

128. Lu, Y.J. and P.S. Low, *Folate-mediated delivery of macromolecular anticancer therapeutic agents.* Advanced Drug Delivery Reviews, 2002. **54**(5): p. 675-693.

129. Brannon-Peppas, L. and J.O. Blanchette, *Nanoparticle and targeted systems for cancer therapy.* Advanced Drug Delivery Reviews, 2004. **56**(11): p. 1649-1659.

130. Rosenholm, J.M., et al., *Targeting of Porous Hybrid Silica Nanoparticles to Cancer Cells.* ACS Nano, 2008. **3**(1): p. 197-206.

131. Wu, J., Q. Liu, and R.J. Lee, *A folate receptor-targeted liposomal formulation for paclitaxel.* International Journal of Pharmaceutics, 2006. **316**(1–2): p. 148-153.

132. Zhang, L., et al., *Uptake of folate-conjugated albumin nanoparticles to the SKOV3 cells.* International Journal of Pharmaceutics, 2004. **287**(1–2): p. 155-162.

133. Werner, M.E., et al., *Folate-targeted nanoparticle delivery of chemo- and radiotherapeutics for the treatment of ovarian cancer peritoneal metastasis.* Biomaterials, 2011. **32**(33): p. 8548-8554.

134. Li, L., et al., *Biofunctional self-assembled nanoparticles of folate-PEG-heparin/PBLA copolymers for targeted delivery of doxorubicin.* Journal of Materials Chemistry, 2011. **21**(39): p. 15288-15297.

135. Zauner, W., N.A. Farrow, and A.M.R. Haines, *In vitro uptake of polystyrene microspheres: effect of particle size, cell line and cell density.* Journal of Controlled Release, 2001. **71**(1): p. 39-51.

136. Chithrani, B.D., A.A. Ghazani, and W.C.W. Chan, *Determining the Size and Shape Dependence of Gold Nanoparticle Uptake into Mammalian Cells.* Nano Letters, 2006. **6**(4): p. 662-668.

137. Zhang, Y., N. Kohler, and M. Zhang, *Surface modification of superparamagnetic magnetite nanoparticles and their intracellular uptake.* Biomaterials, 2002. **23**(7): p. 1553-1561.

138. Thurn, K.T., et al., *Endocytosis of titanium dioxide nanoparticles in prostate cancer PC-3M cells.* Nanomedicine : nanotechnology, biology, and medicine, 2011. **7**(2): p. 123-130.

139. Hu, F.X., K.G. Neoh, and E.T. Kang, *Synthesis and in vitro anti-cancer evaluation of tamoxifen-loaded magnetite/PLLA composite nanoparticles.* Biomaterials, 2006. **27**(33): p. 5725-5733.

140. Yin Win, K. and S.-S. Feng, *Effects of particle size and surface coating on cellular uptake of polymeric nanoparticles for oral delivery of anticancer drugs.* Biomaterials, 2005. **26**(15): p. 2713-2722.

141. Davda, J. and V. Labhasetwar, *Characterization of nanoparticle uptake by endothelial cells.* International Journal of Pharmaceutics, 2002. **233**(1,Äì2): p. 51-59.

142. Miller, C.R., et al., *Liposome-Cell Interactions in Vitro: Effect of Liposome Surface Charge on the Binding and Endocytosis of Conventional and Sterically Stabilized Liposomes.* Biochemistry, 1998. **37**(37): p. 12875-12883.

Chapter 2. Red-luminescent Europium (III) Doped Silica Nanoshells: Synthesis, Characterization and Their Interaction with HeLa Cells

A simple method to fabricate Eu^{3+} doped silica nanoshells particles with 100 nm and 200 nm diameters is reported. Amino polystyrene beads were used as templates, and a 8-10 nm thick silica gel coating was formed by the sol-gel reaction. After removing the template by calcination, porous dehydrated silica gel nanoshells of uniform size were obtained. The Eu^{3+} doped silica nanoshells exhibited a red emission at 615 nm on UV excitation. The porous structure of the silica shell wall was characterized by transmission electron microscopy measurements, while particle size and zeta potentials of the particles suspended in aqueous solution were characterized by dynamic light scattering. Two-photon microscopy was used to image the nanoshells after assimilation by HeLa cancer cells.

2.1 Introduction

An important area of biomedical nanotechnology is based on the interaction of living systems with inorganic and organic materials at the nanoscale. Silica nanoparticles (NPs) are attractive biomaterials because of their advantages as readily functionalized transport and imaging devices [1-3]: silica has low cellular biotoxicity and good biocompatibility [4]; the surface of silica can be modified readily with trimethoxysilyl reagents [5, 6] which allows for easy surface modification such as for attaching biomolecules [5, 7]; and silica can be used to encapsulate small molecules [8]. Silica NPs potentially have multiple biomedical applications as imaging agents, targeted drug delivery agents, or gene transferring motherships [9-12].

Fluorescent silica NPs have been used for imaging in cell culture and animal *in vivo* studies [13, 14]. The organic fluorescent dyes used are either covalently conjugated to the surface of silica [15] or encapsulated in the SiO_2 core [16]. Organic dyes are limited by their broad emission range, photobleaching, short fluorescence lifetimes, and high cost. Furthermore, functionalization of the silica surface with dye molecules reduces the reactive surface sites available for coupling targeting agents to the NPs. Other groups have synthesized silica NPs with different inorganic luminescent quantum dot (QD) sources [17-19] ; however these NPs do not have a viable future in human *in vivo* studies due to the toxicity of the QD components. Rare-earth ions such as Eu^{3+}, Er^{3+} or Y^{3+} doped into insulators often yield efficient inorganic luminescent centers. Rare-earth ions have narrow emission spectral peaks and long emission lifetimes, and they are believed to be non-cytotoxic [20]. We previously reported a simple method of synthesis of silica and titania nanoshells (NS) particles with amino polystyrene (APS) beads as templates [21]. In this manuscript, a method for preparing Eu^{3+} doped silica NS is reported. The uniqueness of these NS particles lies in the fact that the fluorophore reporter is directly incorporated in the NS matrix, leaving the entire NS surface free for future targeting or biomolecule fictionalization while also leaving the NS core free for drug or biomolecule encapsulation. Hydrolyzed tetramethyl orthosilicate (TMOS) was used as a precursor of silica. APS beads were used as templates in the sol-gel reaction, and $Eu(NO_3)_3$ was added as the dopant. The reaction employed ethanol solvent at room temperature, and the APS cores were removed by calcination. The size of NS could be controlled by using APS beads with different diameters. The NS had uniform and robust silica walls of 8-10 nm thickness with Eu(III) doping levels below 3% mole fraction. When the Eu^{3+} content exceeded 3%, only irregularly sized colloidal material was obtained. The Eu^{3+} doped silica NS showed a narrow emission at 615 nm under UV excitation. This provides a simple, inexpensive and scalable method to prepare Eu^{3+} doped silica NS for imaging studies. The long-lived atomic emission of Eu(III) makes it an efficient two-photon absorber. This manuscript also reports on the interaction of these luminescent silica spheres with HeLa cancer cells as probed by two-photon spectroscopy.

2.2 Experimental Methods and Materials

2.2.1 Materials

Tetramethyl orthosilicate and europium nitrate hydrate were obtained from Aldrich-Sigma Ltd. All chemicals were used as received. The 100 nm amine functionalized polystyrene beads (2.5% w/w) were purchased from PolySciences Ltd. Nunc Lab-Tek II 4-well chamber slides were obtained from Fisher Scientific (Pittsburgh, PA). HeLa cervical cancer cells were purchased from ATCC (Manassas, VA); Dulbecco's Phosphate Buffer Saline solution (DPBS 1x), Dulbecco's Modified Eagle's Medium (DMEM), and fetal bovine serum (FBS) were purchased from Mediatech, Inc. (Manassas, VA), while media supplements, Chloromethylfluorescein Diacetate (CMFDA) CellTracker Green intracellular stain and Prolong Gold were obtained from Invitrogen (Carlsbad, CA). Paraformaldehyde (PFA) was purchased from ThermoFisher Scientific (Fair Lawn, NJ).

2.2.2 Preparation of Europium Doped Silica Nanoshells (NS)

In a 2 mL Eppendorf tube, 100 uL of a 2.5% weight dispersion (in water) of 100 nm APS beads were suspended in 1.75 mL of absolute ethanol. To this suspension, 6.5 uL of TMOS and then 250 uL of 1 mg/mL $Eu(NO_3)_3 \cdot 5H_2O$/ethanol was added. The mixture was stirred on a vortex mixer at room temperature at a speed of 900 rpm. After 12 h stirring, a white precipitate was collected by centrifugation and washed with ethanol and dried in vacuum for 48 h at room temperature to give 4.1 mg of core-shell spheres. The APS core was removed by calcining the 4.1 mg of core-shell nanospheres by heating in air at 5ºC per minute to 500ºC and maintaining this temperature for 24 h. About 1.5 mg of europium doped SiO_2 nanoshells were collected as a white powder. EDS showed the Eu content of this preparation was 1.35% (mole%).

To increase the absorption efficiency of Eu/SiO_2 nanoshells by HeLa cells, poly(ethylenimine) (PEI) was coated on the spheres, thereby increasing the positive charge of the surface which was hypothesized to improve adherence to the negatively charged HeLa cells. The following coating procedure was employed: 3 mg of Eu-SiO_2

nanoshells were suspended in 1.5 mL of 0.1mg/mL PEI water solution. The suspension was stirred 2 hours and the NS were collected by centrifugation and washed with water. Afterwards, the PEI coated NS were suspended in 0.5 mL of pH 7.4 phosphate buffer for the cell experiments.

2.2.3 Characterization of Silica Nanoshells (NS)

The SEM and EDS measurements were conducted on a FEI/Philips XL30 FEG ESEM microscope with an accelerating voltage of 10 kV. The average diameter of the nanospheres was determined from SEM images. TEM images were obtained with the use of a JEOL-2000EX (200kV) CryoElectro Microscope with an accelerating voltage of 200 kV. A Perkin-Elmer LS 45 luminescence spectrometer was used to record emission and excitation spectra. A Zetasizer Nano ZS from Melvern Instruments was used to determine the DLS size distributions and zeta potentials of nanoshells when resuspended in distilled water with gentle sonication.

2.2.4 Cell Culture

HeLa cervical cancer cells were grown at 5 x 10^4 cells/well on Nunc Lab-Tek II 4-well chamber slides in Dulbecco's Modified Eagle's Medium (DMEM) supplemented with 10% FBS, 1% antibiotics (Penicillin, Streptomycin, Glutamine (PSG)), and 1% sodium pyruvate, at 37 °C in a humidified atmosphere of 5% CO_2. Before starting cell adhesion/endocytosing experiments, the cells were grown to 60 to 80% well confluency.

2.2.5 Cell Adhesion/Endocytosis Experiments

In order to determine the extent of NS cell adhesion/endocytosis, HeLa cells were incubated with 500 mg/mL of europium SiO_2 NS functionalized with amines for 24 hrs in DMEM complete media at 37 °C in a humidified atmosphere of 5% CO_2. Afterwards, cells were washed twice with DPBS and labeled with 2.5 µM CMFDA CellTracker Green intracellular stain in DPBS for 30 min. Subsequently, cells were washed 3x with DPBS to remove any excess dye, fixed with 4% PFA in DPBS solution,

washed twice more with DPBS, and covered with Prolong Gold antifade reagent in order to prepare samples for visualization by two-photon microscopy.

2.2.6 Two-Photon (2-P) Microscopy of Silica Nanoshells Engaging HeLa Cells in vitro

Two-photon (2-P) fluorescence dual color (red/green Europium SiO_2 NS/CMFDA) images were obtained with a custom modified Nikon FN1 intravital microscope fitted with a 60x water immersion objective (Nikon, 1.2 NA). The instrument was driven by a Spectraphysics MaiTai Ti:Sa 3 Watt, 120 femtosecond pulsed laser tuned to 695 nm. The microscope operated in non-descanned mode. Emitted sample light was separated into red/green channels using a beam splitter and band pass filters (Chroma ET620/60 and ET510/50). Two side-on PMTS (Hamamatsu) captured the light, and the raster scan data was assembled and saved using Nikon EZ-1 display/analysis software. Images were initially acquired full field at 60x, with constant gain settings between samples, and regions of interest (ROIs) were magnified 4x by spatially compressing the raster scan. In order to confirm the location of the nanospheres, image volumes composed of multiple 1 μm XY slices were acquired serially along the sample z-axis. 2-P images were further processed for background level and SNR, using ImageJ (NIH, Bethesda, MD) and custom C#-based software written in-house.

2.3 Results and Discussion

2.3.1 Synthesis of Eu-SiO_2 Nanoshells

The synthesis of APS/Eu-SiO_2 core-shell spheres used absolute ethanol as solvent to slow the sol-gel process. Previously, the fabrication of SiO_2 shells on APS beads with the assistant of poly-L-lysine in pH7.4 PBS buffer was reported [21]. The hydrolyzed intermediate of TMOS, silicic acid, was used as the precursor of the SiO_2 layer. To dope Eu^{3+} into the SiO_2 matrix, the procedure was modified to decrease the rate of formation of the silica shell. TMOS instead of silicic acid was used as precursor

of SiO_2, and absolute ethanol instead of PBS was employed as solvent for the hydrolysis of TMOS and the cross-linking of SiO^{4-}. The slowing of the kinetics was crucial in incorporating Eu^{3+} in the NS wall and creating uniform Eu-SiO_2 NS as the presence of $Eu(NO_3)_3$ tended to encourage the formation of colloidal SiO_2 when PBS buffer was used during the sol-gel reaction. The small amount of water for the hydrolysis reaction in this mixture (5% by volume) arises from the added aqueous APS suspension. Formation of the Eu-SiO_2 shell required 12 h of reaction time compared with only 5 min for the formation of the SiO_2 layer in aqueous PBS buffer. The partially protonated amine groups on the surface of APS beads help attract the negative silicic acid precursor to the surface of beads and concurrently Eu^{3+} was trapped into the silica matrix perhaps aided by the ligating amino groups.

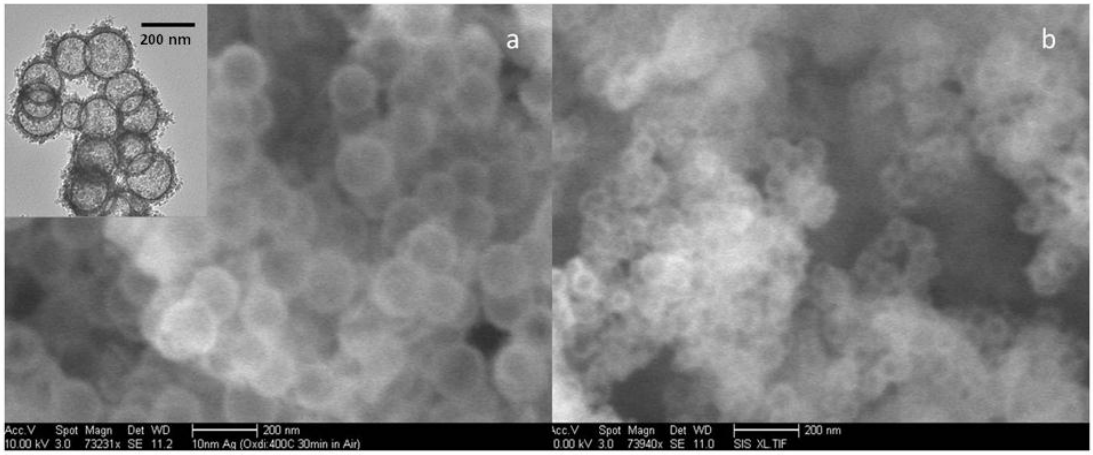

Figure 2.1: SEM and TME images of europium doped silica nanoshells from 200 nm (a) and 100 nm (b) APS templates with europium of 0.54% mole and 1.35% mole, respectively. Scale bars in SEM and TEM images are 200 nm.

Both 100 nm and 200 nm APS beads were used as templates, and variable amounts of Eu^{3+} were doped into the silica NS. Table 2.1 shows the concentration of $Eu(NO_3)_3$ used in the reaction and the content of atomic europium obtained in the NS. The results depict a general trend where as more $Eu(NO_3)_3$ is added in the initial reaction, more atomic europium is incorporated in NS wall matrix, with a higher europium % mole being entrapped in the NS wall lining than what was used in the original solution, signifying that not all the TMOS used reacts during the sol-gel

process. In addition, it was observed that if the content of europium is too high, broken silica shells and small pieces of colloids occurred at a higher frequency and were visible in SEM images. The radius of Eu^{3+} is 1.087 Å which is much larger than the radius of Si^{4+} (0.41 Å), consequently, a high concentration of Eu^{3+} in the silica matrix or on the surface of the APS beads could hinder formation of a uniform silica shell and could

Table 2.1: Content of Europium(III) in Silica Nanoshells

100 nm APS beads template		200 nm APS beads template	
Initial content of Eu^{3+} to TMOS (%mole)	Eu^{3+} content in nanoshells (%mole)[a]	Initial content of Eu^{3+} to TMOS (%mole)	Eu^{3+} content in nanoshells (%mole)[a]
0.10	0.11	0.05	0.04
0.23	0.45	0.10	0.06
0.46	1.35	0.23	0.54
0.70	2.84	0.46	1.02

[a] From EDS analysis, compared to Si and O

account for the colloids and broken shells.

The APS core was removed by calcination from core-shell spheres at 500ºC for 24 hours. Figure 2.1 shows SEM images of Eu-SiO_2 sphere prepared using 100 nm and 200 nm APS beads after calcination and a TEM image of the 200 nm Eu-SiO_2 shells. Microscopy images confirmed the hollow shell morphology and revealed that the thickness of Eu-SiO_2 shell wall was 8-10 nm. According to the SEM pictures, the diameters of the nanoshells are 87 ± 9 nm and 179 ± 15 nm for 100 nm and 200 nm hollow shells. The shell size shrank below that of the APS template during calcination; it is hypothesized that calcination dehydrates the silica, initially forming a silica gel coating around the APS template, which results in the contracted size for the NS. The shrinkage of a gel is a common occurrence as liquid evaporates during the drying process [22]. In addition, X-Ray Diffraction (XRD) analysis was performed on dry powdered NS samples and no crystalline material was observed (Results not shown).

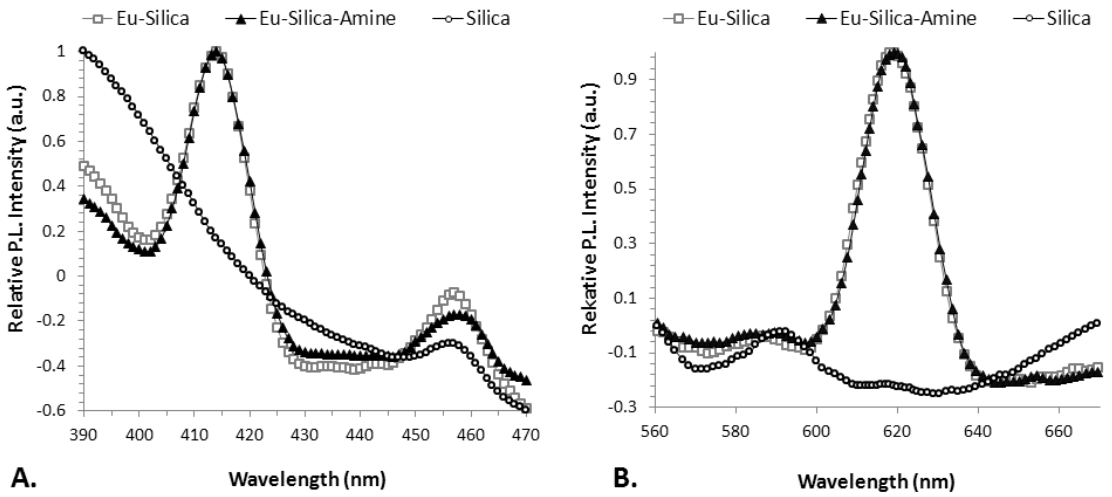

Figure 2.2: Excitation (A) and emission (B) of 100 nm silica nanoshells, europium silica nanoshells (doped with 1.35% mole europium), and europium silica nanoshells surfaced functionalized with PEI.

2.3.2 Optical Properties

Figure 2.2 shows the excitation (λ_{em} = 615 nm) and emission spectra of the 100 nm Eu-SiO_2 nanoshells containing 1.35 mole% Eu under 413 nm excitation. The ^{5}D0 emission of Eu^{3+} has five characteristic peaks, which are assigned to the $^5D_0$-^7F_J (J = 0, 1, 2, 3, 4) transitions. The strong emission centered at 615 nm can be attributed to the $^5D_0$-$^7F_2$ atomic like f-f transition [23]. Atomic emission lines dominate the luminescence of the Eu-SiO_2 and Eu-SiO_2-PEI particles, but it is not seen in the undoped SiO_2 nanoshells, signifying that the detected luminescence is due to the Eu incorporated on the NS surface.

2.3.3 Dynamic Light Scattering (DLS) and Zeta potential Measurements

Using DLS, the dispersed size of the Eu-SiO_2 nanoshells in aqueous suspension was estimated. All the concentrations of nanoshells in aqueous suspension were 3 mg/mL. After 3 h of sonication, 10 uL of suspension was diluted in 1 mL of D.I. water for size and zeta potential determinations. Table 2.2 shows the sizes and zeta potentials of core-shell spheres (non-calcined silica coated APS spheres), NS, and PEI coated NS.

The sizes measured in solution by dynamic light scattering (DLS) measurements are about double the sizes obtained from the SEM pictures. In the sol gel reaction, growing colloidal silica could crosslink between spheres and form some dimers or trimers consistent with the core-shells having a larger diameter and PDI than their templates. TEM images show the shells of some spheres fused with neighboring shells, but it is difficult to quantify the amount of aggregation with TEM or SEM. Core-shell spheres possess a negatively charged surface from the silica gel coating the APS beads. After calcination, the amino-polystyrene core was removed, which resulted in the silica shell exhibiting an even more negative surface charge, perhaps due to removal of the amino groups. The calcination also densified the silica shell and produced a smaller diameter and narrower size range. The small doping content of Eu^{3+} does not greatly affect the zeta potential of the NS.

Table 2.2: Size and Zeta Potential of Silica Nanoshells in Aqueous Suspension[a]

	Average size (nm)	PDI	Zeta potential (mV)
Core-shell spheres	225	0.35	-15
Nanoshells	157	0.22	-22
PEI coated nanoshells	185	0.25	48

[a] Test is induced using 100 nm Eu-silica nanoshells with 1.35% mole europium

Particles with positively charged surfaces should enhance binding between particles and cells. Langer etc [24] reported the zeta potential of PEI coated silica spheres could be up to +47.90 mV. A 0.1% PEI aqueous solution was employed to coat the Eu-SiO_2 nanoshells. The pKa of PEI in water is 9.6, so it is significantly protonated and readily absorbed to the negatively charged surface of Eu-SiO_2 nanoshells and trapped in the polar porous structure of SiO_2. A zeta potential of +48 mV was observed for the NS after PEI coating. The zeta potential negative to positive charge change that occurred between the non-modified NS (-22 mV) and the PEI coated NS (+48 mV) imply the presence of amine groups on the PEI coated Eu-SiO_2 particle surface. The

PEI coating only slightly increased the size of PEI modified NS compared to non-modified ones.

2.3.4 Adhesion/Endocytosis Experiments and Image Analysis

In general, cell membranes tend to have a net negative charge due to surface glycoproteins/glycosphingolipids [25] which has lead many groups to take advantage of this unique cell property by functionalized short DNA sequences [26], peptides [27], proteins [28], or NPs [29] with cationic functional groups in order to help the macromolecules or nanoparticles adhere and penetrate mammalian cells through electrostatic mediated interactions. To implement this, the surface of the Eu-SiO_2 nanoshells was functionalized with PEI. In addition, the high positive charge on the NS surface due to the surface adsorbed PEI helps prevent the aggregation of the Eu-SiO_2 nanoshells under physiological conditions [30].

The uptake of the Eu-SiO_2 NS coated with PEI was studied by two-photon (2-P microscopy) under *in vitro* cell culture conditions with HeLa cervical cancer cells. For these adhesion/endocytosis experiments Eu-SiO_2 NS with a DLS measured size of 332.7 nm (PDI: 0.202) and a zeta-potential 43.9 mV were used. As shown in Figure 2.3A, a high number of red emissive Eu-SiO_2 NS can be detected along the cell membrane of multiple HeLa cells when compared to control HeLa cells stained with CMFDA intercellular stain (Figure 2.3B). As the PEI coated particles carry a highly positive zeta potential (+48 mV, Table 2.1), electrostatic attraction of the particles to the negatively charged cell membrane could account for this observation.

In order to confirm that the red ring around the HeLa cells (Figure 2.3A) was composed of Eu-SiO_2-PEI NS and not an optical artifact, a background subtraction between the red and green images was performed using custom C#--based heat map software. Briefly, optical bleed over from any green fluorescence passed through the red fluorescence filter could falsely indicate the presence of Eu-doped NS particles. The recorded color fluorescent microscopy image was split into red, green, and blue channels and background subtraction was performed independently on each channel to remove baseline noise from the camera exposure. The intensity values of each pixel in the green fluorescence image were subtracted from each pixel in the red fluorescence image (setting any negative values to zero), leaving only intensity values above and beyond any green fluorescence in the resultant image. The remaining intensity range of

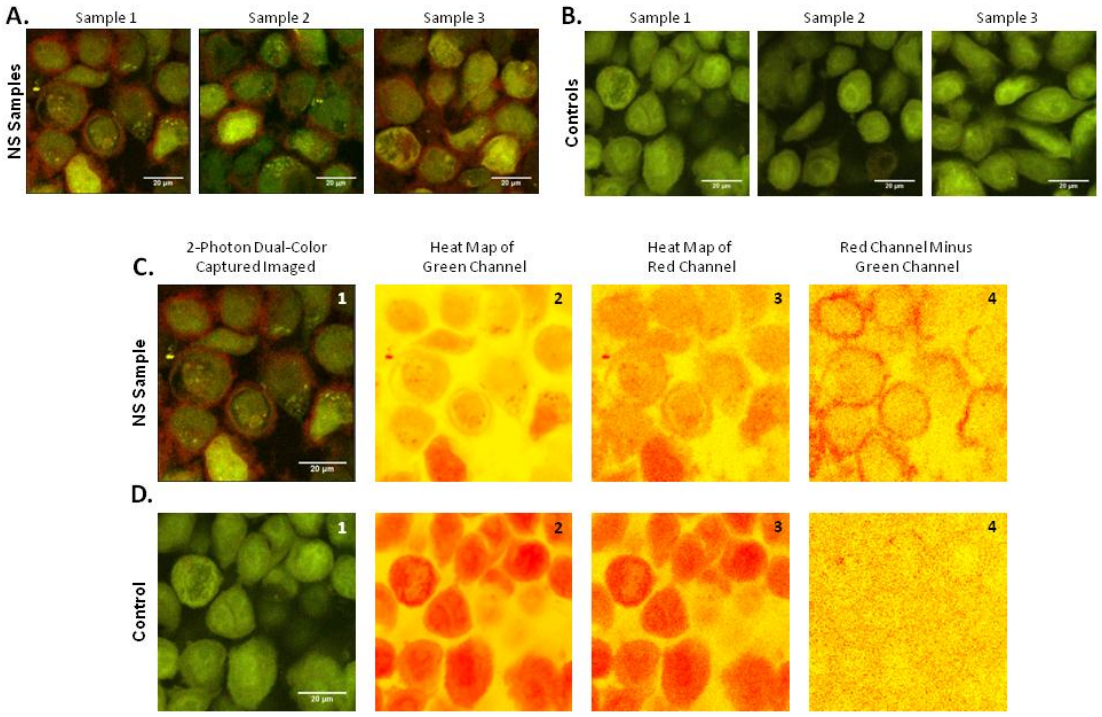

Figure 2.3: Adhesion/Endocytosis Imaging of Eu-SiO_2 NS on HeLa Cells. HeLa cells, stained with CMFDA (green), appear to have a red ring of NS around their cellular membrane when incubated with Eu-SiO_2-PEI NS (red) for 24 hrs [Panel A]. Results were confirmed by performing a background subtraction on samples incubated with [Panel C] and without [Panel D] Eu-SiO_2-PEI NS.

the image was then scaled across a red to yellow heat scale, and averaged into 2 x 2 pixel blocks for visualization purposes. In summary, this subtraction removes any optical bleed from the green channel (CMFDA cytoplasmic stain) to the red channel (Eu-doped NS particles).

As shown in Figure 2.3C-D, the original 2-P dual-color image was first separated into its individual red and green channel components, and a multiple of the green channel heat map was subtracted from its red counterpart. These results clearly show that the samples incubated with PEI-NS have a ring of nanoparticles around the majority of the HeLa cells (Figure 2.3C.4), but the control sample (Figure 2.3D.4) does not have a similar feature, which is consistent with the PEI functionalized NS having attached to the surfaces of the HeLa cells.

A luminescence ratio analysis was performed on the outer and inner regions of the cell membrane in order to distinguish between the amount of PEI-NS attached to the outer part of the membrane and those internalized by the cells. To our knowledge, this is the first time a luminescence ratio analysis has been used to demonstrate the adhesion/endocytosis of NPs onto cells. This was accomplished by using Image J to (1) creating outline areas just outside or inside the cell, based on the green cytoplasmic cell stain images on both the control and PEI-NS sample images, (2) applying these same outlines to their corresponding locations on the red channel image using the ROI manager, and (3) using the Analyze Particles/Measure tools to calculate the mean luminescence values of the outline areas, in both the green and red channels. Once the mean luminescent value of each outlines area was known, the ratio of red mean luminescence to green mean luminescence ratio was calculated for each outline.

The ratio analysis performed on the outlines just outside of cell samples incubated with Eu-SiO_2-PEI NS had a luminescence ratio of 2.58 (SD ± 0.57) [Table 2.3], while the control samples had a ratio of 0.80 (± 0.09); therefore, the samples with europium-SiO_2-PEI NS are ~ 223% more photoluminescently intense in areas around the periphery of HeLa cells than native HeLa cells. These results imply that a large number of Eu-SiO_2-PEI NS are attached to the outer membrane surface of the HeLa

cells, which is consistent with the expected electrostatic attraction of the positively charged particles to the negatively charged cell membrane. Conversely, when the ratio analysis was performed on areas located inside the cell (Figure 2.4A.5 / A.4 and Figure 2.4B.5 / B.4), it was found that the Eu-SiO_2-PEI NS samples were only ~ 34% more luminescently intense (Table 2.3), which is consistent with a small amount of Eu-SiO_2-PEI NS penetrating the cell membrane by endocytosis. It is hypothesized that the negligible amount of endocytosis is probably due to the lack of targeting to a specific membrane receptor.

Table 2.3: Emission Ratio Analysis Results

	Red Mean Luminescence / Green Mean Luminescence	**Standard Deviation**
Controls: Outlines Just Outside of Cell (n = 25)	0.80	0.087
NS Samples: Outlines Just Outside of Cell (n = 33)	2.58	0.57
Controls: Outlines Inside of Cell (n = 25)	0.80	0.03
NS Samples: Outlines Inside of Cell (n = 33)	1.07	0.17

Previous studies by Oh and colleagues [31] have proposed that optimal nanoparticle uptake into cells typically occurs with particles between the range of 50 to 200 nm, while other groups have shown that sub-100nm particles exhibit significantly greater cellular uptake compared with particles >100 nm diameter regardless of the surface composition of the particles [32-34]. Therefore, it is proposed that improved NS cellular uptake could be induced by reducing the size of the NS. In addition to size consideration, particle uptake can be enhanced by functionalizing the surface of the NS with a targeting ligand that can bind to specific cell surface receptors which can induce endosomal endocytosis. For example, previous work by Rosenholm etc [30] has shown

that folate targeted nanoparticles tend to be readily endocytosed by HeLa cells, even when the nanoparticle diameter is larger than 400 nm.

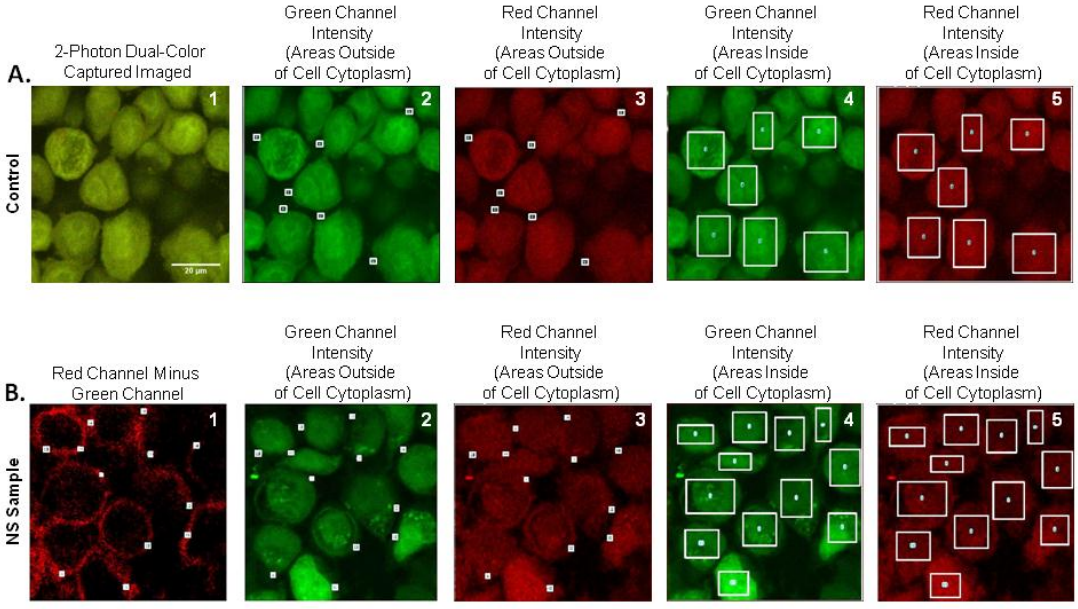

Figure 2.4: Fluorescent intensity ratio analysis of adhesion/endocytosis experiments. Panel (a), shows outline areas just outside [(a)-2 and (a)-3] or inside [(a)-4 and (a)-5] HeLa cells for a typical control sample, while Panel (b), shows similar outlines for cells incubated with Eu-SiO_2-PEI NS. Outlines on individual images that were used to determine the red to green mean luminescence ratios for each sample set are shown. The average emission intensity ratio of areas just outside the cell membrane wall was typically 223% more luminescently intense for samples incubated with Eu-SiO_2-PEI NS, when compared to HeLa cells controls stained only with CMFDA. All outlines were based on the location of the green cytoplasmic cell stain images.

2.4 Conclusions

Photoluminescent Eu^{3+} has been doped into 100 nm and 200 nm diameter sizes of silica NS through a sol-gel synthesis route and use of a polymer bead template. Removing the polymer cores by calcination produces silica NS containing less than 3 % mole europium, which emits a strong narrow red emission line at 615 nm. The long lifetime of the rare earth ion facilitates studies by 2-P microscopy. Two-photon microscopy of the europium (III) doped NS show little interaction with HeLa cells in culture media; however, when the NS were coated with PEI they acquired a high positive charge and bound to the outer surface of HeLa cancer cells with minimal

endocytosis. The ability to control nanoparticle location (cell surface vs. interior) is valuable in biosensing and drug delivery studies.

2.5 Acknowledgements

This research was supported by NIH Nanotumor Grant (NIH Grant U54 CA 119335), and we thank the California Institute of Information Technology and Telecommunication for research support. In addition, individual student funding was provided by NCI Research Supplements to Promote Diversity in Health Related Research Fellowship (NIH Grant 3U54 CA 119335-05S3), NSF - California LSAMP Bridge to the Doctorate / Louis Stokes Alliances for Minority Participation Fellowship (UCI NSF Grant HRD0115115), and NIH – ET CURE / Specialized Cancer Center Support Grant (NIH Grant 3P30 CA 023100-25S7). The NIH National Center for Microscopy and Imaging Research at UCSD is acknowledged for assistance with obtaining the TEM images.

Chapter 2 in full, is a reprint of the material as it appears in Red-luminescent Europium (III) Doped Silica Nanoshells: Synthesis, Characterization and Their Interaction with HeLa Cells in *Journal of Biomedical Optics* 2011. Yang J., Sandoval S., Alfaro J.G., Aschemeyer S., Liberman, A., Martin D.T., Makale M., Kummel A.C., Trogler W.C.; Jun;16(6) : 066012. Copyright 2011. The dissertation author was the primary researcher and author of this work.

2.6 References

1. Barbe, C., et al., *Silica particles: A novel drug-delivery system.* Advanced Materials, 2004. **16**(21): p. 1959-1966.

2. Sharrna, P., et al., *Nanoparticles for bioimaging.* Advances in Colloid and Interface Science, 2006. **123**: p. 471-485.

3. Lai, C.W., Hsiao, J.K., Chen, Y.C., Chou, P.T., *Nanomaterials for the Life Sciences*. Spherical and Anisotropic Silica Shell Nanomaterials. Vol. 3, Chapter 10. 2009: Wiley-VCH.

4. Jin, Y., Lohstreter, S., Zhao, J.X. , *Nanomaterials for the Life Sciences*. Toxicity of Spherical and Anisotropic Nano Silica. Vol. 2, Chapter 1. 2009: Wiley-VCH.

5. Lipski, A.M., et al., *Nanoscale engineering of biomaterial surfaces.* Advanced Materials, 2007. **19**(4): p. 553-+.

6. Smith, J.E., L. Wang, and W.T. Tan, *Bioconjugated silica-coated nanoparticles for bioseparation and bioanalysis.* Trac-Trends in Analytical Chemistry, 2006. **25**(9): p. 848-855.

7. Choi, H. and I.W. Chen, *Surface-modified silica colloid for diagnostic imaging.* Journal of Colloid and Interface Science, 2003. **258**(2): p. 435-437.

8. Jain, T.K., et al., *Nanometer Silica Particles Encapsulating Active Compounds:â€‰ A Novel Ceramic Drug Carrier.* Journal of the American Chemical Society, 1998. **120**(43): p. 11092-11095.

9. Kim, J., et al., *Magnetic fluorescent delivery vehicle using uniform mesoporous silica spheres embedded with monodisperse magnetic and semiconductor nanocrystals.* Journal of the American Chemical Society, 2006. **128**(3): p. 688-689.

10. Bharali, D.J., et al., *Organically modified silica nanoparticles: A nonviral vector for in vivo gene delivery and expression in the brain.* Proceedings of the National Academy of Sciences of the United States of America, 2005. **102**(32): p. 11539-11544.

11. Torney, F., et al., *Mesoporous silica nanoparticles deliver DNA and chemicals into plants.* Nature Nanotechnology, 2007. **2**(5): p. 295-300.

12. Tan, W.H., et al., *Bionanotechnology based on silica nanoparticles.* Medicinal Research Reviews, 2004. **24**(5): p. 621-638.

13. Burns, A., H. Ow, and U. Wiesner, *Fluorescent core-shell silica nanoparticles: towards "Lab on a Particle" architectures for nanobiotechnology.* Chemical Society Reviews, 2006. **35**(11): p. 1028-1042.

14. Knopp, D., D.P. Tang, and R. Niessner, *Bioanalytical applications of biomolecule-functionalized nanometer-sized doped silica particles.* Analytica Chimica Acta, 2009. **647**(1): p. 14-30.

15. Cauda, V., et al., *Multiple Core-Shell Functionalized Colloidal Mesoporous Silica Nanoparticles.* Journal of the American Chemical Society, 2009. **131**(32): p. 11361-11370.

16. Estevez, M.C., et al., *Highly Fluorescent Dye-Doped Silica Nanoparticles Increase Flow Cytometry Sensitivity for Cancer Cell Monitoring.* Nano Research, 2009. **2**(6): p. 448-461.

17. Xu, Y., et al., *Multifunctional Fe3O4 Cored Magnetic-Quantum Dot Fluorescent Nanocomposites for RF Nanohyperthermia of Cancer Cells.* Journal of Physical Chemistry C, 2010. **114**(11): p. 5020-5026.

18. Lim, Y.T., et al., *Multifunctional Silica Nanocapsule with a Single Surface Hole.* Small, 2009. **5**(3): p. 324-328.

19. Chen, L.Y., et al., *CdTe quantum dot functionalized silica nanosphere labels for ultrasensitive detection of biomarker.* Chemical Communications, 2009(19): p. 2670-2672.

20. Andelman, T., et al., *Synthesis and Cytotoxicity of Y2O3 Nanoparticles of Various Morphologies.* Nanoscale Research Letters, 2010. **5**(2): p. 263-273.

21. Yang, J., J.U. Lind, and W.C. Trogler, *Synthesis of hollow silica and titania nanospheres.* Chemistry of Materials, 2008. **20**(9): p. 2875-2877.

22. Brinker, C.J. and G.W. Scherer, *Sol-gel science : the physics and chemistry of sol-gel processing*. 1990, Boston: Academic Press. xiv, 908.

23. *Making sense of lanthanide luminescence.* Science Progress, 2005. **88**: p. 101-131.

24. Fuller, J.E., et al., *Intracellular delivery of core-shell fluorescent silica nanoparticles.* Biomaterials, 2008. **29**(10): p. 1526-1532.

25. Yacobi, N.R., et al., *Mechanisms of alveolar epithelial translocation of a defined population of nanoparticles.* Am J Respir Cell Mol Biol. **42**(5): p. 604-14.

26. Schroeder, A., et al., *Lipid-based nanotherapeutics for siRNA delivery.* J Intern Med. **267**(1): p. 9-21.

27. Daniels, D.S. and A. Schepartz, *Intrinsically cell-permeable miniature proteins based on a minimal cationic PPII motif.* J Am Chem Soc, 2007. **129**(47): p. 14578-9.

28. Frankel, A.D. and C.O. Pabo, *Cellular uptake of the tat protein from human immunodeficiency virus.* Cell, 1988. **55**(6): p. 1189-93.

29. Hong, S., et al., *Interaction of poly(amidoamine) dendrimers with supported lipid bilayers and cells: hole formation and the relation to transport.* Bioconjug Chem, 2004. **15**(4): p. 774-82.

30. Rosenholm, J.M., et al., *Targeting of porous hybrid silica nanoparticles to cancer cells.* ACS Nano, 2009. **3**(1): p. 197-206.

31. Oh, J.M., et al., *Inorganic metal hydroxide nanoparticles for targeted cellular uptake through clathrin-mediated endocytosis.* Chem Asian J, 2009. **4**(1): p. 67-73.

32. Slowing, I., B.G. Trewyn, and V.S. Lin, *Effect of surface functionalization of MCM-41-type mesoporous silica nanoparticles on the endocytosis by human cancer cells.* J Am Chem Soc, 2006. **128**(46): p. 14792-3.

33. Desai, M.P., et al., *The mechanism of uptake of biodegradable microparticles in Caco-2 cells is size dependent.* Pharm Res, 1997. **14**(11): p. 1568-73.

34. Prabha, S., et al., *Size-dependency of nanoparticle-mediated gene transfection: studies with fractionated nanoparticles.* Int J Pharm, 2002. **244**(1-2): p. 105-15.

Chapter 3. Europium Doped TiO_2 Hollow Nanoshells: Two-Photon Imaging of Cell Binding

A simple scalable method to fabricate luminescent monodisperse 200 nm europium-doped hollow TiO_2 nanoshell (NS) particles is reported. Fluorophore reporter, Eu3+ ions are incorporated directly in the NS matrix, leaving the surface free for functionalization and the core free for payload encapsulation. Amine-functionalized polystyrene beads were used as templates, and the porous walls of europium-doped titania nanoshells were synthesized using titanium(IV) t-butoxide and europium(III) nitrate as reactants. X-ray diffraction analysis identified anatase as the predominant titania phase of the rigid nanoshell wall structure, and photoluminescence spectra showed that the Eu(III)-doped TiO2 nanoshells exhibited a red emission at 617 nm due to an atomic f−f transition. Nanoshell interactions with HeLa cervical cancer cells in vitro were visualized using two-photon microscopy of the Eu(III) emission and studied using a luminescence ratio analysis to assess nanoshell adhesion and endocytosis.

3.1 Introduction

Titania nanomaterials and hybrid derivatives have attracted interest because of their broad range of industrial applications, such as in photovoltaic devices [1, 2], chemical/gas sensors [3], catalysis [4, 5], wastewater treatment [6, 7], and in filtration and sorption media [8]. Titania nanomaterials and their compound hybrid composites are also intriguing for medical applications [9-15], and several studies of applications in anticancer research [16-19] have appeared. When TiO_2 nanoparticles undergo photoexcition with ultraviolet (UV) light, photoinduced electrons and holes are produced. These electrons and holes can react with hydroxyl ions or water to produce reactive hydroxyl radicals •OH and perhydroxyl radicals HO_2•. These oxygen species not only react with organic wastes in the environment and decompose them into non-

toxic molecules, but are also highly reactive with cells and can cause DNA strand breaking through genotoxicity [16, 20]. This characteristic gives titania nanomaterials the potential to be used as photodynamic therapy agents in cancer treatments [21, 22]. Furthermore, the use of various titania and hybrid titania nanocomposites made up of gold [23], silver [24], copper [25], platinum [17, 26], and iron cooperatives [12], as well as titania nanoparticles combined with specific antibodies [27], have been shown to have cancer therapeutic potential typically via photodynamic therapy or magnetic therapy (Fe composites).

Several methods have been described for the synthesis of TiO_2 nanospheres. Caruso and co-workers [28, 29] used a layer-by-layer (L-b-L) self-assembly technique to fabricate both SiO_2 and TiO_2 hollow spheres. For the TiO_2 spheres, a positively charged TiO_2 colloid was used to form a shell around polymer templates through the absorption of polyelectrolytes. Repeated absorption of polyelectrolytes and TiO_2 precursors increased the thickness and integrity of the shell wall. Xia et al. [30] prepared hollow TiO_2 spheres by using crystalline arrays of polystyrene beads as a template. Well-defined TiO_2 spheres could be fabricated from these methods, but multiple steps are needed, which makes these methods challenging for the large-scale fabrication needed in biomedical applications. Similar templating methods using activated carbon [31] or polymers [32-35] as cores have also been reported. Alternative methods, such as ultrasonic spray pyrolysis [36], diffusion flame synthesis [37], and supercritical fluid methods [38, 39] have been used as potentially scalable routes to create TiO_2 spheres, these processes tend to produce nanoparticles with a wide range of sizes and/or have fragile shell structures.

Another active research area has been the development of nanoparticles that incorporate rare-earth ions within their structures. Rare-earth materials have attractive properties that include increased photostability, reduced light scattering, narrow emission spectra, large emissive Stokes shifts and long luminescence lifetimes and allow for simple functionalization strategies.[40, 41] Europium is particularly advantageous because europium(III) ions produce red photoluminescence with narrow

atomic emission profiles when doped in inorganic lattices. Due to its high transparency to visible light and its robust thermal, chemical, and mechanical properties [42-44], titania is an ideal host material for Eu^{3+}, and several Eu^{3+}-doped TiO_2 films, nanocrystals, and particles have already been reported.[42, 43, 45-54] Furthermore, europium provides an inexpensive, long lifetime, low cytotoxicity, and safe method for fluorescence imaging compared to organic fluorophores.[40, 55] The high efficiency of reactive oxygen production during near-UV irradiation of TiO_2 leads to enhanced photobleaching of organic dyes [56] in aerobic environments.

This paper describes a simple method of synthesizing uniform monodispersed europium(III)-doped hollow TiO_2 nanoshells (NSs) that have rigid porous shell walls. The utility of this NS design is that the long-lived fluorophore reporter, Eu^{3+} ions are incorporated directly in the NS matrix, leaving the surface free for functionalization and the NS core free for payload encapsulation. Amine-functionalized polystyrene (PS) beads were used as templates in the synthesis. Titanium(IV) *t*-butoxide was used as the precursor for titania deposition to reduce the rate of hydrolysis and suppress nontemplated growth. The sol-gel hydrolysis of titanium(IV) *t*-butoxide was catalyzed on the surface of amine-functionalized PS beads to form a thin porous titania coating. Doping was effected by using ethanol solvent containing 5% water and dissolved europium(III) nitrate. After removing the PS core by calcination, hollow nanoporous TiO_2 NSs with red luminescence characteristic of doping by Eu^{3+} were isolated. This protocol provides a simple, inexpensive, and scalable method to prepare Eu^{3+}-doped titania NSs for imaging studies. These nanoshells were coated with a cationic polymer, poly(ethylenimine) (PEI), to alter the surface charge from negative to positive, which allowed the NS to adhere to HeLa cervical cancer cells. Cell to NS interactions were imaged using two-photon (2-P) microscopy and quantified using a previously reported luminescence ratio analysis.[57]

3.2 Experimental Methods and Materials

3.2.1 Materials

Titanium *t*-butoxide, europium(III) nitrate hydrate, and poly(ethylenimine) (PEI – MW 750000) were obtained from Aldrich-Sigma Ltd. The 200 nm amine functionalized polystyrene beads (2.5% w/w) were purchased from PolySciences Ltd. HeLa cervical cancer cells were purchased from ATCC (Manassas, Virginia); Dulbecco's Phosphate Buffer Saline solution (DPBS 1 ×), Dulbecco's Modified Eagle's Medium (DMEM), and fetal bovine serum (FBS) were purchased from Mediatech, Inc. (Manassas, Virginia). Media supplements, chloromethylfluorescein diacetate (CMFDA) CellTracker Green intracellular stain, and Prolong Gold were obtained from Invitrogen (Carlsbad, California). Nunc Lab-Tek II 4-well chamber slides and Paraformaldehyde (PFA) were purchased from ThermoFisher Scientific (Fair Lawn, New Jersey). All chemicals and reagents were used as received or as described by in manufacturer protocols, unless otherwise stated.

3.2.2 Preparation of Europium-Doped Hollow Titania Nanoshells

In a 2 mL Eppendorf tube, 0.25 mg of $Eu(NO_3)_3 \bullet 5H_2O$ was dissolved in 1.25 mL of absolute ethanol. A 50uL portion of a 2.5% weight dispersion (in water) of 200 nm aminopolystyrene beads was added. Next 25 uL of 1 M titanium(IV) t-butoxide/ethanol solution was added, and the mixture was stirred in a vortex mixer for 5 min at room temperature at a setting of 900 rpm. The suspended core-shell nanospheres were collected by centrifugation, washed with ethanol, and dried in vacuum for 48 h at room temperature to give 1.90 mg of core-shell spheres.

The aminopolystyrene bead core was removed by the preceding nanospheres by heating in air at 5 °C per minute to 500 °C and maintaining this temperature for 24 h. About 0.85 mg of europium-doped hollow TiO_2 NSs were recovered as a white powder. Energy-dispersive X-ray spectroscopy (EDS) showed the Eu content of this preparation was 0.84% (mol %).

3.2.3 Modification of Eu/TiO_2 Hallow Nanoshells with Poly(ethylenimine)

To increase the cell-adhering efficiency of Eu/TiO_2 nanoshells, the NS surface charge was changed from negative to positive using poly(ethylenimine) (PEI). This was accomplished by suspending 3 mg of Eu/TiO_2 NS in 1.5 mL of 0.1 mg/mL PEI water solution. The suspension was stirred for 2 h; nanoshells were collected by centrifugation and washed with water. Subsequently, the PEI-coated NSs were suspended in 1.0 mL of DPBS for use in cell imaging experiments.

3.2.4 Characterization of Eu/TiO_2 Hallow Nanoshells

The scanning electron microscopy (SEM) and EDS measurements were conducted on a FEI/Philips XL30 FEG ESEM microscope with an accelerating voltage of 10 kV. The average diameter of the NS was determined from SEM images. Transmission electron microscopy (TEM) images were obtained with the use of a JEOL-2000EX (200 kV) cryo-electron microscope with an accelerating voltage of 200 kV. A Perkin-Elmer LS 45 luminescence spectrometer was used to record luminescence emission and excitation spectra. A Zetasizer Nano ZS (Malvern Instruments) was used to measure the dynamic light scattering (DLS) size distribution, the polydispersity index (PDI), and zeta potential of NSs when suspended in distilled water with gentle sonication and vortexing. X-ray powder-diffraction patterns were obtained using a Bruker Discover D8 X-ray diffractometer with a rotating anode Cu K α ($\lambda = 0.154$ nm) source.

3.2.5 Cell Culture

HeLa cervical cancer cells (5×10^4) in Dulbecco's Modified Eagle's Medium (DMEM) supplemented with 10% FBS, 1% antibiotics (penicillin, streptomycin, glutamine (PSG)), and 1% sodium pyruvate were plated per well on Nunc Lab-Tek II 4-well chamber slides at 37 °C in a humidified atmosphere of 5% CO_2. HeLa cells were allowed to grow to 60-80% well confluence before beginning cell adhesion/endocytosing experiments.

3.2.6 Cell Adhesion/Endocytosis Experiments

HeLa cells were incubated with 500 μg/mL of europium-TiO_2 NS functionalized with PEI for 24 h in DMEM complete media at 37 °C in a humidified atmosphere of 5% CO_2. Cells were then washed 2 times with DPBS and labeled with 2.5 μM CMFDA CellTracker Green intracellular stain in DPBS for 30 min. Cells were washed 3 times with DPBS to remove any surplus dye, fixed with 4% PFA in DPBS solution, washed 2 times more with DPBS, and covered with Prolong Gold antifade reagent to prepare samples for visualization by two-photon microscopy.

3.2.7 Two-Photon (2-P) Microscopy of HeLa Cell Interactions with Europium-Doped Nanoshells *In Vitro*

2-P fluorescence dual color (red/green Europium TiO_2 NS/CMFDA) images were obtained with a custom-modified Nikon FN1 intravital microscope fitted with a 60x water immersion objective (Nikon, 1.2 NA). The instrument was driven by a Spectraphysics MaiTai Ti:Sa 3 W, 120 fs pulsed laser tuned to 705 nm. The microscope operated in nondescanned mode. Emitted sample light was separated into red/green channels using a beam splitter and band-pass filters (Chroma ET620/60 and ET510/50). Two side-on PMTS (Hamamatsu) captured the light, and the raster scan data were assembled and saved using Nikon EZ-1 display/analysis software. Full-field images were initially acquired full field at 60x, with constant gain settings between samples, and regions of interest (ROIs) were magnified 3.56x by spatially compressing the raster scan. To confirm the location of the NS, image volumes composed of multiple 1 μm XY slices were acquired serially along the sample z-axis. 2-P images were further processed for background level and SNR, using Image J (NIH, Bethesda, MD).

3.3 Results and Discussion

3.3.1 Synthesis of Eu^{3+}-Doped Hollow Titania Nanoshells

Sol-gel reactions are often used to fabricate amorphous inorganic oxides.[58] While primary alkoxysilanes can be hydrolyzed in water slowly, the hydrolysis of primary alkoxylates of titanium (IV) in water is too rapid to use in templating reactions. Therefore, bulky *t*-butoxy groups were employed to slow the rate of hydrolysis, and a solution of ethanol/5% water was used as the reaction medium to reduce the water concentration. These techniques yielded a hydrated titania sol-gel coating on the amine-functionalized PS beads (Figure 1A and 1B) due to either the negatively charged, partially hydrolyzed precursor derived from $Ti(O\text{-}t\text{-}Bu)_4$ being absorbed by the cationic amino group (partially protonated in water) on the surface of the PS beads or by the basic surface amines catalyzing sol-gel hydrolysis. An effort to use plain PS beads to template the TiO_2 sol-gel reaction was also attempted, but after the mixture was stirred for 48 h, it was found that no solid shell formed on the nonfunctionalized PS surface.

Different amounts of $Ti(O\text{-}t\text{-}Bu)_4$ were added during the synthesis, and it was found that an excess did not increase the thickness of the titania shell but instead resulted in the formation of colloidal byproduct. The optimal ratio of titanium(IV) *t*-butoxide to PS beads was determined to be between 4:1 and 8:1 by weight. With a ratio less than 4:1, the titania coverage on the surface of PS beads was found to be nonuniform and produced many broken nanoshells after calcination. At a ratio above 8:1, extensive colloidal TiO_2 byproduct contaminated the core-shell nanospheres. This suggested that the growth of the titania shell stopped when the surface of PS beads was covered by a uniform layer of titania. Furthermore, it was observed after calcination that when excess colloidal titania byproduct was present this leads to polydisperse batches according to DLS measurements.

The PS beads within each core-shell nanosphere were removed by calcining at 500 °C for 24 h. The isolated hollow shells (Figure 3.1C) were collected and resuspended in ethanol, and a droplet of this solution was used to analyze the NSs with SEM and TEM. The SEM images show no distinguishable shape differences between the formed hollow TiO_2 spheres doped with and without europium. After calcination there were very few broken undoped hollow TiO_2 spheres, and some broken Eu^{3+}-doped

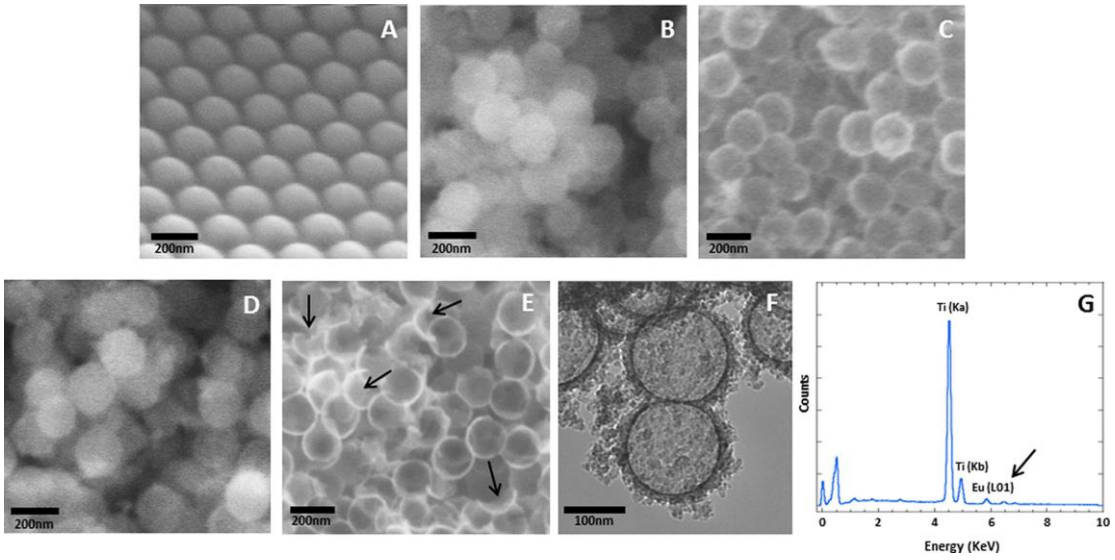

Figure 3.1: SEM and TEM Images of 200 nm plain and europium-doped titania nanoshells prepared using 0.025% $Eu(NO_3)_3 \cdot 5H_2O$. A: SEM images of amino polystyrene templates, B: Nondoped TiO_2 core-shells, C: Plain TiO_2 hollow NS, D: Eu^{3+}-doped TiO_2 core-shells, and E: Eu^{3+}-doped TiO_2 hollow NS. Small amounts of broken shells in the europium-doped image are identified by black arrows in E; F: TEM image of europium-doped TiO_2 hollow NS showing some colloidal TiO_2 fused onto the outer NS surface; G: EDS spectrum analysis of Eu^{3+}-doped TiO_2 hollow NS showing X-rays characteristic of both Ti and Eu.

spheres can be spotted in their respective image sets (Figure 3.1C and 3.1E). The wall thickness of the undoped titania NS was found to be as thin as 5-10 nm and the results suggest that the doping with Eu^{3+} leads to a more fragile TiO_2 shell wall and, therefore, some broken europium-doped NSs. The TEM image (Figure 3.1F) reveals that small amounts of colloidal TiO_2 are fused onto the outer NS surfaces, which was a typical occurrence after the critical shell thickness forms around the aminopolystyrene template.

While preparing the europium-doped titania NS, different concentrations from 0.01% to 0.035% of $Eu(NO_3)_3 \bullet 5H_2O$ were dissolved in ethanol before adding the aminopolystyrene beads and $Ti(O\text{-}t\text{-}Bu)_4$ to examine how the amount of $Eu(NO_3)_3 \bullet 5H_2O$ affects the nanoshell synthesis. During the templating reaction, with increasing concentration of $Eu(NO_3)_3 \bullet 5H_2O$ the amount of Eu^{3+} trapped in the titania lattice increased, but the NS yield decreased. The percentage doping of Eu^{3+} in the hollow spheres was confirmed using EDS. Figure 3.1G shows a typical EDS spectra of NS doped with europium(III). Furthermore, when more than 0.035% $Eu(NO_3)_3 \bullet 5H_2O$ was added during synthesis, it was discovered that templated core-shells were not produced even after 1 h of vortex mixing. The ionic radius of Eu^{3+} (1.087Å) [59] is significantly greater than that of Ti^{4+} (0.745Å) [60]. It is expected that during polycondensation Eu^{3+} is attracted to the growing anionic TiO_2 shell, and at higher concentrations, the significantly larger Eu^{3+} hinders polycondensation and blocks shell growth. Table 3.1 shows the yield of NS formation and the amount of europium(III) found doped within the different synthesized titania nanospheres batches using the various concentrations of $Eu(NO_3)_3 \bullet 5H_2O$ added during the synthesis process. Therefore, to maintain a high NS yield and hollow shell uniformity, it is necessary to limit the amount of $Eu(NO_3)_3 \bullet 5H_2O$ added during the sol-gel reaction.

Table 3.1: Yield of Hollow TiO_2 Nanoshells and Their Europium Content.

Percentage of $Eu(NO_3)_3 \cdot 5H_2O$ (%)[1]	**0**	**0.005**	**0.015**	**0.025**	**0.03**	**0.035**
Yield % of hollow titania NSs[2]	100	93	82	65	31	~0
Theoretical mole percent of Eu(III) in NS[3]	0	0.47	1.40	2.33	2.80	3.26
Mole percent of Eu(III) in NSs from EDS	0	0.22	0.34	0.84	1.13	-

[1]Mass percentage of added $Eu(NO_3)_3 \cdot 5H_2O$ used in the synthesis in ethanol/5% water as wt % of the total solvent.

[2]Ratio of hollow europium-titania particles compared with the amount of titania particles obtained by synthesis without added europium (w/w). In this series of experiments, the ratio of titanium(IV) *t*-butoxide versus PS beads is a constant 6.5:1 (w/w) as the added Eu^{3+} increases.

[3]Ratio of added $Eu(NO_3)_3 \cdot 5H_2O$ compared with added titanium(IV) *t*-butoxide in the sol-gel reaction.

3.3.2 Electron Microscopy and Dynamic Light Scattering Measurements

Using SEM images (Figure 3.1), it was found that the average diameter of hollow TiO_2 NSs was slightly smaller than their 200 nm starting PS templates. The size of core-shell and hollow Eu^{3+}-doped TiO_2 spheres (doped with 0.025% $Eu(NO_3)_3 \bullet 5H_2O$ in this set of results) was measured and compared (Table 3.2). The average diameters of core-shell spheres and hollow spheres were found to be 200 ± 5 nm and 185 ± 6 nm, respectively (n=30). After calcination, the TiO_2 shells shrunk by more than 10 nm. This result is consistent with previously measurements of silica nanoshells prepared by a similar template synthesis protocol [61]. This shrinking likely arises from the dehydration of the TiO_2 sol-gel and partial formation of the anatase mineral phase on heating. It is known that dehydration is a common occurrence during the sol-gel drying process [62]. Shrinking is believed to be isotropic as the shells are uniform in size and shape in the SEM images.

Table 3.2: Average Diameters of Eu^{3+}-Doped Core-shell and Hollow Nanoshells from SEM Images[1].

Sample	Average Diameter (nm)	Standard Deviation (nm)
Eu^{3+}-Doped Core-Shells[1]	200	5
Eu^{3+}-Doped Hollow NS[1]	185	6

[1]Eu-doped particles were prepared using 0.025% $Eu(NO_3)_3 \cdot 5H_2O$ during synthesis. Average diameters were calculated by measuring 30 nanospheres in the SEM images.

After their dispersal in solution, solution sizes and zetapotentials of core-shells and hollow Eu^{3+}-doped TiO_2 spheres were also determined using dynamic light scattering (DLS). The NSs were suspended at a concentration of 1 mg/mL in distilled water (pH 6.5) and were dispersed using a Misonix ultrasonic liquid processor (XL-2000 Series) operating at 5 W with a continuous setting for 60 s at a temperature of 4 °C, before the scattering measurements were taken. The DLS showed average diameters of 305 ± 80 nm (PDI: 0.27) and 310 ± 60 nm (PDI: 0.24) for the doped core-shell and doped hollow NSs, respectively. Their corresponding zeta potentials were 5 mV and -23 mV. Since the aminopolystyrene beads have a measured zeta potential of -33 mV, these results suggest that Eu^{3+} accumulates on the surface of the core-shell spheres, with the europium(III) ions eventually being incorporated into the titania lattice on calcination. Core-shell and hollow TiO_2 spheres without Eu^{3+} doping were also measured with DLS. Their respective diameters using intensity-weighted averaging were found to be 250 ± 40 nm (PDI: 0.22) and 240 ± 40 nm (PDI: 0.23), while their zeta potentials were measured at -44 mV and -41 mV. The DLS measurements of the aqueous suspensions exhibit slightly increased average hydrodynamic sizes from those determined by SEM measurements, which suggests that the TiO_2 NSs in solution disperse largely as monomers and a small fraction of aggregates; however, the nonideal optical properties of the nanoparticles (a uniform refractive index is assumed in fitting the correlation function) may also distort the measurements. The hollow Eu^{3+}-doped TiO_2 NSs were slightly larger than their nondoped TiO_2 NS counterparts. This may be

due to the lower zeta potential value of the Eu^{3+}-doped NS, since lower zeta potential values have been shown to correlate with a higher tendency of aggregation.[63]

DLS was used to analyze the PEI-coated Eu/TiO_2 hollow NS; these particles had an average size of 355 ± 75 nm (PDI: 0.24) with a zeta potential of +46 mV. This indicates that cationic PEI is strongly bound to the negative Eu/TiO_2 NS surface by electrostatic forces, consequently converting the surface charge from negative to positive. In addition, the high positive charge on the PEI-coated NS suggests that the NSs have good stability in aqueous solution [64], and the low PDI value suggests that the NSs are predominantly monodispersed and that colloidal debris contributes minimally to the sample population.[65] The increase of size from noncoated to PEI-coated NSs can be attributed to the polymer coating (750000 MW) as the polyoxamer corona surrounding PEI in water has been observed to increase the apparent size when compared to direct measurements (e.g., AFM) of size.[66] A summary of the average diameters of core-shell and hollow NSs measured by DLS analysis can be seen in Table 3.3.

Table 3.3: Dynamic Light Scattering Measurements of Eu^{3+}-Doped and Undoped Core-shell and Hollow Nanoshells[1].

Sample	Avg. Hydrodynamic Diameter (nm)	Standard Deviation (nm)	PDI (± SD)	Zeta Potential (mV)
Aminopolystyrene (PS) Beads	208	4	0.04 ± 0.01	-33
Nondoped Core-Shells	250	40	0.22 ± 0.04	-44
Nondoped Hollow NS	240	40	0.23 ± 0.07	-41
Eu^{3+}-Doped Core-Shells	305	80	0.27 ± 0.05	+5
Eu^{3+}-Doped Hollow NS	310	60	0.24 ± 0.05	-23
PEI-Coated Eu^{3+}-Doped Hollow NS	355	75	0.24 ± 0.02	+46

[1]Europium doped NS were prepared using 0.025% $Eu(NO_3)_3 \cdot 5H_2O$ during the synthesis. The average hydrodynamic diameter was based on DLS measurements of three different batches.

3.3.3 X-Ray Diffraction Measurements

XRD spectra of undoped TiO_2 hollow spheres and various Eu-doped TiO_2 hollow NSs are shown in Figure 3.2. The diffraction pattern matches the International Center for Diffraction Data (ICDD) sample card 00-001-0562 (shown as vertical lines in Figure 3.2), which identifies anatase as the predominant titania phase (comparison with ICDD data for the rutile and brookite phases shows that the strongest peak in both is missing) within the NS wall structure. Unmarked peaks have been attributed to the sample holder, and the diffuse background below 35^o has been identified as background from the Petrol used to mount the powder. It is observed that the crystalline phase is disturbed by doping Eu^{3+}, as peak broadening is observed for the anatase phase in the presence of small amounts of Eu^{3+}. This is consistent with structural doping in the lattice by Eu(III) and disruption of the anatase crystal order, rather than merely Eu(III) coating the surface of the titania NS, which would be expected to still show diffraction features of anatase for the underlying TiO_2.

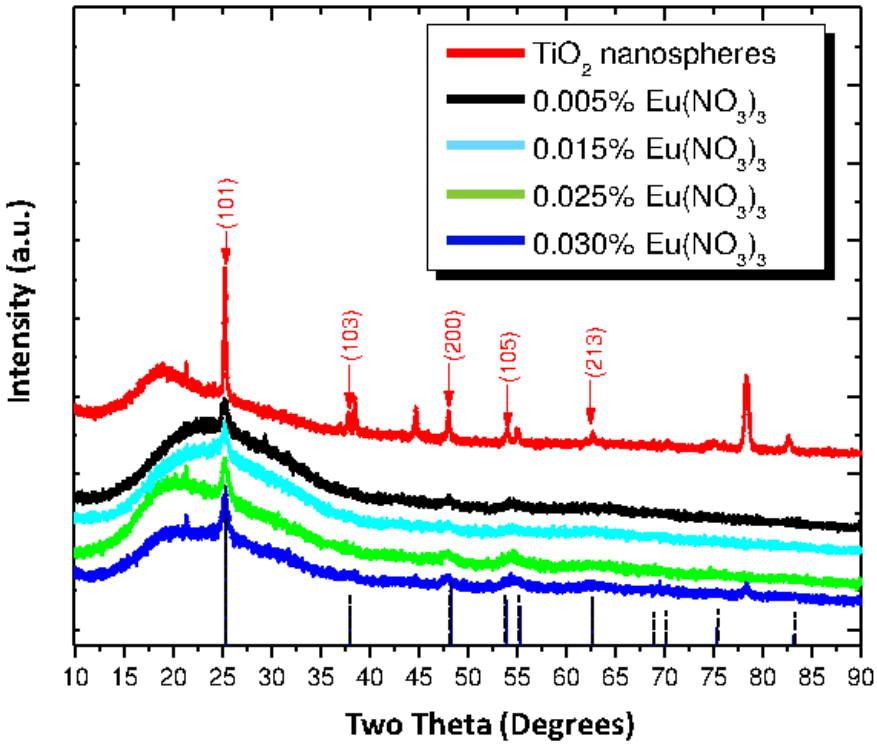

Figure 3.2: X-ray Diffraction Patterns of Thin Films of Plain and Eu^{3+} Doped TiO_2 Hollow Nanoshells. The percentages shown are the mass percent of $Eu(NO_3)_3 \cdot 5H_2O$ used during the sol-gel synthesis.

3.3.4 Optical Properties

Figure 3.3 compares the photoluminescence spectra (λ_{ex} = 413 nm) of core-shell and hollow nanoshells made with the same amount of added $Eu(NO_3)_3 \cdot 5H_2O$. The $^5D_0$ emission of Eu^{3+} has five characteristic peaks, which are assigned to the $^5D_0$-$^7F_0$, $^5D_0$-$^7F_1$, $^5D_0$-$^7F_2$, $^5D_0$-$^7F_3$, and $^5D_0$-$^7F_4$ transitions. The emission of Eu^{3+}-doped TiO_2 spheres was dominated by the red emission peak at 617 nm, which is associated with the $^5D_0$-$^7F_2$ atomic-like f-f transition [67]. There were no other strong emission peaks in the photoluminescence spectra. The emission intensity at 617 nm from calcined hollow NSs was much greater than that of the core-shell spheres having the same content of Eu^{3+}. These results are in agreement with several reports [68-71] which have also shown emission intensity increases in rare earth elements doped in TiO_2 nanoparticles after calcination at ~500 °C. This was attributed to the structure of TiO_2. After

calcination at 500 °C, TiO_2 is primarily a mixture of anatase and amorphous phases. It has been suggested [72] that this semicrystalline TiO_2 structure is an excellent host for Eu^{3+}. The TiO_2 nanocrystallite acts as an antenna, and the UV energy it absorbs is transferred to Eu^{3+}, which sensitized Eu^{3+} luminescence [72, 73]. Calcination at temperatures above 500 °C converts TiO_2 to the rutile phase, which causes the Eu^{3+} luminescence emission to disappear [73, 74]. Since europium-doped TiO_2 nanoshells emit by an atomic f-f transition, this offers the possibility to detecting and visualizing their interactions with cells using two-photon (2-P) microscopy, which is an attractive technique for *in vitro* and *in vivo* biological imaging since background 2-P bioluminescence is minimal [75-77].

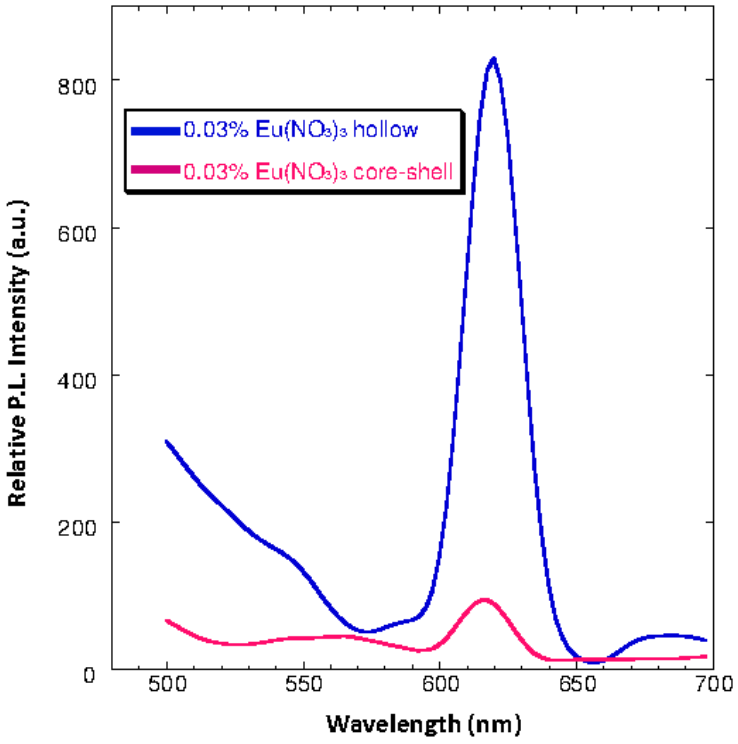

Figure 3.3: Photoluminescence Spectra of Eu3+ Doped Core-shell and Hollow Nanoshells. The percentages showed in legend are the mass percent of $Eu(NO_3)_3 \cdot 5H_2O$ used during the sol-gel synthesis.

3.3.5 Endocytosis Experiments

The outer cell surface contains sialic acids, which causes most mammalian cells to have a net anionic surface charge [78, 79]. Due to this phenomenon, surface functionalized or coated cationic groups on the surface of microbeads, macromolecules, or nanoparticles cause attachment to cells via electrostatic interactions [80-86]. For this reason, Eu-TiO_2 NSs were coated with PEI.

The adhesion and uptake of europium-doped TiO_2 NSs coated with PEI by HeLa cervical cancer cells under *in vitro* cell culture conditions was studied and visualized by 2-P microscopy. The cells were marked with a green fluorescent CMFDA intracellular 2-P stain. Hollow Eu-TiO_2 NSs prepared using 0.025% $Eu(NO_3)_3 \cdot 5H_2O$ during the synthesis reaction (DLS measured average diameter size of 342 nm and a zeta potential of +46 mV) were employed.

As shown in Figure 3.4, cells incubated with Eu-TiO_2 PEI NSs exhibit a high concentration of red luminescent material surrounding the HeLa cells, while samples incubated with noneuropium-doped TiO_2 PEI-functionalized NSs did not and resembled the control HeLa cells. Control samples incubated with noneuropium-doped TiO_2 PEI NSs probably an amount of NSs surrounding HeLa similar to the samples incubated with Eu-TiO_2 PEI NSs but are not visible via 2-P microscopy because these NS lack red luminescencent Eu^{3+}. These imaging results confirm 2-P imaging of the doped nanoparticles and suggest that the red particulates observed around HeLa cells arise due to electrostatic interactions between the positive charged PEI-functionalized Eu-TiO_2 NS and the negatively charged glycoproteins found on the cell membranes.

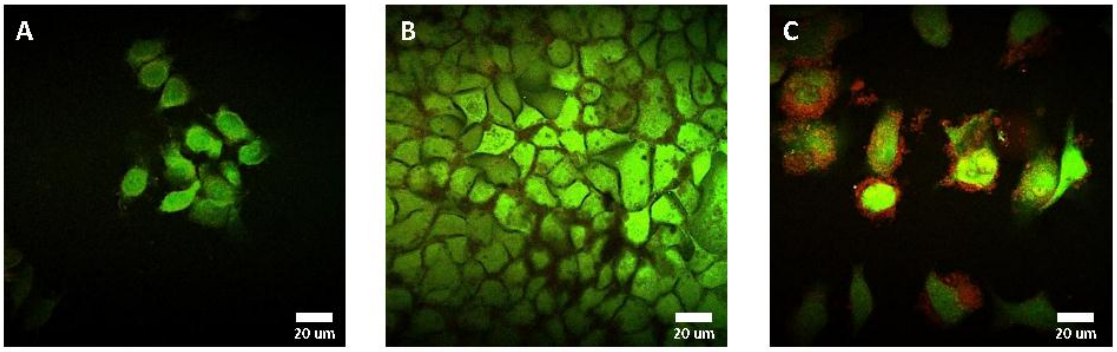

Figure 3.4: Two-Photon Microscopy Images of Non-Doped and Eu Doped 200 nm TiO_2 Nanoshells Incubated with HeLa Cells. A: HeLa cells, stained with CMFDA (green) dye; B: HeLa cells incubated with 500 µg/mL of undoped TiO_2 PEI-coated NSs for 24 h; C: HeLa cells incubated with 500 µg/mL of Eu-TiO_2-PEI NS (red) for 24 h (0.025% $Eu(NO_3)_3 \cdot 5H_2O$). Identical settings and gains were used across all microscopy images.

To quantify and confirm that these red particle features were due to europium-doped TiO_2 NSs and not an optical artifact or bleed over effect from the green dye, the 2-P dual color captured images were split into their individual red, green, and blue channel components, and an image subtraction between each sample's red and green images was performed using Image J software. The intensity of each pixel in the green fluorescence image were subtracted from each pixel in the red fluorescence image (setting any negative values to zero), leaving only intensity values above and beyond any green fluorescence in the resultant image. As shown Figure 3.5, the resulting subtracted image for cells incubated Eu-TiO_2 PEI NSs shows a distinct pattern of red luminescence around the outside of the HeLa cells. Conversely, the cells only and cells incubated with nondoped TiO_2 PEI NS samples do not exhibit this red circumference. Being that all cell samples were prepared and captured using the same settings, these results establish that this effect is due to the cell adhesion of red-emitting PEI-functionalized Eu-TiO_2 NSs onto the HeLa cell surface. Furthermore, the red luminescence pattern exhibits variations in thickness, which suggests there are one or multiple NS layers on the cell surface. This is consistent with previous results showing a similar thick multilayered nanoparticle surface adhesion pattern under confocal microscopy [87, 88] or SEM analysis [89] when nanoparticle endocytosis is not

favored. Whether endocytosis occurs can depend on the cell type [90-94], nanoparticle size [95-100], nanoparticle shape [87, 97, 101-103], and/or presence of ligands on the nanoparticle surface that facilitate cell surface receptor mediated pathways.[104-108]

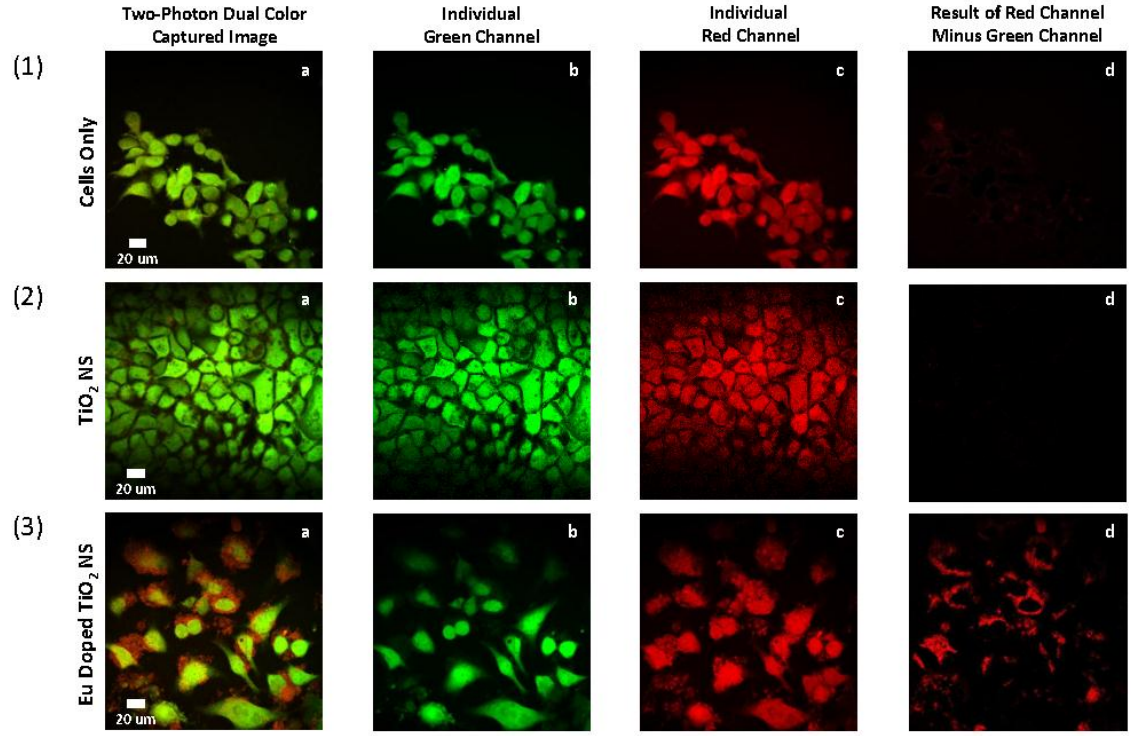

Figure 3.5: Imaging of 200 nm Eu-doped TiO_2 Nanoshells Adhering to HeLa Cells. Two-photon dual colored captured images of cell only samples (Panel 1) and cell samples incubated with 500µg/mL of TiO_2-PEI NS (Panel 2) or Eu-TiO2-PEI NS (Panel 3), were split into their individual green and red image components (1.b/1.c, 2.b/2.c, and 3.b/3.c) and a background subtraction between these images was performed (1d, 2d, 3d) using Image J.

A luminescence ratio analysis was also performed on the outer and inner regions of the cell membrane to distinguish between the amount of PEI NS attached to the outer part of the membrane and those internalized by cells. This use of the red to green luminescence ratio to establish NS adhesion/endocytosis has been described [57]. Briefly, the luminescence ratio analysis was performed using Image J to first create cytoplasmic cell outlines to determine the extent of NS internalization by cells or locationization in small rectangular regions just outside the green CMFDA stain cells to demonstrate NS cell adhesion (Figure 3.6). The cell outlines were based on the

individual green channel images and were applied to the same location/coordinates on their red channel counterparts by using the region of interest (ROI) manager in Image J. The Image J analyze/measure tools were used to determine the mean luminescence values inside the cell outlines or in rectangular regions just outside the cells for both the green and red channels, which in turn were used to calculate the red to green luminescence ratio inside or just outside the cells.

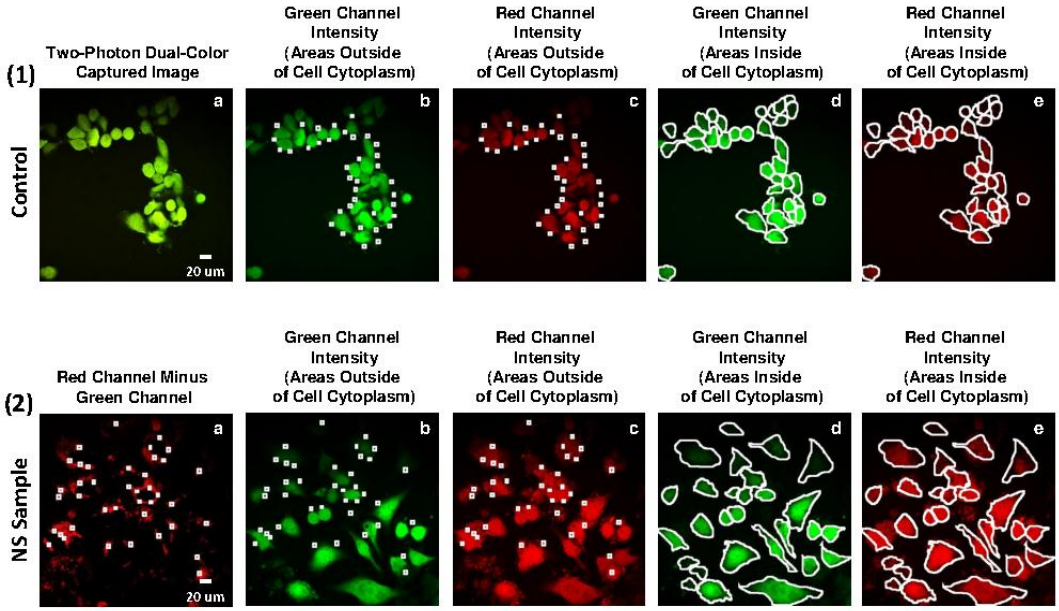

Figure 3.6: Luminescence Intensity Ratio Analysis of Nanoshell Cell Adhesion/Endocytosis from Figure 5. Panel 1: Green and red channel images of outlines of areas just outside (1b and 1c) or inside (1d and 1e) HeLa cells for a control sample. Panel 2: Corresponding image outlines for cells incubated with 200 nm Eu-TiO2-PEI NSs. All outlines were based on the location of the green cytoplasmic cell stain images and used to calculate the fluorescence ratios in Table 3.4.

The ratio analysis performed on the regions just outside of HeLa-only samples showed a red/green luminescence ratio value of 1.42 (SE ± 0.03), while the HeLa cell samples incubated with europium-doped TiO_2 NSs exhibited a ratio of 4.29 (± 0.15) (Table 3.4). Thus, the cells incubated with Eu-TiO_2 NSs had a photoluminescence intensity ~200% greater in areas just outside the cellular membrane than wild HeLa cells. This suggest that a large number of Eu^{3+}-doped hollow titania NSs attached to the outer surface of HeLa cells through electrostatic interactions. Moreover, when the ratio

analysis was performed on the interior areas of cells, the HeLa-only samples had a ratio value of 1.07 (± 0.02), whereas samples that saw Eu-TiO_2 NSs had a value of 1.56 (± 0.11). Therefore, cells that were incubated with NSs were 46% more luminescent, which is consistent with a small amount of Eu-TiO_2 NS being endocytosed by HeLa cells. These ratio analysis values are similar to those obtained for adhesion/endocytosis of Eu^{3+}-doped hollow silica NSs [57]. Emission from Eu^{3+} -doped hollow titania NSs is more intense than for the corresponding silica NSs because of the antenna effect of the UV absorbing titania.

Table 3.4: Luminescence Intensity Ratio Analysis for 200 nm PEI-Coated TiO_2 NSs Made Using 0.025% $Eu(NO_3)_3 \cdot 5H_2O$[1].

	Red Mean Luminescence / Green Mean Luminescence	Standard Error
Controls: Outside of Cell[2] (n = 118)	1.42	0.03
NS Samples: Outside of Cell (n = 93)	4.29	0.15
Controls: Inside of Cell[3] (n = 122)	1.07	0.02
NS Samples: Inside of Cell (n = 48)	1.56	0.11

[1]Note: Luminescence ratios inside and outside of cells for control samples are different because inner cell ratios were calculated in areas where the cell is stained (ratio most likely bleed through into red of green dye), while outer cell ratios were calculated in non-stained (i.e. black background) areas.

[2]Outside of Cell = red/green luminescence ratios calculated using small outline boxes surrounding a cell like those seen in Figure 3.6 (panels 1b,2b & 1d,2d)

[3]Inside of Cell = red/green luminescence ratios calculated using cytoplasmic cell outline like those seen in Figure 3.6 (panels 1c,2c & 1e,2e)

3.4 Conclusion

Uniform-sized Eu^{3+}-doped hollow titania NSs were fabricated by a new method using $Ti(O\text{-}t\text{-}Bu)_4$ and $Eu(NO_3)_3$ with amine-functionalized polystyrene beads serving as templates. Removal of the polystyrene core by calcining led to increased luminescence from Eu^{3+}-doped hollow nanoshells as the hydrated titania sol-gel partially transformed to the anatase-doped crystalline phase. Up to 1.1% Eu^{3+} could be introduced before the nanoshells lost their structural integrity, and the doped NS exhibited a strong narrow red photoluminescence emission at 617 nm upon UV excitation of the titania. Europium-doped hollow NSs were functionalized with PEI, which changed the NS surface charge from negative to positive. The positively charged doped NSs were shown by two-photon microscopy to bind to the outer surface of HeLa cervical cancer cells with minimal endocytosis. Since the Eu^{3+} luminescence does not photobleach, the UV absorbing titania acts as an antenna to enhance emission, and the luminescent state is also amenable to imaging by two-photon techniques. These NSs may be especially useful in the fields of biological imaging, diagnostics, and/or therapeutics.

3.5 Acknowledgements

This research was supported by NIH Nanotumor Grant (NIH Grant U54 CA 119335) and we thank the California Institute of Information Technology and Telecommunication and the Air Force Office of Scientific Research (AFOSR grant number FA9550-12-1-0381) for research support. In addition, individual student funding was provided by NIH Ruth L. Kirschstein National Research Service Award F31 Fellowship (NIH Grant No. 5F31 EB010375), NCI Research Supplements to Promote Diversity in Health Related Research Fellowship (NIH Grant No. 3U54 CA 119335–05S3), NSF—California LSAMP Bridge to the Doctorate/Louis Stokes Alliances for Minority Participation Fellowship (UCINSF Grant No. HRD0115115), and NIH—ET CURE/Specialized Cancer Center Support (Grant No. 3P30 CA 023100–25S7). The NIH National Center for Microscopy and Imaging Research at UCSD is acknowledged for assistance in obtaining the TEM images.

Chapter 3 contents are part of a manuscript in preparation, Sandoval S., Yang J., Alfaro J.G., Aschemeyer S., Liberman, A., Mikale M., Chiang C., Schuller I., Kummel A.C., Trogler W.C. The dissertation author was the primary researcher and author of this work.

3.6 References

1. Ma, L., et al., *Fabrication and properties of meso-macroporous electrodes screen-printed from mesoporous titania nanoparticles for dye-sensitized solar cells.* Mater Chem Phys, 2009. **118**(2-3): p. 477-483.

2. Vlachopoulos, N., et al., *Very efficient visible light energy harvesting and conversion by spectral sensitization of high surface area polycrystalline titanium dioxide films.* J Amer Chem Soc, 1988. **110**(4): p. 1216-1220.

3. Mohammadi, M.R., D.J. Fray, and M.C. Cordero-Cabrera, *Sensor performance of nanostructured TiO2 thin films derived from particulate sol-gel route and polymeric fugitive agents.* Sens Actuators B, 2007. **124**(1): p. 74-83.

4. Xu, J., et al., *Synthesis of Gd-doped TiO2 nanoparticles under mild condition and their photocatalytic activity.* Colloids Surf A, 2009. **334**(1-3): p. 107-111.

5. Herz, E., et al., *Fluorescent core-shell silica nanoparticles: an alternative radiative materials platform.* Proc. SPIE-Int. Soc. Opt. Eng., 2006. **6096**: p. 609605/1-609605/12.

6. Lee, S.-A., et al., *Use of Ultrafiltration Membranes for the Separation of TiO2 Photocatalysts in Drinking Water Treatment.* Indus Eng Chem Res, 2001. **40**(7): p. 1712-1719.

7. Park, Y., et al., *Organic dye-sensitized TiO2 for the redox conversion of water pollutants under visible light.* Chem Commun, 2010. **46**(14): p. 2477-2479.

8. Arabatzis, I.M. and P. Falaras, *Synthesis of Porous Nanocrystalline TiO2 Foam.* Nano Letters, 2002. **3**(2): p. 249-251.

9. Macak, J.M., et al., *TiO2 nanotubes: Self-organized electrochemical formation, properties and applications.* Curr Opin Solid State and Mater Sci, 2007. **11**(1-2): p. 3-18.

10. Cao, J., O. Rusina, and H. Sieber, *Processing of porous TiO2-ceramics from biological preforms.* Ceram Int, 2004. **30**(7): p. 1971-1974.

11. Necula, B.S., et al., *In vitro antibacterial activity of porous TiO2-Ag composite layers against methicillin-resistant Staphylococcus aureus.* Acta Biomaterialia, 2009. **5**(9): p. 3573-3580.

12. Tsuang, Y.-H., et al., *Studies of Photokilling of Bacteria Using Titanium Dioxide Nanoparticles.* Artificial Organs, 2008. **32**(2): p. 167-174.

13. Paunesku, T., et al., *Biology of TiO2-oligonucleotide nanocomposites.* Nat Mater, 2003. **2**(5): p. 343-346.

14. Wu, H.-P., T.-L. Cheng, and W.-L. Tseng, *Phosphate-Modified TiO2 Nanoparticles for Selective Detection of Dopamine, Levodopa, Adrenaline, and Catechol Based on Fluorescence Quenching.* Langmuir, 2007. **23**(14): p. 7880-7885.

15. Roy, S.C., M. Paulose, and C.A. Grimes, *The effect of TiO2 nanotubes in the enhancement of blood clotting for the control of hemorrhage.* Biomaterials, 2007. **28**(31): p. 4667-4672.

16. Zhu, R.R., et al., *Bio-effects of Nano-TiO2 on DNA and cellular ultrastructure with different polymorph and size.* Mater Sci Eng C, 2009. **29**(3): p. 691-696.

17. Lopez, T., et al., *Catalytic nanomedicine: A new field in antitumor treatment using supported platinum nanoparticles. In vitro DNA degradation and in vivo tests with C6 animal model on Wistar rats.* Eur J Med Chem, 2010. **45**(5): p. 1982-1990.

18. Kubota, Y., et al., *Photokilling of T-24 Human Bladder-Cancer Cells with Titanium-Dioxide.* British Journal of Cancer, 1994. **70**(6): p. 1107-1111.

19. Kalbacova, M., et al., *TiO(2) nanotubes: photocatalyst for cancer cell killing.* Phys Stat Solidi - Rapid Res Lett, 2008. **2**(4): p. 194-196.

20. Trouiller, B., et al., *Titanium Dioxide Nanoparticles Induce DNA Damage and Genetic Instability In vivo in Mice.* Cancer Res, 2009. **69**(22): p. 8784-8789.

21. Chen, W. and J. Zhang, *Using Nanoparticles to Enable Simultaneous Radiation and Photodynamic Therapies for Cancer Treatment.* J Nanosci Nanaotechnol, 2006. **6**: p. 1159-1166.

22. Rozhkova, E.A., et al., *A High-Performance Nanobio Photocatalyst for Targeted Brain Cancer Therapy.* Nano Letters, 2009. **9**(9): p. 3337-3342.

23. Abdulla-Al-Mamun, M., et al., *Enhanced Photocatalytic Cytotoxic Activity of Au@TiO2 Nanopellets against Human Epithelial Carcinoma (HeLa) Cells.* Chem Lett, 2009. **38**(10): p. 950-951.

24. Abdulla-Al-Mamun, M., Y. Kusumoto, and M.S. Islam, *Cytotoxic Evaluation of Ag@TiO2 Core-Shell Composite Nanoclusters against Cancer Cells.* Chem Lett, 2009. **38**(10): p. 980-981.

25. Abdulla-Al-Mamun, M. and Y. Kusumoto, *New Simple Synthesis of Cu-TiO2 Nanocomposite: Highly Enhanced Photocatalytic Killing of Epithelia Carcinoma (HeLa) Cells.* Chem Lett, 2009. **38**(8): p. 826-827.

26. Lopez, T., et al., *Pt/TiO2 brain biocompatible nanoparticles: GBM treatment using the C6 model in Wistar rats.* Acta Biomaterialia, 2008. **4**(6): p. 2037-2044.

27. Xu, J., et al., *Photokilling cancer cells using highly cell-specific antibody-TiO2 bioconjugates and electroporation.* Bioelectrochemistry, 2007. **71**(2): p. 217-222.

28. Caruso, R.A., A. Susha, and F. Caruso, *Multilayered Titania, Silica, and Laponite Nanoparticle Coatings on Polystyrene Colloidal Templates and Resulting Inorganic Hollow Spheres.* Chem Mater, 2001. **13**(2): p. 400-409.

29. Meyer, U., et al., *Templating of Porous Polymeric Beads to Form Porous Silica and Titania Spheres.* Adv Mater, 2002. **14**(23): p. 1768-1772.

30. Zhong, Z., et al., *Preparation of Mesoscale Hollow Spheres of TiO2 and SnO2 by Templating Against Crystalline Arrays of Polystyrene Beads.* Adv Mater, 2000. **12**(3): p. 206-209.

31. Lei, Z., et al., *Two-step Templating Route to Macroporous or Hollow Sphere Oxides.* J Mater Chem, 2001. **11**: p. 2930-2933.

32. Kim, T.H., K.H. Lee, and Y.K. Kwon, *Monodisperse hollow titania nanospheres prepared using a cationic colloidal template.* J Colloid Interfac Sci, 2006. **304**(2): p. 370-377.

33. Sun, X., J. Liu, and Y. Li, *Use of Carbonaceous Polysaccharide Microspheres as Templates for Fabricating Metal Oxide Hollow Spheres.* Chemistry - A European Journal, 2006. **12**(7): p. 2039-2047.

34. Wang, D., et al., *Preparation and characterization of TiO_2 hollow spheres.* Materials Letters, 2006. **60**(1): p. 77-80.

35. Yang, Z., et al., *Templated Synthesis of Inorganic Hollow Spheres with a Tunable Cavity Size onto Coreâ€“Shell Gel Particles.* Angew Chem Int Ed, 2003. **42**(17): p. 1943-1945.

36. Blešić, M.D., et al., *TiO2 films prepared by ultrasonic spray pyrolysis of nanosize precursor.* Mater Lett, 2002. **54**(4): p. 298-302.

37. Karan, N.S., et al., *Diffusion flame synthesis of hollow, anatase TiO2 nanoparticles.* Mater Sci Eng B, 2009. **163**(2): p. 128-133.

38. Zhang, C., et al., *Preparation of silica and titanium-containing silica hollow spheres at supercritical CO2/H2O interface.* J Supercrit Fluid, 2007. **42**(1): p. 142-149.

39. Wu, C.-I., et al., *Preparation of TiO2 nanoparticles by supercritical carbon dioxide.* Mater Lett, 2008. **62**(12–13): p. 1923-1926.

40. Bouzigues, C., T. Gacoin, and A. Alexandrou, *Biological Applications of Rare-Earth Based Nanoparticles.* ACS Nano, 2011. **5**(11): p. 8488-8505.

41. Lo, W.S., et al., *Impressive Europium Red Emission Induced by Two-Photon Excitation for Biological Applications.* Inorganic Chemistry, 2011. **50**(12): p. 5309-5311.

42. Conde-Gallardo, A., et al., *Photoluminescence properties of the Eu[3+] activator ion in the TiO2 host matrix.* Appl Phys Lett, 2001. **78**(22): p. 3436-3436.

43. Li, J.-G., et al., *Phase Structure and Luminescence Properties of Eu3+-Doped TiO2 Nanocrystals Synthesized by Ar/O2 Radio Frequency Thermal Plasma Oxidation of Liquid Precursor Mists.* J Phys Chem B, 2006. **110**(3): p. 1121-1127.

44. Yin, J.B., L.Q. Xiang, and X.P. Zhao, *Monodisperse spherical mesoporous Eu-doped TiO2 phosphor particles and the luminescence properties.* Appl Phys Lett, 2007. **90**(11): p. -.

45. Ghosh, P. and A. Patra, *Influence of Surface Coating on Physical Properties of TiO2/Eu3+ Nanocrystals.* J Phys Chem C, 2007. **111**(19): p. 7004-7010.

46. Julian, B., et al., *One-pot synthesis and optical properties of $Eu^{[3+]}$ -doped nanocrystalline TiO_2 and ZrO_2.* Nanotechnology, 2005. **16**(11): p. 2707-2713.

47. Luo, M., et al., *Enhanced Luminescence of Eu-Doped TiO2 Nanodots.* Nanoscale Res Lett, 2009. **4**(8): p. 809-813.

48. Aihua, P., et al., *Photoluminescence properties of TiO2: Eu3 + thin films deposited on different substrates.* Mater Lett, 2005. **59**(29-30): p. 3866-3869.

49. Tan, M., et al., *Synthesis and characterization of titania-based monodisperse fluorescent europium nanoparticles for biolabeling.* J Lumin, 2006. **117**(1): p. 20-28.

50. Xie, Y. and C. Yuan, *Transparent TiO2 sol nanocrystallites mediated homogeneous-like photocatalytic reaction and hydrosol recycling process.* J Mater Sci, 2005. **40**(24): p. 6375-6383.

51. Xu, Z., et al., *Structure, luminescence properties and photocatalytic activity of europium doped-TiO2 nanoparticles.* J Mater Sci, 2005. **40**(6): p. 1539-1541.

52. Yi, S.-s., et al., *Highly enhanced luminescence of nanocrystalline TiO2:Eu3+ phosphors.* Opt Mater, 2006. **28**(6-7): p. 610-614.

53. Zeng, Q.G., Z.J. Ding, and Z.M. Zhang, *Synthesis, structure and optical properties of Eu3+/TiO2 nanocrystals at room temperature.* J Lumin, 2006. **118**(2): p. 301-307.

54. Zhao, Z., et al., *Optical properties of Eu3+-doped TiO2 nanocrystalline under high pressure.* J Lumin, 2006. **122-123**: p. 862-865.

55. Andelman, T., et al., *Synthesis and Cytotoxicity of Y2O3 Nanoparticles of Various Morphologies.* Nano Res Lett, 2010. **5**(2): p. 263-273.

56. Epling, G.A. and C. Lin, *Photoassisted bleaching of dyes utilizing TiO_2 and visible light.* Chemosphere, 2002. **46**(4): p. 561-570.

57. Yang, J., et al., *Red-luminescent europium (III) doped silica nanoshells: synthesis, characterization, and their interaction with HeLa cells.* Journal of Biomedical Optics, 2011. **16**(6).

58. Gash, A.E., et al., *New sol-gel synthetic route to transition and main-group metal oxide aerogels using inorganic salt precursors.* Journal of Non-Crystalline Solids, 2001. **285**(1-3): p. 22-28.

59. Klimchuk, O., et al., *New Wide Rim Phosphomethylated Calix[4]arenes in Extraction of Americium and Europium.* Journal of Inclusion Phenomena and Macrocyclic Chemistry, 2004. **49**(1): p. 47-56.

60. Tong, T., et al., *Preparation of Fe3+-doped TiO2 catalysts by controlled hydrolysis of titanium alkoxide and study on their photocatalytic activity for methyl orange degradation.* Journal of Hazardous Materials, 2008. **155**(3): p. 572-579.

61. Yang, J., J.U. Lind, and W.C. Trogler, *Synthesis of Hollow Silica and Titania Nanospheres.* Chemistry of Materials, 2008. **20**(9): p. 2875-2877.

62. Brinker, C.J. and G.W. Scherer, *Sol-gel science : the physics and chemistry of sol-gel processing*. 1990, Boston: Academic Press. xiv, 908.

63. Suvarna, S., et al., *Determinants of PF4/heparin immunogenicity.* Blood, 2007. **110**(13): p. 4253-4260.

64. *Zeta Potential of Colloids in Water and Waste Water*. 1985: American Society for Testing and Materials (ASTM) Standard D 4187-8.

65. Bazylińska, U., P. Warszyński, and K.A. Wilk, *Influence of pH upon in vitro sustained dye-release from oil-core nanocapsules with multilayer shells.* Colloids and Surfaces A: Physicochemical and Engineering Aspects, 2012(0).

66. Thünemann, A., et al., *Polyelectrolyte Complexes,* in *Polyelectrolytes with Defined Molecular Architecture II,* M. Schmidt, Editor. 2004, Springer Berlin Heidelberg. p. 113-171.

67. Werts, M.H.V., *Making sense of lanthanide luminescence.* Science Progress, 2005. **88**: p. 101-131.

68. Jeon, S. and P.V. Braun, *Hydrothermal Synthesis of Er-Doped Luminescent TiO2 Nanoparticles.* Chemistry of Materials, 2003. **15**(6): p. 1256-1263.

69. Xu, Z., et al., *Structure, luminescence properties and photocatalytic activity of europium doped-TiO2 nanoparticles.* Journal of Materials Science, 2005. **40**(6): p. 1539-1541.

70. Feng, X., et al., *A facile one-pot hydrothermal method to prepare europium-doped titania hollow phosphors and their sensitized luminescence properties.* Journal of Alloys and Compounds, 2010. **506**(2): p. 728-733.

71. Ding, S., et al., *Mesoporous hollow TiO2 microspheres with enhanced photoluminescence prepared by a smart amino acid template.* Journal of Materials Chemistry, 2011. **21**(13): p. 4888-4892.

72. Yin, J.B., L.Q. Xiang, and X.P. Zhao, *Monodisperse spherical mesoporous Eu-doped TiO2 phosphor particles and the luminescence properties.* Applied Physics Letters, 2007. **90**(11): p. -.

73. Pal, M., et al., *Effects of crystallization and dopant concentration on the emission behavior of TiO2: Eu nanophosphors.* Nanoscale Research Letters, 2012. **7**.

74. Ningthoujam, R.S., et al., *Photoluminescence studies on Eu doped TiO2 nanoparticles.* Journal of Alloys and Compounds, 2009. **486**(1–2): p. 864-870.

75. Kim, H.M., et al., *Design of molecular two-photon probes for in vivo imaging. 2H-Benzo[h]chromene-2-one derivatives.* Tetrahedron Letters, 2007. **48**(15): p. 2791-2795.

76. Sumalekshmy, S. and C.J. Fahrni, *Metal-Ion-Responsive Fluorescent Probes for Two-Photon Excitation Microscopy†.* Chemistry of Materials, 2010. **23**(3): p. 483-500.

77. Eliseeva, S.V. and J.-C.G. Bunzli, *Lanthanide luminescence for functional materials and bio-sciences.* Chemical Society Reviews, 2010. **39**(1): p. 189-227.

78. Yacobi, N.R., et al., *Mechanisms of Alveolar Epithelial Translocation of a Defined Population of Nanoparticles.* American Journal of Respiratory Cell and Molecular Biology, 2010. **42**(5): p. 604-614.

79. Finkelstein, E.I., et al., *Electric field-induced polarization of charged cell surface proteins does not determine the direction of galvanotaxis.* Cell Motility and the Cytoskeleton, 2007. **64**(11): p. 833-846.

80. Cohen, C.M., et al., *Membrane Isolation on Polylysine-Coated Beads - Plasma-Membrane from Hela-Cells.* Journal of Cell Biology, 1977. **75**(1): p. 119-134.

81. Kalish, D.I., et al., *Membrane Isolation on Polylysine-Coated Glass Beads - Asymmetry of Bound Membrane.* Biochimica Et Biophysica Acta, 1978. **506**(1): p. 97-110.

82. Schroeder, A., et al., *Lipid-based nanotherapeutics for siRNA delivery.* J Intern Med, 2010 **267**(1): p. 9-21.

83. Daniels, D.S. and A. Schepartz, *Intrinsically cell-permeable miniature proteins based on a minimal cationic PPII motif.* J Am Chem Soc, 2007. **129**(47): p. 14578-9.

84. Frankel, A.D. and C.O. Pabo, *Cellular uptake of the tat protein from human immunodeficiency virus.* Cell, 1988. **55**(6): p. 1189-93.

85. Hong, S., et al., *Interaction of poly(amidoamine) dendrimers with supported lipid bilayers and cells: hole formation and the relation to transport.* Bioconjug Chem, 2004. **15**(4): p. 774-82.

86. Karmali, P.P. and A. Chaudhuri, *Cationic liposomes as non-viral carriers of gene medicines: Resolved issues, open questions, and future promises.* Medicinal Research Reviews, 2007. **27**(5): p. 696-722.

87. Huang, X., et al., *The effect of the shape of mesoporous silica nanoparticles on cellular uptake and cell function.* Biomaterials, 2010. **31**(3): p. 438-448.

88. Huang, M., et al., *Uptake of FITC-Chitosan Nanoparticles by A549 Cells.* Pharm Res, 2002. **19**(10): p. 1488-1494.

89. Gupta, A.K. and A.S.G. Curtis, *Lactoferrin and ceruloplasmin derivatized superparamagnetic iron oxide nanoparticles for targeting cell surface receptors.* Biomaterials, 2004. **25**(15): p. 3029-3040.

90. Cai, Y., et al., *Role of hydroxyapatite nanoparticle size in bone cell proliferation.* J Mater Chem, 2007. **17**(36): p. 3780-3787.

91. Mansouri, S., et al., *Characterization of folate-chitosan-DNA nanoparticles for gene therapy.* Biomaterials, 2006. **27**(9): p. 2060-2065.

92. de Salamanca, A.E., et al., *Chitosan Nanoparticles as a Potential Drug Delivery System for the Ocular Surface: Toxicity, Uptake Mechanism and In Vivo Tolerance.* Invest Ophth Vis Sci, 2006. **47**(4): p. 1416-1425.

93. Cartiera, M.S., et al., *The uptake and intracellular fate of PLGA nanoparticles in epithelial cells.* Biomaterials, 2009. **30**(14): p. 2790-2798.

94. Thurn, K., et al., *Nanoparticles for Applications in Cellular Imaging.* Nanoscale Res Lett, 2007. **2**(9): p. 430-441.

95. Slowing, I.I., et al., *Mesoporous silica nanoparticles as controlled release drug delivery and gene transfection carriers.* Adv Drug Deliv Rev, 2008. **60**(11): p. 1278-1288.

96. Desai, M.P., et al., *The mechanism of uptake of biodegradable microparticles in Caco-2 cells is size dependent.* Pharm Res, 1997. **14**(11): p. 1568-73.

97. Chithrani, B.D., A.A. Ghazani, and W.C.W. Chan, *Determining the Size and Shape Dependence of Gold Nanoparticle Uptake into Mammalian Cells.* Nano Letters, 2006. **6**(4): p. 662-668.

98. Prabha, S., et al., *Size-dependency of nanoparticle-mediated gene transfection: studies with fractionated nanoparticles.* Int J Pharm, 2002. **244**(1-2): p. 105-15.

99. Zhang, S., et al., *Size-Dependent Endocytosis of Nanoparticles.* Adv Mater, 2009. **21**(4): p. 419-424.

100. Jiang, W., et al., *Nanoparticle-mediated cellular response is size-dependent.* Nat Nano, 2008. **3**(3): p. 145-150.

101. Verma, A. and F. Stellacci, *Effect of Surface Properties on Nanoparticle–Cell Interactions.* Small, 2010. **6**(1): p. 12-21.

102. Muro, S., et al., *Control of Endothelial Targeting and Intracellular Delivery of Therapeutic Enzymes by Modulating the Size and Shape of ICAM-1-targeted Carriers.* Mol Ther, 2008. **16**(8): p. 1450-1458.

103. Perry, J.L., et al., *PRINT: A Novel Platform Toward Shape and Size Specific Nanoparticle Theranostics.* Accounts Chem Res, 2011. **44**(10): p. 990-998.

104. Tkachenko, A.G., et al., *Multifunctional Gold Nanoparticle−Peptide Complexes for Nuclear Targeting.* J Amer Chem Soc, 2003. **125**(16): p. 4700-4701.

105. Byrne, J.D., T. Betancourt, and L. Brannon-Peppas, *Active targeting schemes for nanoparticle systems in cancer therapeutics.* Adv Drug Del Rev, 2008. **60**(15): p. 1615-1626.

106. Davis, M.E., *The First Targeted Delivery of siRNA in Humans via a Self-Assembling, Cyclodextrin Polymer-Based Nanoparticle: From Concept to Clinic.* Molec Pharm, 2009. **6**(3): p. 659-668.

107. Berry, C.C., *Possible exploitation of magnetic nanoparticle-cell interaction for biomedical applications.* J Mater Chem, 2005. **15**(5): p. 543-547.

108. Rosenholm, J.M., et al., *Targeting of Porous Hybrid Silica Nanoparticles to Cancer Cells.* ACS Nano, 2008. **3**(1): p. 197-206.

Chapter 4. Targeting of Cervical Cancer Cells using Folate Functionalized SiO_2 Hollow Nanoshells

A simple method to functionalize hollow SiO_2 nanoshell (NS) particles with fluorescent reporter FITC and folate using NHS conjugation techniques is reported. Folate was used as a cancer targeting ligand as it is essential for the synthesis of nucleotide bases and binds with high affinity to folate receptors, which are frequently over-expressed in tumor cells such as ovarian carcinomas. Functionalized NS were characterized using SEM and DLS analysis and maximum amount of folate functionalized on NS surfaces was calculated with the use of UV-Vis spectroscopy. Nanoshell interactions with HeLa cervical cancer cells in vitro were visualized using fluorescent and confocal microscopy and studied using a fluorescent ratio analysis to assess nanoshell adhesion and endocytosis while comparing folate targeting NS versus non-targeting PEG functionalized NS. It was found that as the amount of folate on the surface of the NS was increased, a higher amount of NS adhered and endocytose into HeLa cancer cells at larger rates than similar size non-targeting PEG functionalized NS.

4.1 Introduction

Currently diverse nanoparticle based technologies are being developed for biomedical applications. These nanoparticles are typically synthesized using polymeric [1-4], liposomal [5-8], or inorganic formulations [9-12]. Medical areas of study that nanoparticles are being developed for include therapeutic delivery systems [1-4], ablative therapy sensitizers [13-15], and biomedical imaging [16-18]. Two highly critical parameters which influence nanoparticle efficacy are *in vivo* circulation time and cellular accumulation or adhesion. The longer a particle can survive and circulate *in vivo*, the higher probability it can accumulate at a desired target or provide other

capabilities. Similarly, cellular accumulation or adhesion is critical for therapeutic delivery.

Many cancer therapeutics are hydrophobic, have poor bioavailability, and poor *in vivo* stability. As a result, these drugs are packaged with a variety of surfactants and other products, such as Cremophor EL, which can have adverse side effects [19]. In the case of other therapeutics currently in development, such as siRNA, or various catalytic enzymes and other nucleic acid based therapies, the *in vivo* half-life (minutes to 2 hours for unmodified siRNA varying by report) is too short to be an effective therapy without a delivery vehicle [20]. In both of these cases, encapsulation within a nanoparticle can aid in intracellular delivery. For instance, targeted particles could be utilized to locally raise the drug concentration rather than subjecting the entire body to the adverse effects of chemotherapeutics. This can potentially allow for lower drug dosing while also resulting in a more effective therapeutic.

A variety of methods have been studied to synthesize targeted nanoparticles. Folate targeting, for instance, has been investigated to specifically target and deliver nanoparticles to various types of cancers [21-24]. Folate, also called folic acid or Vitamin B_9, is required by cells for the biosynthesis of nucleotides [25, 26], a process necessary in DNA replication; it is the DNA replication process that becomes uninhibited in many cancers, causing unregulated cell growth and proliferation [27]. There are multiple factors which make folate an ideal candidate for use as a cancer targeting ligand: (a) the overexpression of folate receptor α (FR) found on a wide variety of human cancers including ovarian, breast, and colorectal cancers [28-38], (b) FRs high binding affinity for folic acid ($K_d \approx 0.1$ nM) [39], and (c) the low risk of folate targeted nanoparticles interacting with normal tissue due to those few FRs that are expressed in normal cells being highly inaccessible due to their location on the apical (i.e. lumen facing) surface of polarized epithelia [40-42]. Therefore, the overexpression of the folate receptor suggests that it may be possible to concentrate a toxic dose at the cancerous tissues while sparing the normal tissue from exposure to potent chemotherapeutics [38].

Previous studies have shown that surface functionalization of nanoparticles with folate increases uptake of nanoparticles by cancer cells [43-47]. For example, Rosenholm *et al*. showed that the addition of folic acid to the surface of mesoporous silica nanoparticles, which were also functionalized with fluorescent reporter FITC, increased the number of HeLa cells which uptake particles from 24% to 52% within 24 hours [43]. Werner *et al*. showed mice treated with folate targeted PLGA nanoparticles loaded with paclitaxel and a radio-sensitizer, had significantly longer survival rates compared to those treated with non-targeted nanoparticles [46].

A wide variety of techniques have been previously employed in quantifying cellular uptake and/or surface adhesion of nanoparticles. These techniques primarily involve quantification through fluorescence, mass, or atomic spectroscopy [48-55]. Inductively coupled plasma-atomic emission spectroscopy **(**ICP-AES) has been used to calculate the uptake of gold particles into HeLa cells as a function of size, concentration, aspect ratio, and incubation time [49], as well as to quantify the uptake of superparamagnetic, folate/polyethylene glycol (PEG) functionalized magnetite particles in BT20 human breast cancer cells and in RAW 264.7 mouse macrophage cells [50]. The latter study found that functionalizing the surface of the particles with folate and PEG reduced protein adsorption and facilitated the uptake of particles. Although, methods such as fluorescence, mass, and atomic spectroscopy can be used to quantify the amount of nanoparticles present in cells [55], they cannot distinguish between internalized particles and those only adhered to the cell surface. Instead, multiple methods must be used to quantify nanoparticle uptake. For example in the study by Yin *et al.*, the efficiency of targeted PLGA particle uptake in Caco-2 in human colon adenocarcinoma cells were examined by detecting fluorescent markers with a fluorescence micro-plate reader, after performing multiple and rigorous washing steps and lysing the plated cells. Subsequently, the data had to be confirmed qualitatively with CLSM, Cryo-SEM, and TEM in order to confirm if the nanoparticles were actually internalized within cells [53] and not just adhered to the cell surface. The goal of this article is to describe a novel fluorescent ratio analysis method performed exclusively on fluorescence and confocal microscopy images in order to quantify nanoparticle cell

adhesion and intracellular uptake, plus cancer cell selectivity, of fluorescently labeled, folate functionalized hollow silica nanoshells, while also demonstrating the advantage of folate targeting in increased nanoparticle cellular uptake compared to non-targeted silica nanoshells.

4.2 Experimental Methods

4.2.1 Materials

Tetramethyl orthosilicate (TMOS), (3-aminopropyl)- triethoxysilane (APTES), *N*-hydroxysuccinimide (NHS), *N*-(3-dimethylaminopropyl)-*N′*-ethylcarbodiimide hydrochloride (EDAC), dimethyl sulfoxide (DMSO), and folic acid were obtained from Sigma-Aldrich (St. Louis, MO). Monomethoxypoly(ethylene glycol)-carboxymethyl (mPEG-CM, 2,000 MW) was purchased from Laysan Bio (Arab, Alabama). The 100 nm amine functionalized polystyrene (APS) beads (2.5% w/w) were purchased from PolySciences Ltd (Warrington, PA). HeLa cervical cancer cells and human foreskin fibroblast (HFF-1) were purchased from ATCC (Manassas, Virginia); Dulbecco's Phosphate Buffer Saline solution (DPBS 1×) and fetal bovine serum (FBS) were purchased from Mediatech, Inc. (Manassas, Virginia). RPMI 1640 folate free medium, media supplements, Hoechst 33342, Wheat Germ Agglutinin (WGA) – Alexa Fluor 594 Conjugate, Fluorescein (FITC) Isothiocynate, Prolong Gold, and CellTracker CMFDA Green, CellTracker CMAC Blue, CellTracker CMPTX Red intracellular stains were obtained from Life Sciences Corporation (Carlsbad, California). Nunc Lab-Tek II 4-well chamber slides and Paraformaldehyde (PFA) were purchased from ThermoFisher Scientific (Fair Lawn, New Jersey). All chemicals and reagents were used as received or as described by in manufacture protocols, unless otherwise stated.

4.2.2 Preparation of Hollow Silica Nanoshells

Silica nanoshells were prepared using a previously reported method [10, 56, 57]. Briefly, this was accomplished by taking 100 uL of a 2.5% weight dispersion (in water) of 100 nm APS beads and suspending them in 1.75 mL of absolute ethanol. To this suspension, 6.5 uL of TMOS was added. The mixture was stirred on a vortex mixer at

room temperature at a speed of 900 rpm. After 12 h of stirring, a white precipitate was collected by centrifugation and washed with ethanol and dried in vacuum for 48 h at room temperature to give 4.1 mg of core-shell spheres.

The APS core was removed by calcining the 4.1 mg of core-shell nanospheres by heating in air at 5ºC per minute to 500ºC and maintaining this temperature for 24 h. About 1.5 mg of hollow SiO_2 nanoshells (NS) were collected as a white powder.

4.2.3 Preparation of NHS-Folate and NHS-mPEG

Active intermediate N-hydroxysuccinimide-folate (NHS-folate) was synthesized by adding 0.94 mg of NHS, 1.57 mg of EDAC, 3 mg of folic acid, and 1 mL of DMSO in a 2 mL eppendorf tube. This mixture was vortexed at 3000 rpm for 24 hrs and used within 24 hrs to functionalized NS surfaces with folate. Similarly, N-hydroxysuccinimide-mPEG (NHS-mPEG) was created by weighing out 0.94 mg of NHS, 1.57 mg of EDAC, 13.6 mg of mPEG (molar equivalent to 3 mg of folic acid) in an eppendorf tube. Contents were suspended in 1 mL of DMSO, and the mixture was vortexed at 3000 rpm for 24 hrs. The final solution was used within 24 hrs to create non-targeted PEG functionalized NS.

4.2.4 Amine Surface Functionalization of SiO_2 Hollow Nanoshells with APTES

Before functionalizing NS surfaces with FITC, NHS-folate, and/or NHS-mPEG, NS had to be first amine functionalized. This was accomplished by suspending 3 mg of particles in a solution composed of 1 mL of ethanol and 0.3 μL of APTES in a 2 mL eppendorf tube. The suspension was stirred 2 hours and the NS were collected by centrifugation, washed twice with ethanol, and resuspended in 1 mL DMSO.

4.2.5 Surface Modification of SiO_2 Hollow Nanoshells with FITC-Isothiocynate and NHS-Folate or NHS-mPEG

In a 2 mL eppendorf tube containing 3 mg of amine functionalized NS suspended in 1 mL of DMSO, 2 μL of 10 mg/mL solution of FITC in DMSO was added

to the particles in parallel with a variable amount of a NHS-folate or NHS-PEG solution in DMSO. The variable amounts of NHS-folate solution contained either 2, 20, or 200 ug of NHS-folate, while variable amounts of NHS-PEG solution contained 9, 90, or 900 ug of NHS-PEG. These NS solutions were vortexed for 24 hours at 3000 rpm. After vortexing, the particles are washed twice with DMSO and then resuspended in 1 mL of PBS for use in cell experiments.

4.2.6 Characterization of Functionalized SiO_2 Hollow Nanoshells

Scanning electron microscopy (SEM) analysis of NS was conducted on a FEI/Philips XL30 FEG ESEM microscope with an accelerating voltage of 10 kV. A Zetasizer Nano ZS (Malvern Instruments) was used to measure the dynamic light scattering (DLS) size distribution, polydispersity index (PDI), and zeta potential of NS when suspended in distilled water after 3 hrs of alternating 15 min periods of gentle sonication and vortexing.

Quantification of maximum amount of folate on NS surfaces was performed on NS functionalized only with NHS-folate. During particle functionalization, supernatants from the wash steps were collected and analyzed by UV-Vis spectrophotometry (Perkin Elmer Lambda Scan 35). To calculate the amount of folate retained by the particles, the absorbance was converted into a concentration and multiplied by the volume of the washes resulting in a known mass of folate which was not conjugated onto the particle. This mass was subtracted from the known starting mass of the folate added to the particles during the synthesis reaction to calculate the amount of folate on the surface of the total particles. Using a previously reported weight factor equation method [57], an estimate of the number of NS used in the synthesis reaction was calculated along with amount of folate actually present on the surface of the total particles, to determine the average value of folate molecules per NS.

4.2.7 Cell Culture – HeLa Cell Only Samples

HeLa cervical cancer cells were grown at 5×10^4 cells/well on Nunc Lab-Tek II 4-well chamber slides in RPMI 1640 folate free medium supplemented with 10% FBS

and 1% antibiotics (penicillin, streptomycin, glutamine (PSG)) at 37 °C in a humidified atmosphere of 5% CO_2. Before starting cell adhesion/endocytosing experiments, the cells were grown to 60 to 80% well confluency.

4.2.8 Cell Culture – Nanoshell Selectivity Experiments

Using 15 mL falcon tubes, HeLa and HFF-1 cells were individually stained in a 2 mL RPMI 1640 folate-free complete media suspension following manufacturer guidelines. Briefly, HeLa cells were stained with a final concentration of 5μM CMPTX CellTracker Red intracellular stain, while HFF-1 cells were stained with 20μM CMAC CellTracker Blue, for 30min while under gentle agitation using a Barnstead/Thermolyne Labquake rotisserie in order to prevent cells from adhering to falcon tubes. Cells were washed twice to remove any excess dye and then resuspended in RPMI 1640 folate free complete media. Since normal cells tend to grow at a slower pace than cancer cells, HFF-1 were mixed with HeLa cells at a 3:2 ratio before being plated on Nunc Lab-Tek II 4-well chamber slides in RPMI folate free complete media. Samples were incubated at 37 °C in a humidified atmosphere of 5% CO_2 for 24 hrs to allow the cells to adhere to slide surfaces.

4.2.9 Cell Adhesion/Endocytosis Experiments

In order to determine the extent of NS cell adhesion/endocytosis, HeLa cell only samples were incubated with 100 μg/mL of FITC/folate or FITC/PEG functionalized SiO_2 NS for 24 hrs in RPMI folate free complete media at 37 °C in a humidified atmosphere of 5% CO_2. Afterwards, cells were washed twice with DPBS and labeled with 5 μg/mL WGA membrane stain and 0.01 μg/mL Hoechst nucleus dye in DPBS for 30 min. Subsequently, cells were washed 3x with DPBS to remove any excess dye, fixed with 4% PFA in DPBS solution, washed twice more with DPBS, and covered with Prolong Gold antifade reagent in order to prepare samples for visualization by fluorescent and/or confocal microscopy.

This protocol was adapted for the NS selectivity experiments, with the notable exemption of the staining step, as cells were pre-stained before cell plating in order to distinguish cell types, and incubating NS concentrations were reduced to 50 μg/mL.

4.2.10 Fluorescence Microscopy of Nanoshell Cell Adhesion

Fluorescence microscopy was used to visualize the adhesion of FITC/folate or FITC/PEG functionalized SiO_2 nanoshells in adhesion/selectivity experiments. Three individual fluorescent images (blue, red, and green channels) were captured using a Zeiss AxioImager Z1 (Carl Zeiss Inc., Thornwood, NY) fluorescence microscope and a 1.4 mega-pixel Photometrics Cool-SNAP HQ^2 camera with the appropriate color filter. The samples were imaged at 40x magnification and had an image resolution of 0.1566 μm/pixel. The green fluorescence was visualized using a Zeiss 38HE filter set. Zeiss filter sets 49 and 32 were used to visualize the blue and red fluorescence, respectively. The resulting images were compiled and processed using ImageJ (NIH, Bethesda, MD). The excitation source was a short arc mercury lamp.

4.2.11 Confocal Microscopy of Nanoshell Uptake by HeLa Cells

Confocal microscopy was employed to visualize the uptake of FITC/folate or FITC/PEG functionalized SiO_2 nanoshells by HeLa cervical cancer cells. Z-stack images were captured using a Zeiss LSM510 laser scanning microscope using a Plan-Apochromat 100x 1.4 NA oil objective lens. Sequential 90 um x 90 um (frame size 1024 x 1024) sections were acquired at 0.7 micron intervals in the z direction with excitation wavelengths of 364, 488, & 543 nm.

4.3 Results/Discussion

4.3.1 Characterization of Functionalized SiO_2 Hollow Nanoshell

As shown in Figure 4.1, hollow silica NS were functionalized with 20 ug of FITC and either varying amounts of NHS-folate or NHS-mPEG. Folate was used as a targeting ligand because FR type α are frequently over-expressed in tumor cells and

epithelial lineaged tumors. PEG was functionalized on the NS surface, at the same molar ratio as folate to NS, in order to have non-targeted, similar size, NS controls.

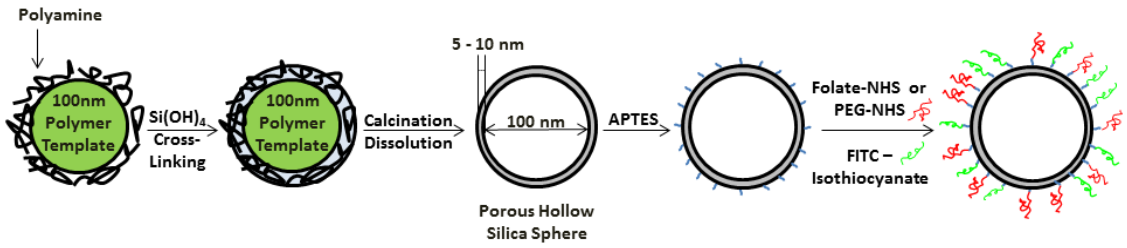

Figure 4.1: Schematic of Nanoshell (NS) Synthesis and Functionalization. Folate was used as a targeting ligand because folate receptor (FR) type α is frequently over-expressed in certain tumor cells and epithelial lineage tumors. Polyethylene glycol (PEG) was functionalized on the NS surface, at the same molar ratio as folate to NS, in order to have non-targeted, similar size, NS controls.

Using DLS, the dispersed size of plain and functionalized SiO_2 nanoshells in aqueous suspension were estimated. All the concentrations of nanoshells in aqueous suspension were 3 mg/mL. After 3 h of alternating 15 min periods of gentle sonication and vortexing, 10 uL of suspension was diluted in 1 mL of D.I. water for size and zeta potential determinations. Table 4.1 shows a summary of the sizes, PDI, and zeta potentials of non-functionalized and varying FITC, folate, and/or PEG functionalized NS. The results suggest that NS functionalized with only hydrophobic FITC fluorophore tend to cluster together, but as folate or PEG concentration are increased during the synthesis reaction process; particles aggregate less and become more monodispersed. This can be seen in the reduction of the hydrodynamic diameter and shrinkage of the PDI values as the folate or PEG concentration is increased. Furthermore, the DLS results show that by functionalizing particles with the same molar ratio of folate or PEG to NS, it was possible to create targeted and non-targeted particles of similar hydrodynamic diameter. For example, the DLS measurements show that in aqueous suspensions NS functionalized with 20ug FITC & 200ug folate had an average hydrodynamic diameter of 330nm (PDI: 0.35), while NS functionalized with 20ug FITC & 900ug PEG had a similar hydrodynamic diameter of 300 nm (PDI: 0.41).

These results also indicate that at the highest tested amounts of folate and PEG functionalized onto the NS surfaces are disperse largely as trimers or quatramers in solution; however, the nonideal (by DLS standards) optical properties of these nanoparticles may distort the measurements. In addition, since the PDI represents the relative variance in the particle size distribution, and the PDI scale ranges from 0 to 1, with 0 being monodisperse and 1 being polydisperse [58-60], the results indicate that at the highest folate and PEG functionalized concentrations that the NS are monodispersed. The DLS zeta potential mesurments show that as NS were functionalized with increased amounts of PEG, the zeta potential were constant. Conversely, when NS were coated with increasing amounts of folate, the NS charge got increasingly more negative probably due to the deprotonation of the folate carboxylic groups. This increase in net absolute charge on the NS functionalized with 200 ug folate suggests that the NS have good stability and will resist any aggregation in aqueous solution.

As seen in Figure 4.2, plain and functionalized NS were also observed by SEM. All samples as expected showed round shaped hollow NS with narrow size distributions and no morphological differences could be seen in any samples before or after NS surface modification.

Table 4.1: Dynamic Light Scattering (DLS) Size and Zeta Potentials of 100nm SiO_2 Nanoshells (NS) in Aqueous Suspension[1].

Sample Name	Hydrodynamic Diameter (nm)	PDI	Zeta Potential (mV)
NS (No Coating)	85	0.24	-40
NS (20ug FITC)	1400	0.46	-6
NS (20ug FITC + 2ug Folate)	720	0.64	-8
NS (20ug FITC + 20ug Folate)	560	0.53	-14
NS (20ug FITC + 200ug Folate)	330	0.36	-25
NS (20ug FITC + 9ug PEG)	710	0.68	-12
NS (20ug FITC + 90ug PEG)	550	0.53	-12
NS (20ug FITC + 900ug PEG)	300	0.41	-12

[1]For all functionalized NS, the stated amount of FITC, folate, and/or PEG were the amount that was mixed during the functionalizing protocol step to 3mg of hollow NS. After the overnight reactions were completed, NS were spun down, washed, re-suspended in Milli-Q water, and analyzed by DLS. DLS results show that as folate or PEG concentration increases, there is less NS aggregation and, as folate increases, there is also higher zeta potential.

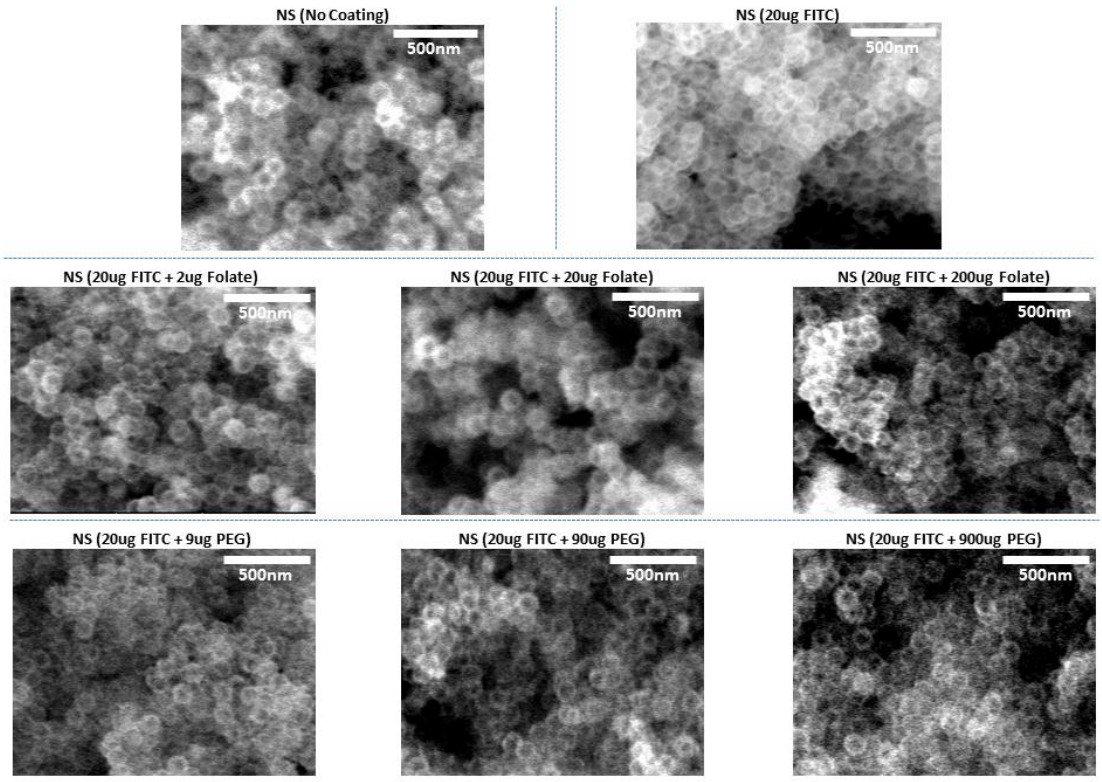

Figure 4.2: SEM Images of 100nm Nanoshells (NS) Functionalized with FITC, Folate, and/or PEG. No morphological differences can be seen before or after surface modification by SEM analysis. All SEM images were taken at 36,000x magnification.

4.3.2 Quantification of Maximum Amount of Folate on NS Surfaces

The maximum amount of folate on NS surfaces was estimated by using a weight factor equation and UV-Vis spectrophotometry to analyze the left over supernatants of three different NS batches after they were functionalized with only NHS-folate, where any folate not present in the supernatant was assumed to be exclusively functionalized on the surface of the nanoshells. As seen in Figure 4.3, it was found that as more folate was added during the reaction step, more folate was functionalized on the NS. On average, over 6,700 folate molecules were coated on an individual NS when 200 ug folate was added to the reaction, but only 2,900 folate molecules adhered to a NS when 20 ug folate was mixed in during functionalization synthesis (Figure 4.3A). Furthermore, folate molecules per area values were also determined (Figure 4.3B). For

batches produced with 200 ug folate, it was estimated that 0.03 folate molecules per nm^2 were coated on the total NS surface area. For batches functionalized with 20 ug folate, these values were lower as expected. It was found that 0.01 folate molecules per nm^2 on average were coated on the surface area of each individual NS. Contrariwise, if one is concerned that SiO_2 NS are slightly porous, and potentially folate molecules could seep into the NS core through these pores, it was calculated using a weight factor equation that only 14% of folate molecules shown in Figure 4.3A would actually be coated on an individual NS surface, while the folate molecules per area values would stay the same. 2 ug sample calculations are not being reported because UV-Vis data was below detection levels.

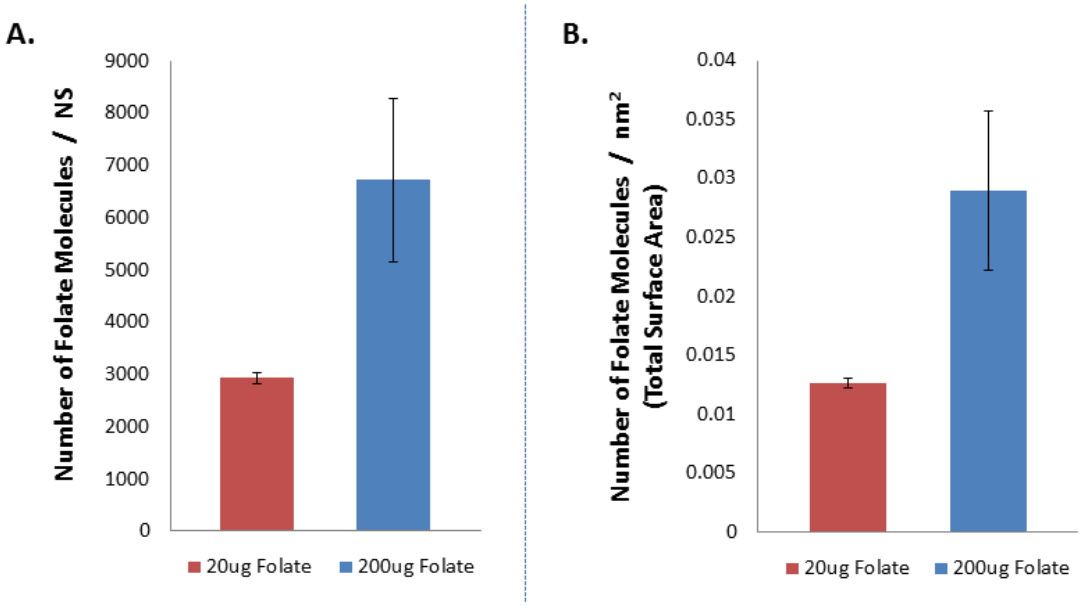

Figure 4.3: Estimated Maximum Amount of Folate Molecules and Number of Folate Molecules Per nm^2 on a Nanoshell (NS). Supernatants used to functionalize NS with 20 or 200 ug of folate were collected. Using UV Vis, amount of folate molecules functionalized on NS surfaces was calculated. A: Average number of folate molecules functionalized on an individual NS. B: Average number of folate molecules per nm^2.

4.3.3 NS HeLa Cell Adhesion Experiments and Fluorescent Microscopy Image Analysis

To evaluate the extent of target-specific cellular adhesion of folate functionalized NS, folate receptor overexpressing HeLa cervical cancer cells were used in *in vitro* cell cultures and were studied and visualized using florescent microscopy. The cells were marked with red fluorescent WGA membrane stain and blue Hoechst nuclear dye. For each cell sample, 100 ug/mL of a specific FITC/folate or FITC/PEG functionalized SiO_2 NS batch was added and allowed to incubate with cells for 24 h.

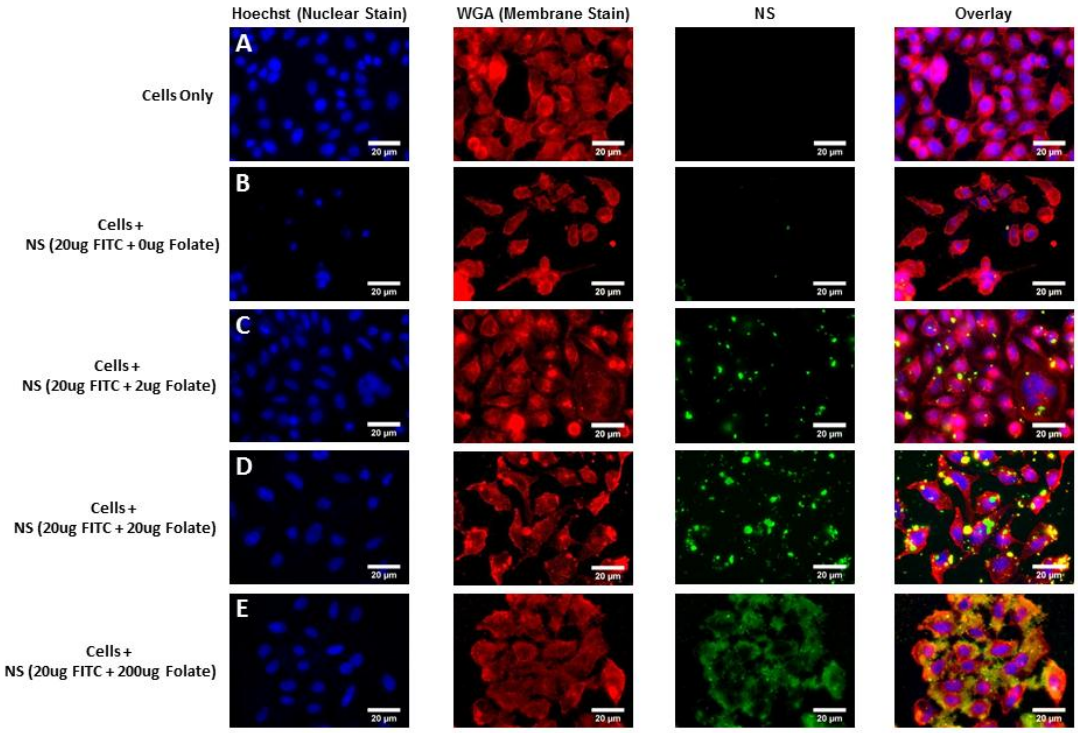

Figure 4.4: Effect of Increasing Folate Targeting Ligand on SiO_2 NS on Cellular Adhesion/Endocytosis by Fluorescent Microscopy. A: HeLa cells stained with WGA membrane stain (Red) and Hoechst nuclear stain (Blue); B: HeLa cells incubated with 100 µg/mL of NS functionalized with 20 µg FITC (Green); C: HeLa cells incubated with 100 µg/mL of NS functionalized with 20 µg FITC and 2 µg Folate; D: HeLa cells incubated with 100 µg/mL of NS functionalized with 20 µg FITC and 20 µg Folate; E: HeLa cells incubated with 100 µg/mL of NS functionalized with 20 µg FITC and 200 µg Folate. Increase in green fluorescence around cells indicates increase in NS adhesion/endocytosis.

Table 4.2: Nanoshell (NS) Cell Adhesion Fluorescence Quantification Ratio on HeLa Cells.

Sample	# of Cell Outlines	Sample Ratio[1]	SD[2]	Fluorescence Ratio[3]	Percent Fluorescence Increase[4]
Cells Only	60	0.14	0.02	-	-
Cells + NS (20ug FITC)	68	0.18	0.03	1.3	-
Cells + NS (20ug FITC + 2ug Folate)	53	0.34	0.15	2.4	140%
Cells + NS (20ug FITC + 20ug Folate)	52	0.53	0.13	3.8	280%
Cells + NS (20ug FITC + 200ug Folate)	88	0.77	0.20	5.5	450%
Cells + NS (20ug FITC + 9ug PEG)	76	0.30	0.05	2.2	120%
Cells + NS (20ug FITC + 90ug PEG)	59	0.37	0.10	2.7	170%
Cells + NS (20ug FITC + 900ug PEG)	78	0.37	0.06	2.7	170%

[1]Sample Ratio = the averaged value of the Mean Green Fluorescence (NS) divided by Mean Red Fluorescence (cells) based on each individual cell outline in a given sample set

[2]Standard Deviation (SD) = Standard Deviation of Sample Ratio

[3]Fluorescence Ratio = Sample Ratio divided by HeLa Cells Only Sample Ratio

[4]Percent Fluorescence Increase (%) = Percent Fluorescence Increase Compared to HeLa Cell Only Sample Ratio

As shown in Figure 4.4, as more folate was incorporated on the NS surface, more NS tended to bind to the surface of HeLa cervical cancer cells (Figure 4.4 A to E). Furthermore, at higher folate concentrations, the NS adhering to the cell surface appeared to be more dispersed, forming a uniform coating around cells, while NS with less folate on their surface tended to attach to cells in large bright clumps. HeLa cell samples were also prepared using similar size non-targeting PEG NS and compared to

their folate functionalized NS counterparts (Figure 4.5). Although, FR positive HeLa cervical cancer cells samples incubated with NS functionalized with increasing folate concentrations on their surfaces show increasing cell adhesion with increase folate concentration (Figure 4.5A), no increase in cell adhersion was observed with increasing PEG concentration (Figure 4.5B). These results are consistent with the increased NS cell adhesion observed with increasing folate functionalized on the NS surface being due primarily to folate-to-FR targeting.

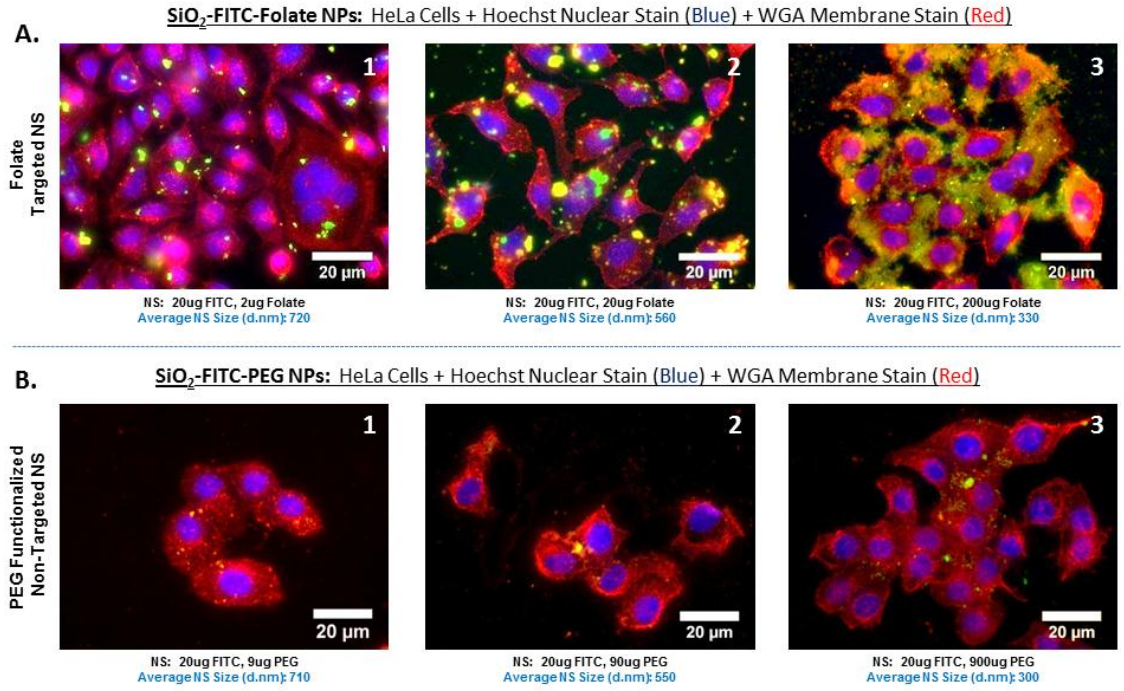

Figure 4.5: Comparison of Targeted and Non-Targeted Nanoshells (NS) Cell Adhesion/Endocytosis by Fluorescent Microscopy. HeLa cells were incubated with 100 µg/mL of targeted NS functionalized with (A.1) 20 µg FITC and 2 µg folate, (A.2) 20 µg FITC and 20 µg folate, (A.3) 20 µg FITC and 200 µg folate or non-targeted NS functionalized with (B.1) 20 µg FITC and 9 µg PEG, (B.2) 20 µg FITC and 90 µg PEG, or (B.3) 20 µg FITC and 900 µg PEG. All cells were stained with Hoescht and WGA. Average NS sizes were determined by DLS measurements.

In order to quantify and confirm that these green particle features were due to the adhesion of NS and not an optical artifact, a modified version of a previously reported fluorescent ratio analysis [61] was performed on cell outlines using the

individual red and green channel images. Briefly, the fluorescent ratio analysis was performed using Image J to first create cytoplasmic cell outlines in order to determine the extent of NS adhesion by cells. The cell outlines were based on the individual red channel images and were applied to the same location/coordinates on their green channel counterparts by using the ROI manager in Image J. The Image J analyze/measure tools were used to determine the mean fluorescent values inside the cell outlines for both the green and red channels, which in turn were used to calculate the sample ratio, i.e. mean green fluorescence divided by mean red fluorescence, of each individual outlined cell. Once the average sample ratio was determine for each set, the fluorescence ratio was calculated by taking a given sample ratio and dividing by the HeLa cells only control sample ratio, which was used as a normalization factor.

As can be seen in Table 4.3, the ratio analysis shows that HeLa cells incubated with folate functionalized NS tend to have larger fluorescence ratio than the corresponding PEG NS samples. In addition, the fluorescent values for increasing folate functionalized NS tend to grow at a fast rate, going from a value of 2.4 for NS synthesized with 2 ug of folate to 5.5 for NS synthesized with 200 ug of folate, while the fluorescent values for increasing PEG only increasing from 2.2 for NS produced using 9 ug of PEG to 2.7 for NS fabricated using 900 ug of PEG. Moreover, when the fluorescent ratios of similar sized folate and PEG NS were compared to each other, as seen in Table 4.3, it was found that folate functionalized NS were always greater than PEG NS. For example, when comparing NS functionalized with 20ug FITC and 200ug folate to NS coated with 20ug FITC and 900ug PEG, the fluorescent ratio for folate functionalized NS was 110% more intense than their similar sized PEG particles counterparts, suggest that ~ 2x more folate NS adhered to the surface of FR positive HeLa cells than their non-targeting PEG coated equivalents. Being that all cell images were obtained with identical microscopy parameters, these results imply that increased NS adhesion on the outer membrane surface of the HeLa cells is not solely due to shrinking NS size, but to folate targeting. To our knowledge, this is the first time a fluorescent ratio analysis has been used to compare nanoparticle adhesion of targeting to non-targeting nanoparticles.

Table 4.3: Differences in Nanoshells (NS) HeLa Cell Adhesion/Endocytosis between Folate NS and PEG NS Counterparts by Fluorescence Microscopy.

Sample Comparison	Percent Increase[1]
NS (20ug FITC + 2ug Folate) / NS (20ug FITC + 9ug PEG)	12%
NS (20ug FITC + 20ug Folate) / NS (20ug FITC + 90ug PEG)	41%
NS (20ug FITC + 200ug Folate) / NS (20ug FITC + 900ug PEG)	110%

[1]Results were calculated by dividing the fluorescent ratio of a HeLa cell sample incubated with folate NS by its PEG NS equivalent sample.

4.3.4 NS HeLa Cell Adhesion Experiments and Fluorescent Microscopy Image Analysis

The uptake of NS by HeLa cells was investigated by confocal microscopy. As seen in

Figure 4.6, the confocal microscope images show FR positive HeLa cancer cells incubated with NS modified with 200 ug folic acid and 20 ug fluorescein at different Z positions: (A) top, (B) middle cut between slices A & C and (C) center cell cut. These confocal images indicate that folate functionalize NS were inside the cells, as opposed

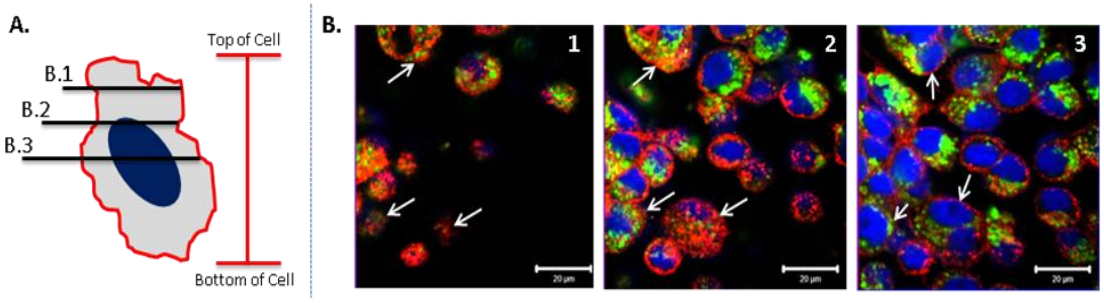

Figure 4.6: Confocal Microscopy Cross Sectional Images of Endocytosed Nanoshells (NS) in HeLa Cancer Cells. A: Schematic depicting z-stack depth of consecutive confocal cross sections (B.1 to B.3) within HeLa cancer cells. B.1-B.3: A series of confocal microscopy images of HeLa cells, stained with WGA (Red) and Hoechst (Blue), incubated with 100 µg/mL of NS functionalized with 20 µg of FITC and 200 µg folate (Green), with arrows pointing to (B.1) top of cells, (B.2) proceeding cell cross section, or (B.3) cells at their center cross section.

to being only on the cell membrane surface. To further verify folate induced endocytosis, a confocal micrscopy comparison was made between folate and PEG functionalizd NS. As shown in Figure 4.7, HeLa cells incubated with FITC/folate functionalized NS show a green fluorescent of scattered NS within the cytosol region of cells (Figure 4.7C) which is easy to observe with the blue channel off (Figure 4.7D); conversely HeLa cells treated with similar sized FITC/PEG coated NS (Figure 4.7B) exhibited very weak green fluorescent intensities within the confocal image and look very similar to control samples of HeLa cells without NS (Figure 4.7A).

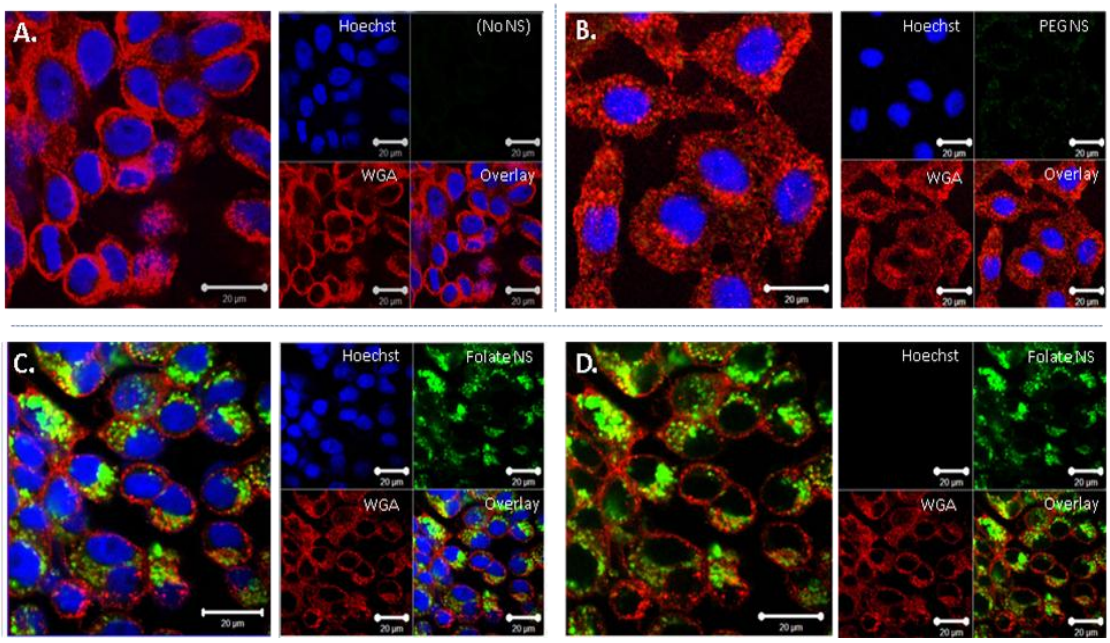

Figure 4.7: Confocal Microscopy Center Cross Sectional Images of HeLa Cells Incubated with Targeted or Non-Targeted Nanoshells (NS). A: HeLa cells, stained with WGA (Red) and Hoechst (Blue); B: : HeLa cells incubated with 100 µg/mL of non-targeted NS functionalized with 20 µg FITC and 900 µg PEG; C: HeLa cells incubated with 100 µg/mL of targeted NS functionalized with 20 µg FITC and 200 µg folate; D: Same as (C) except with blue channel turned off. Identical settings and gains were used across all microscopy images.

As with the adhesion study, a fluorescent ratio analysis was performed on confocal images in order to quantify NS cellular uptake with a minor change. Individual cell outline were again drawn out using Image J software and all outlines were based on the location of the red membrane cell stain images, but as shown in Figure 4.8, for confocal z-stacks, cell outlines were only drawn for the center cut (i.e.

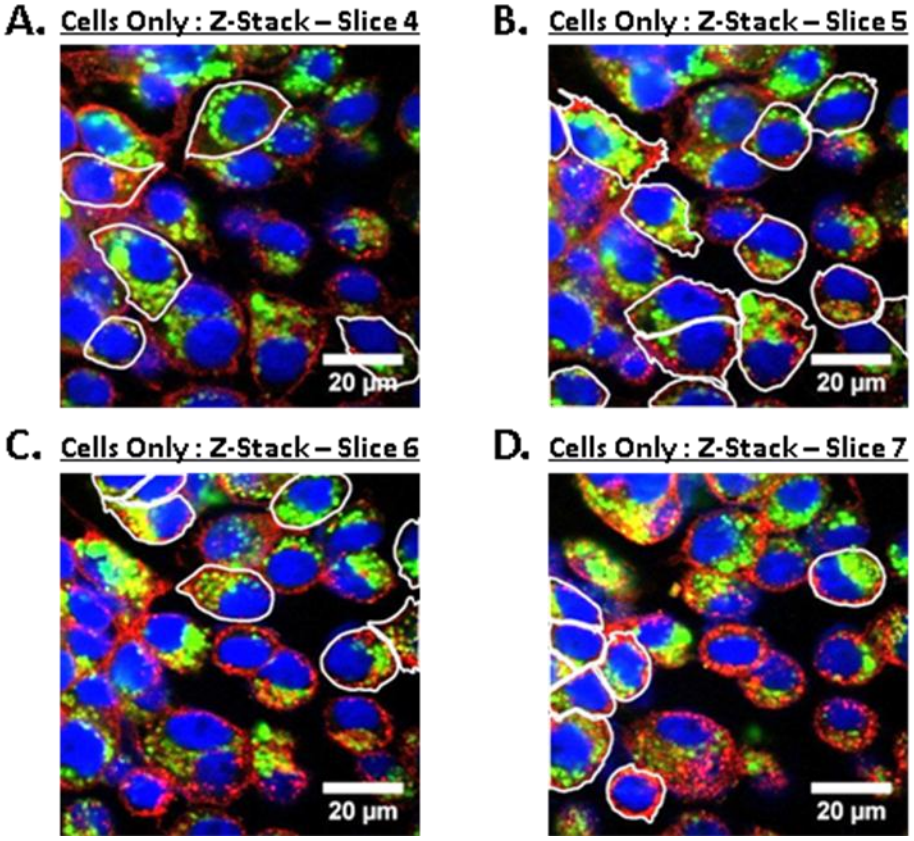

Figure 4.8: Outlining HeLa Cells from Confocal Z-Stack Images. (A) - (D) A series of consecutive confocal images showing different cells being outlined at different z-stack planes. Each individual cell was outline only once at its center cross section, which was identified as the z-stack slice where an individual cell had its largest area. All outlines were based on the location of the red membrane stain images.

biggest z-stack slice) of any individual cell to avoid outlining the same cell more than once throughout the z-stack.

Table 4.4: Quantification of Nanoshell (NS) Cell Endocytosis by HeLa Cells using Confocal Cross-Sectional Image Analysis.

Sample	# of Cell Outlines	Sample Ratio[1]	SD[2]	Fluorescence Ratio[3]	Percent Fluorescence Increase[4]
Cells Only	149	0.06	0.02	-	-
Cells + NS (20ug FITC)	108	0.04	0.03	0.8	-
Cells + NS (20ug FITC + 2ug Folate)	368	0.12	0.09	2.2	120%
Cells + NS (20ug FITC + 20ug Folate)	190	0.43	0.25	7.8	680%
Cells + NS (20ug FITC + 200ug Folate)	292	0.82	0.58	14.8	1380%
Cells + NS (20ug FITC + 9ug PEG)	100	0.08	0.11	1.5	50%
Cells + NS (20ug FITC + 90ug PEG)	217	0.18	0.25	3.3	230%
Cells + NS (20ug FITC + 900ug PEG)	115	0.03	0.01	0.6	-

[1]Sample Ratio = the averaged value of the Mean Green Fluorescence (NS) divided by Mean Red Fluorescence (cells) based on each individual cell outline in a given sample set

[2]Standard Deviation (SD) = Standard Deviation of Sample Ratio

[3]Fluorescence Ratio = Sample Ratio divided by HeLa Cells Only Sample Ratio

[4]Percent Fluorescence Increase (%) = Percent Fluorescence Increase Compared to HeLa Cell Only Sample Ratio

As can be seen in Table 4.4, NS functionalized with increasing amounts of folate tend to have larger fluorescence ratios and their values tend to be much greater than the corresponding PEG NS samples. Furthermore, the results show that the confocal imaging fluorescence ratio values for folate targeting NS increased by almost as much as 3x compared to their 2D imaging values, even while particle endocytosis is not seen in the immediate area around the cell nucleus in confocal images. These results indicate that folic acid modification not only facilitate the NS to target specific

cell surfaces, but more importantly increase the yield of cell internalization likely due to folate receptor mediated endocytosis, as particle cell internalization plays a large role in successful drug delivery. Some samples tended to have large sample ratio standard deviations, which was due to outlining all cells in a field of view and including them in the analysis, even cells that didn't appear to have any or little NS endocytosis.

Table 4.5: Differences in Nanoshells (NS) endocytosis by HeLa Cells between Folate NS and PEG NS Counterparts using Confocal Cross-Sectional Images.

Sample Comparison	Percent Increase[1]
NS (20ug FITC + 2ug Folate) / NS (20ug FITC + 9ug PEG)	46%
NS (20ug FITC + 20ug Folate) / NS (20ug FITC + 90ug PEG)	140%
NS (20ug FITC + 200ug Folate) / NS (20ug FITC + 900ug PEG)	2500%

[1]Fluorescent Ratio of a HeLa cell sample incubated with folate NS divided by Fluorescent Ratio of a HeLa cell sample incubated with PEG NS size equivalent sample.

When the fluorescent ratios of similar sized folate and PEG NS were compared to each other, it was found that folate functionalized NS were always greater than PEG NS (Table 4.5). Of particular interest was the fluorescent ratio comparison of NS functionalized with 20ug FITC and 200ug folate to NS coated with 20ug FITC and 900ug PEG, where folate functionalized NS showed 2500% increase in intensity than their similar sized PEG particles counterparts, suggesting that on average ~ 26x more folate NS were endocytosed by FR positive HeLa cells than similar sized PEG coated NS. These results are similar to previously published data by Leamon *et al* [62], which demonstrated that HeLa cells can uptake up to 30x more folate functionalized nanoparticles compared to non-targeting particles, which suggest that a fluorescent ratio analysis could be a valid quick inexpensive and usable method for quantifying and comparing NS uptake of targeting versus non-targeting nanoparticle when used in combination with confocal microscopy. As far to our knowledge, this is the first time

anyone has shown the validity of such a method. Furthermore, it should not come to a surprise that HeLa cells can uptake NS as large as 300 nm, as previous work by Rosenholm *et al* [43] has shown that folate targeted nanoparticles can be readily endocytosed by HeLa cells, even when the nanoparticle diameter is larger than 400 nm.

In addition, the number of cell outlines with a sample ratio over 1, 0.8, and 0.6 were counted and tabulated (Table 4.6). This data was collected in order to help explain why some samples had large sample ratio standard deviations, but it also demonstrates the difference between the large numbers of cells that tended to endocytose FITC/folate functionalized NS, while showing how few HeLa cells actually engulfed similar size FITC/PEG NS. As can be seen for all 3 tabulated cutoff sample ratios, as folate molecules were increased on the NS surface, the percentage of outlines over a given ratio value increases as well, while only a handful of cells at any of the 3 cutoffs show

Table 4.6: Number of Confocal Cell Outlines with a Sample Ratio over 1, 0.8, and 0.6.

Sample	# of Outlines with Value > 1	% of Outlines with Value > 1	# of Outlines with Value > 0.8	% of Outlines with Value > 0.8	# of Outlines with Value > 0.6	% of Outlines with Value > 0.6
Cells Only	0	0%	0	0%	0	0%
Cells + NS (20ug FITC)	0	0%	0	0%	0	0%
Cells + NS (20ug FITC + 2ug Folate)	0	0%	0	0%	2	0.5%
Cells + NS (20ug FITC + 20ug Folate)	7	3.7%	15	7.9%	41	22%
Cells + NS (20ug FITC + 200ug Folate)	84	29%	131	45%	159	55%
Cells + NS (20ug FITC + 9ug PEG)	0	0%	0	0%	1	1%
Cells + NS (20ug FITC + 90ug PEG)	3	1.4%	5	2.3%	10	4.6%
Cells + NS (20ug FITC + 900ug PEG)	0	0%	0	0%	0	0%

an internalization of any of PEG functionalized NS. For example, at a sample ratio cutoff value of 0.6, 159 HeLa cells (55% of all cells outline in that group) internalized enough NS functionalized with 20ug FITC and 200ug folate to get to that value, while 0 HeLa cells endocytosed enough similar size non-targeting NS coated with 20ug FITC and 900ug PEG. These results again present strong evidence about the targeting and uptake effects of folate NS by FR positive HeLa cells. Additionally, these results help explain why some sets tended to have large sample ratio standard deviations, and it was because in certain sample sets there were a fair number of cells that endocytosed NS, but also a large number that did not.

4.3.5 NS Selectivity Experiments and Image Analysis

An important aspect for developing nanoparticles for biomedical applications is their selective targeting. Particles that show non-selective uptake by cells could potentially have limited utility in biological settings. Therefore, the selectivity properties of folate functionalized NS was studied using a cellular mixture consisting of FR positive HeLa cervical cancer cells and normal HFF-1 cells. For this study, only NS functionalized with 200 ug folate and 20 ug fluorescein or 900 ug PEG and 20 ug fluorescein were studied because they should the most cell interactions in the previous experiments for their respective targeting and non-targeting sets. As can be seen in Figure 4.9, under co-culture conditions of HeLa and HFF-1 cells, folate targeted NS almost exclusively adhered to HeLa cells at high numbers (Figure 4.9C), while non-targeting similar size PEG functionalize NS only bind to a few cells (Figure 4.9B) and samples look similar to cell only co-culture conditions (Figure 4.9A). These results indicate that folate functionalized silica NS are selective and prefer HeLa cancer cells due to their elevated folate receptor expression, something that non-cancerous cells like HFF-1 cells tend to have in low levels. This ability of folate NS to be highly cancer cell selective gives them particular interesting as potential therapeutic drug delivery vehicles.

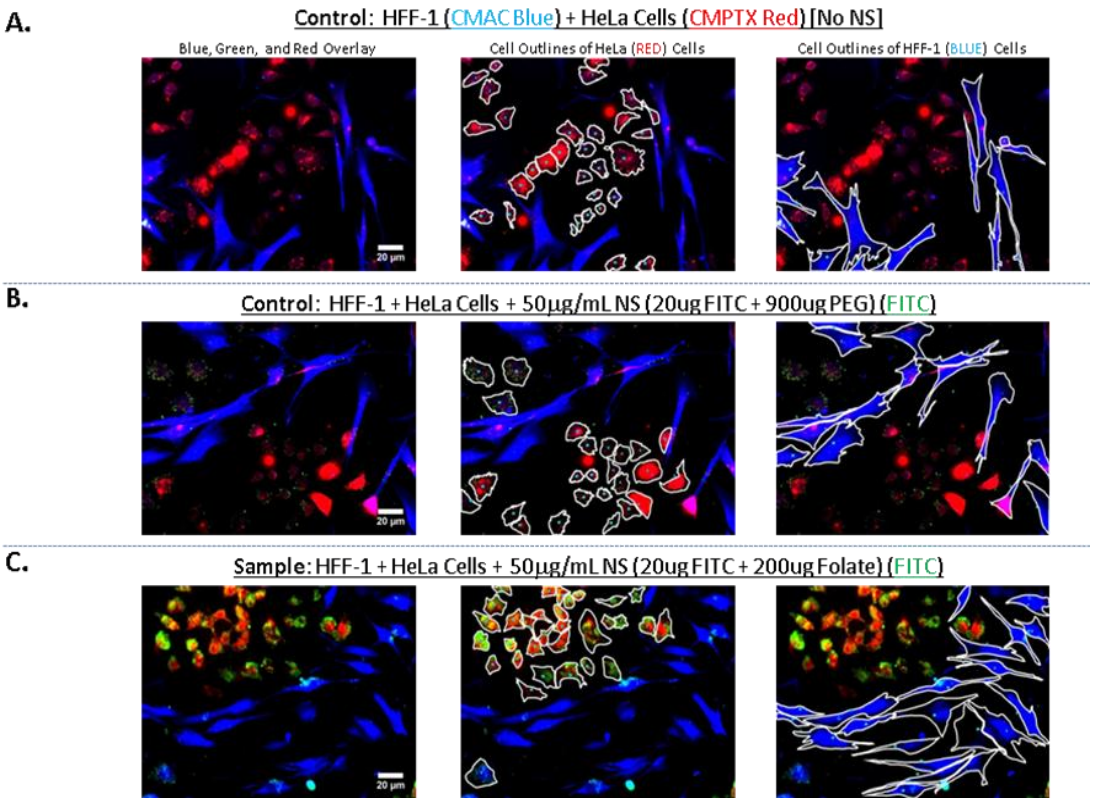

Figure 4.9: Fluorescent Microscopy Images of Differential Uptake of Non-Targeted and Targeted Nanoshells (NS) by HeLa and HFF-1 cells. A: HeLa cancer cells, stained with CMPTX (Red), and normal Human Forskin Fibroblast (HFF-1), stained with CMAC (Blue); B: HeLa and HFF-1 cells incubated with 50 µg/mL of non-targeted NS functionalized with 20 µg FITC and 900 µg PEG; C: HeLa and HFF-1 cells incubated with 50 µg/mL of targeted NS functionalized with 20 µg FITC and 200 µg folate. White markings are cell outlines used to quantify NS cell selectivity.

Moreover, the different in NS cell selectivity between folate and PEG functionalized NS was also quantified. As depicted in Figure 4.9, by using Image J two different sets of cell outlines were created; one consisting of HeLa cell outlines that were produced using the red channel image and the other for HFF-1 cell outlines that used solely the blue channel image to trace traced out HFF-1 cells. These set of outlines were then applied to the same location/coordinates on their green channel counterparts by using the ROI manager in Image J. The Image J analyze/measure tools were used to determine the mean green fluorescent values inside each of the cell outlines. These individual mean green fluorescent values were then averaged for each set. The averaged mean green fluorescence of HeLa cells to HFF-1 cells was compared

to each other in order to create a corresponding ratio for each of the three cell sample sets (co-culture cells only, cells incubated with folate functionalized NS, and cells incubated with PEG functionalized NS). The corresponding ratio for each cell set was then normalized by dividing by the cells only control corresponding ratio, thus giving the comparable fluorescent ratio. As expected, when the comparable fluorescent ratios for the similar sized folate and PEG NS were compared to each other, it was found that folate functionalized NS adhered selectively at a higher rate to HeLa cells rather than to HFF-1 cells compared PEG functionalized NS. A summary of these results can be found on Table 4.7. Furthermore, if the percent fluorescence increase values are compared to each other, folate targeted NS show an 8.01x higher preference for HeLa cells than HFF-1 normal cells when compared to non-targeting PEG particles.

Table 4.7: Quantification of Nanoshells (NS) Selective Cell Adhesion/adhesion by Fluorescence Microscopy.

Sample	# of Cell Outlines	MGF[1]	SD[2]	CR[3]	CFR[4]	PFI[5]
HeLa Cells Only	183	1928	540	1.17	-	-
HFF-1 Cells Only	151	1650	573	-	-	-
HeLa + NS (20ug FITC+200ug Folate)	248	8012	4166	2.62	2.24	124%
HFF-1 + NS (20ug FITC+200ug Folate)	191	3057	1267	-	-	-
HeLa + NS (20ug FITC+900ug PEG)	226	3862	870	1.35	1.16	16%
HFF-1 + NS (20ug FITC+900ug PEG)	139	2862	655	-	-	-

[1]Mean Green Fluorescence (MGF) = The averaged value of the Mean Green Fluorescence of each individual cell outline in a given sample set

[2]SD = Standard Deviation of Mean Green Fluorescence

[3]Corresponding Ratio (CR) = Mean Green Fluorescence of HeLa Cells Sample divided by the Mean Green Fluorescence value of HFF-1 Sample of Corresponding Set (e.g. Mean Green Fluorescence of HeLa Cells Only / Mean Green Fluorescence of HFF-1 Cells Only)

[4]Comparable Fluorescent Ratio (CFR) = Corresponding Fluorescence Ratio divided by Cells Only Corresponding Fluorescence Ratio

[5]Percent Fluorescence Increase (PFI) = Percent Fluorescence Increase Compared to Cells Only Corresponding Fluorescence Ratio

4.4 Conclusions

Hollow silica 100nm NS were functionalized with FITC and varying amounts of folic acid, a cancer targeting ligand. It was found that as the amount of folate increased on the particle surface, less NS aggregation occurred under aqueous conditions and on average approximately 6,700 individual folate molecules could be functionalized on an individual hollow nanoshell. By applying a novel fluorescent ratio analysis method on fluorescent microscopy images, it was found that folate functionalized SiO_2 NS adhered

to the surface of FR positive HeLa cervical cancer cells by a factor of 2x more than non-targeted PEG functionalized silica NS. In addition, when the same ratio analysis was applied to confocal images, roughly 26x more folate functionalized NS were discovered to be internalized by HeLa cells when compared to samples incubated with similar sized non-targeted PEG NS. Under HeLa/HFF-1 co-culture conditions, folate NS were found to be cancer cell selective, by a factor of 8x, compared to their PEG NS counterparts. The internalization and selectivity of folate functionalized NS by FR rich cancer cells make these particles promising candidates for targeted drug delivery or cancer imaging. Furthermore, it has been shown that a fluorescent ratio analysis, when used in conjunction with fluorescent and confocal microscopy, can be a quick method to distinguish nanoparticle adhesion from nanoparticle uptake and can be a simple analysis tool to quantify these parameters. This technique can potentially eliminate the need for multiple washes and lysing steps as well as the need to use multiple analytical techniques to confirm nanoparticle cell interactions.

4.5 Acknowledgments

This research was supported by NIH Nanotumor Grant (NIH Grant U54 CA 119335) and we thank the California Institute of Information Technology and Telecommunication and the Air Force Office of Scientific Research (AFOSR grant number FA9550-12-1-0381) for research support. In addition, individual student funding was provided by NIH Ruth L. Kirschstein National Research Service Award F31 Fellowship (NIH Grant No. 5F31 EB010375), NCI Research Supplements to Promote Diversity in Health Related Research Fellowship (NIH Grant No. 3U54 CA 119335–05S3), NSF—California LSAMP Bridge to the Doctorate/Louis Stokes Alliances for Minority Participation Fellowship (UCINSF Grant No. HRD0115115), and NIH—ET CURE/Specialized Cancer Center Support (NIH Grant No. 3P30 CA 023100–25S7). The Cancer Center Microscopy Core Facility at UCSD (NCI Grant No. P30 CA23100) is acknowledged for assistance in obtaining the confocal images.

Chapter 4 contents are part of a manuscript in preparation, Sandoval S., Liberman, A., Alfaro J.G., Yang J., Aschemeyer S., Trogler W.C., Kummel A.C. The dissertation author was the primary researcher and author of this work

4.6 References

1. Chan, J.M., et al., *PLGA-lecithin-PEG coreshell nanoparticles for controlled drug delivery.* Biomaterials, 2009. **30**(8): p. 1627-1634.

2. Cheng, J., et al., *Formulation of functionalized PLGA-PEG nanoparticles for in vivo targeted drug delivery.* Biomaterials, 2007. **28**(5): p. 869-876.

3. de Salamanca, A.E., et al., *Chitosan Nanoparticles as a Potential Drug Delivery System for the Ocular Surface: Toxicity, Uptake Mechanism and In Vivo Tolerance.* Investigative Ophthalmology & Visual Science, 2006. **47**(4): p. 1416-1425.

4. Davis, M.E., *The First Targeted Delivery of siRNA in Humans via a Self-Assembling, Cyclodextrin Polymer-Based Nanoparticle: From Concept to Clinic.* Molecular Pharmaceutics, 2009. **6**(3): p. 659-668.

5. Kong, G., et al., *Efficacy of Liposomes and Hyperthermia in a Human Tumor Xenograft Model: Importance of Triggered Drug Release.* Cancer Research, 2000. **60**(24): p. 6950-6957.

6. Ibsen, S., et al., *A novel nested liposome drug delivery vehicle capable of ultrasound triggered release of its payload.* Journal of Controlled Release, 2011. **155**(3): p. 358-366.

7. Bandekar, A., et al., *Antitumor efficacy following the intracellular and interstitial release of liposomal doxorubicin.* Biomaterials, 2012. **33**(17): p. 4345-4352.

8. Muthu, M.S., et al., *Theranostic liposomes of TPGS coating for targeted co-delivery of docetaxel and quantum dots.* Biomaterials, 2012. **33**(12): p. 3494-3501.

9. Kong, S.D., et al., *Magnetically Vectored Nanocapsules for Tumor Penetration and Remotely Switchable On-Demand Drug Release.* Nano Letters, 2010. **10**(12): p. 5088-5092.

10. Yang, J., J.U. Lind, and W.C. Trogler, *Synthesis of Hollow Silica and Titania Nanospheres.* Chemistry of Materials, 2008. **20**(9): p. 2875-2877.

11. Podsiadlo, P., et al., *Gold Nanoparticles Enhance the Anti-Leukemia Action of a 6-Mercaptopurine Chemotherapeutic Agent.* Langmuir, 2007. **24**(2): p. 568-574.

12. Gupta, A.K. and M. Gupta, *Synthesis and surface engineering of iron oxide nanoparticles for biomedical applications.* Biomaterials, 2005. **26**(18): p. 3995-4021.

13. Yoshida, M., et al., *Tumor local chemohyperthermia using docetaxel-embedded magnetoliposomes: Interaction of chemotherapy and hyperthermia.* Journal of Gastroenterology and Hepatology, 2012. **27**(2): p. 406-411.

14. Hocine, O., et al., *Silicalites and Mesoporous Silica Nanoparticles for photodynamic therapy.* International Journal of Pharmaceutics, 2010. **402**(1,Äì2): p. 221-230.

15. Wang, X., et al., *Perfluorohexane-Encapsulated Mesoporous Silica Nanocapsules as Enhancement Agents for Highly Efficient High Intensity Focused Ultrasound (HIFU).* Advanced Materials, 2012. **24**(6): p. 785-791.

16. Liberman, A., et al., *Hollow silica and silica-boron nano/microparticles for contrast-enhanced ultrasound to detect small tumors.* Biomaterials, 2012. **33**(20): p. 5124-5129.

17. Michalet, X., et al., *Quantum Dots for Live Cells, in Vivo Imaging, and Diagnostics.* Science, 2005. **307**(5709): p. 538-544.

18. Sharma, P., et al., *Nanoparticles for bioimaging.* Advances in Colloid and Interface Science, 2006. **123,Äì126**(0): p. 471-485.

19. Gelderblom, H., et al., *Cremophor EL: the drawbacks and advantages of vehicle selection for drug formulation.* European Journal of Cancer, 2001. **37**(13): p. 1590-1598.

20. Behlke, M.A., *Progress towards in Vivo Use of siRNAs.* Mol Ther, 2006. **13**(4): p. 644-670.

21. Zhang, Y., N. Kohler, and M.Q. Zhang, *Surface modification of superparamagnetic magnetite nanoparticles and their intracellular uptake.* Biomaterials, 2002. **23**(7): p. 1553-1561.

22. Oyewumi, M.O. and R.J. Mumper, *Influence of formulation parameters on gadolinium entrapment and tumor cell uptake using folate-coated nanoparticles.* International Journal of Pharmaceutics, 2003. **251**(1-2): p. 85-97.

23. Kukowska-Latallo, J.F., et al., *Nanoparticle Targeting of Anticancer Drug Improves Therapeutic Response in Animal Model of Human Epithelial Cancer.* Cancer Research, 2005. **65**(12): p. 5317-5324.

24. Kularatne, S.A. and P.S. Low, *Targeting of Nanoparticles: Folate Receptor*. Cancer Nanotechnology: Methods in Molecular Biology

Vol. Volume 624. 2010: Springer.

25. James, S.J., et al., *The Essentiality of Folate for the Maintenance of Deoxynucleotide Precursor Pools, DNA-Synthesis, and Cell-Cycle Progression in Pha-Stimulated Lymphocytes.* Environmental Health Perspectives, 1993. **101**: p. 173-178.

26. Ulrich, C.M., *Folate and cancer prevention: a closer look at a complex picture.* American Journal of Clinical Nutrition, 2007. **86**(2): p. 271-273.

27. Hilgenbrink, A.R. and P.S. Low, *Folate receptor-mediated drug targeting: From therapeutics to diagnostics.* Journal of Pharmaceutical Sciences, 2005. **94**(10): p. 2135-2146.

28. Campbell, I.G., et al., *Folate-Binding Protein Is a Marker for Ovarian-Cancer.* Cancer Research, 1991. **51**(19): p. 5329-5338.

29. Weitman, S.D., et al., *Distribution of the Folate Receptor Gp38 in Normal and Malignant-Cell Lines and Tissues.* Cancer Research, 1992. **52**(12): p. 3396-3401.

30. Weitman, S.D., K.M. Frazier, and B.A. Kamen, *The Folate Receptor in Central-Nervous-System Malignancies of Childhood.* Journal of Neuro-Oncology, 1994. **21**(2): p. 107-112.

31. Toffoli, G., et al., *Overexpression of folate binding protein in ovarian cancers.* International Journal of Cancer, 1997. **74**(2): p. 193-198.

32. Holm, J., et al., *Characterization of a high-affinity folate receptor in normal and malignant human testicular tissue.* Bioscience Reports, 1999. **19**(6): p. 571-580.

33. Ross, J.F., et al., *Folate receptor type beta is a neutrophilic lineage marker and is differentially expressed in myeloid leukemia.* Cancer, 1999. **85**(2): p. 348-357.

34. Bueno, R., et al., *The alpha folate receptor is highly activated in malignant pleural mesothelioma.* Journal of Thoracic and Cardiovascular Surgery, 2001. **121**(2): p. 225-233.

35. Shia, J., et al., *Immunohistochemical expression of folate receptor α in colorectal carcinoma: patterns and biological significance.* Human Pathology, 2008. **39**(4): p. 498-505.

36. Sudimack, J. and R.J. Lee, *Targeted drug delivery via the folate receptor.* Advanced Drug Delivery Reviews, 2000. **41**(2): p. 147-162.

37. Garinchesa, P., et al., *Trophoblast and Ovarian-Cancer Antigen-Lk26 - Sensitivity and Specificity in Immunopathology and Molecular-Identification as a Folate-Binding Protein.* American Journal of Pathology, 1993. **142**(2): p. 557-567.

38. Ross, J.F., P.K. Chaudhuri, and M. Ratnam, *Differential regulation of folate receptor isoforms in normal and malignant tissues in vivo and in established cell lines. Physiologic and clinical implications.* Cancer, 1994. **73**(9): p. 2432-2443.

39. Wang, X., et al., *Differential Stereospecificities and Affinities of Folate Receptor Isoforms for Folate Compounds and Antifolates.* Biochemical Pharmacology, 1992. **44**(9): p. 1898-1901.

40. Lu, Y.J., et al., *Folate receptor-targeted immunotherapy of cancer: mechanism and therapeutic potential.* Advanced Drug Delivery Reviews, 2004. **56**(8): p. 1161-1176.

41. Lu, Y.J. and P.S. Low, *Folate-mediated delivery of macromolecular anticancer therapeutic agents.* Advanced Drug Delivery Reviews, 2002. **54**(5): p. 675-693.

42. Brannon-Peppas, L. and J.O. Blanchette, *Nanoparticle and targeted systems for cancer therapy.* Advanced Drug Delivery Reviews, 2004. **56**(11): p. 1649-1659.

43. Rosenholm, J.M., et al., *Targeting of Porous Hybrid Silica Nanoparticles to Cancer Cells.* ACS Nano, 2008. **3**(1): p. 197-206.

44. Wu, J., Q. Liu, and R.J. Lee, *A folate receptor-targeted liposomal formulation for paclitaxel.* International Journal of Pharmaceutics, 2006. **316**(1–2): p. 148-153.

45. Zhang, L., et al., *Uptake of folate-conjugated albumin nanoparticles to the SKOV3 cells.* International Journal of Pharmaceutics, 2004. **287**(1–2): p. 155-162.

46. Werner, M.E., et al., *Folate-targeted nanoparticle delivery of chemo- and radiotherapeutics for the treatment of ovarian cancer peritoneal metastasis.* Biomaterials, 2011. **32**(33): p. 8548-8554.

47. Li, L., et al., *Biofunctional self-assembled nanoparticles of folate-PEG-heparin/PBLA copolymers for targeted delivery of doxorubicin.* Journal of Materials Chemistry, 2011. **21**(39): p. 15288-15297.

48. Zauner, W., N.A. Farrow, and A.M.R. Haines, *In vitro uptake of polystyrene microspheres: effect of particle size, cell line and cell density.* Journal of Controlled Release, 2001. **71**(1): p. 39-51.

49. Chithrani, B.D., A.A. Ghazani, and W.C.W. Chan, *Determining the Size and Shape Dependence of Gold Nanoparticle Uptake into Mammalian Cells.* Nano Letters, 2006. **6**(4): p. 662-668.

50. Zhang, Y., N. Kohler, and M. Zhang, *Surface modification of superparamagnetic magnetite nanoparticles and their intracellular uptake.* Biomaterials, 2002. **23**(7): p. 1553-1561.

51. Thurn, K.T., et al., *Endocytosis of titanium dioxide nanoparticles in prostate cancer PC-3M cells.* Nanomedicine : nanotechnology, biology, and medicine, 2011. **7**(2): p. 123-130.

52. Hu, F.X., K.G. Neoh, and E.T. Kang, *Synthesis and in vitro anti-cancer evaluation of tamoxifen-loaded magnetite/PLLA composite nanoparticles.* Biomaterials, 2006. **27**(33): p. 5725-5733.

53. Yin Win, K. and S.-S. Feng, *Effects of particle size and surface coating on cellular uptake of polymeric nanoparticles for oral delivery of anticancer drugs.* Biomaterials, 2005. **26**(15): p. 2713-2722.

54. Davda, J. and V. Labhasetwar, *Characterization of nanoparticle uptake by endothelial cells.* International Journal of Pharmaceutics, 2002. **233**(1,Äì2): p. 51-59.

55. Miller, C.R., et al., *Liposome-Cell Interactions in Vitro: Effect of Liposome Surface Charge on the Binding and Endocytosis of Conventional and Sterically Stabilized Liposomes.* Biochemistry, 1998. **37**(37): p. 12875-12883.

56. Trogler, W.C., et al., *Hollow silica nanospheres for drug delivery and gene transfer.* 2009: p. 76 pp.

57. Martinez, H.P., et al., *Hard shell gas-filled contrast enhancement particles for colour Doppler ultrasound imaging of tumors.* Medchemcomm, 2010. **1**(4): p. 266-270.

58. Wagner, A.J., et al., *Cellular Interaction of Different Forms of Aluminum Nanoparticles in Rat Alveolar Macrophages.* The Journal of Physical Chemistry B, 2007. **111**(25): p. 7353-7359.

59. Bihari, P., et al., *Optimized dispersion of nanoparticles for biological in vitro and in vivo studies.* Part Fibre Toxicol, 2008. **5**: p. 14.

60. Pal, A.K., et al., *Screening for Oxidative Stress Elicited by Engineered Nanomaterials: Evaluation of Acellular DCFH Assay.* Dose Response, 2012. **10**(3): p. 308-30.

61. Yang, J., et al., *Red-luminescent europium (III) doped silica nanoshells: synthesis, characterization, and their interaction with HeLa cells.* J. Biomed. Opt., 2011. **16**(6): p. 066012/1 - 066012/8.

62. Leamon, C.P. and P.S. Low, *Folate-mediated targeting: from diagnostics to drug and gene delivery.* Drug Discov Today, 2001. **6**(1): p. 44-51.

Chapter 5. Conclusions and Future Directions

5.1 Conclusions

5.1.1 Europium Doped Silica NS

Photoluminescent Eu^{3+} has been doped into 100 nm and 200 nm diameter sizes of silica NS through a sol-gel synthesis route and use of a polymer bead template. Removing the polymer cores by calcination produces silica NS containing less than 3 % mole europium, which emits a strong narrow red emission line at 615 nm. The long lifetime of the rare earth ion facilitates studies by 2-P microscopy. Two-photon microscopy of the europrium(III) doped NS show little interaction with HeLa cells in culture media; however, when the NS were coated with PEI they acquired a high positive charge and bound to the outer surface of HeLa cancer cells with minimal endocytosis. The ability to control nanoparticle location (cell surface vs. interior) is valuable in biosensing and drug delivery studies.

5.1.2 Europium Doped Titania NS

Uniform-sized Eu^{3+} doped hollow titania NS were fabricated by a new method using $Ti(O\text{-}t\text{-}Bu)_4$ and $Eu(NO_3)_3$ with amine functionalized polystyrene beads serving as templates. Removal of the polystyrene core by calcining led to increased luminescence from Eu^{3+} doped hollow nanoshells as the hydrated titania sol gel partially transformed to the anatase doped phase. Up to 1.1% Eu^{3+} could be introduced before the nanoshells lost their structural integrity, and the doped NS exhibited a strong narrow red photoluminescence emission at 617 nm upon UV excitation of the titania. Europium doped hollow NS were functionalized with PEI, which changed the NS surface charge from negative to positive. The positively charged doped NS where shown by two-photon microscopy to bind to the outer surface of HeLa cervical cancer cells with minimal endocytosis. Since the Eu^{3+} luminescence does not photobleach, the UV

absorbing titania acts as an antenna to enhance emission, and the luminescent state is amenable to imaging by 2-P techniques, these NS may be especially useful in the field of biological imaging, diagnostics, and/or therapeutics.

5.1.3 Folate Functionalized Silica NS

Hollow silica 100nm NS were functionalized with FITC and varying amounts of folic acid, a cancer targeting ligand. It was found that as the amount of folate increased on the particle surface, less NS aggregation occurred under aqueous conditions and on average approximately 7,000 individual folate molecules could be functionalized on an individual hollow nanoshell. By applying a novel fluorescent ratio analysis method on fluorescent microscopy images, it was found that folate functionalized SiO_2 NS adhered to the surface of FR positive HeLa cervical cancer cells by a factor of 2x more than non-targeted PEG functionalized silica NS. In addition, when the same ratio analysis was applied to confocal images, roughly 26x more folate functionalized NS were discovered to be internalized by HeLa cells when compared to samples incubated with similar sized non-targeted PEG NS. Under HeLa/HFF-1 co-culture conditions, folate NS were found to be cancer cell selective, by a factor of 8x, compared to their PEG NS counterparts. The internalization and selectivity of folate functionalized NS by FR rich cancer cells make these particles promising candidates for targeted drug delivery or cancer imaging. Furthermore, it has been shown that a fluorescent ratio analysis, when used in conjunction with fluorescent and confocal microscopy, can be a quick method to distinguish nanoparticle adhesion from nanoparticle uptake and can be a simple analysis tool to quantify these parameters. This technique can potentially eliminate the need for multiple washes and lysing steps, as well as the need to use multiple analytical techniques to confirm nanoparticle cell interactions.

5.2 Future Directions

5.2.1 NS Payload Encapsulation and Possible Drug Delivery Peripheral Instrumentation

In order to fully take advantage of the unique structure of SiO_2 and TiO_2 NS, payload and drug realease studies need to be invistigated. We have recently publish *ex vivo* [1] and *in vivo* mice studies [2] showing that silica NS can be filled with perfluorocarbon gas and can be used as ultrasound imaging agents. Although, these publications show that the hollow nanoshell interior can be used to encapsulate a payload material for diagnostic purposes, studies still need to be performed to demonstrate that a drug can be entrapped in the NS core and released over time in order to show therapy application potential. Ideally, a study would involve: (1) developing an encapsulation method, (2) quantifying the drug loading efficiency, (3) performing a drug release study showing controlled NS drug release over time, (4) demonstrating improved cytotoxicity of drug loaded NS over free drug *in vitro* and (5) finally *in vivo*.

5.2.2 Folate Functionalization of Titania NS

A method to functionalize folate on to the surface of TiO_2 NS can be developed. This targeting mechanism can potential not only help titania NS in drug delivery and diagnostic applications, but also in their conceivable use as photodynamic therapy agents. By selectively binding cancer cells, TiO_2 NS can potentially reduce the amount of damage caused to normal tissue while they are excited under ultra violet light during photodynamic therapy sessions.

5.2.3 Folate NS Targeting In Vivo Properties

Being that different parameters exist under *in vivo* conditions that are difficult to reproduce under cell culture conditions, such as blood flow and muscle movements, folate targeting NS need to be studied under *in vivo* conditions in order to proof that their targeting capabilites are applicable in such enviornments. In addition, in order to

make these NS extremly useful, an *in vivo* drug realease study should also be investigated.

5.2.4 Incorporation of Iron Oxide in NS Structure for Potential Use Magnetic Therapy

An interesting potential area of use for these NS is in magnetic resonance imaging (MRI). In order to make this possible, SiO_2 and TiO_2 NS would have to be superparamagnetic. This can potentially be accomplished by first swelling the polystyrene templates in an anhydrous ethanol/organic solvent solution and then by adding iron oxide, which is insoluble in alcohols, to the swelled polystyrene templates [3]. The polystyrene template can then be contracted to its original size by adding another polar organic solvent, which consequently, would cause the iron oxide to be embedded within the polystyrene sphere [3]. Tetramethylorthosilicate or titanium(IV) *t*-butoxide can then be added to the polystyrene templates, in order to start the sol-gel reaction to create SiO_2 or TiO_2 NS, respectively. The particles can then be collected, dried in a vacuum oven, and heated to 500°C in order harden the NS wall and calcined to remove the polystyrene core. Being that iron oxide has a melting temperature of 1,566°C, it will stay trap inside the resulting hollow nanoshells, making the NS superparamagnetic.

5.3 References

1. Martinez, H.P., et al., *Hard shell gas-filled contrast enhancement particles for colour Doppler ultrasound imaging of tumors.* Medchemcomm, 2010. **1**(4): p. 266-270.

2. Liberman, A., et al., *Hollow silica and silica-boron nano/microparticles for contrast-enhanced ultrasound to detect small tumors.* Biomaterials, 2012. **33**(20): p. 5124-5129.

3. Trogler, W., C. (2460 Cordero Road, Del Mar, CA, 92093, US), et al., *Hollow Silica Nanospheres and Methods of Making Same*. 2009, THE REGENTS OF THE UNIVERSITY OF CALIFORNIA (1111 Franklin Street, 5th FloorOakland, CA, 94607-5200, US); TROGLER, William, C. (2460 Cordero Road, Del Mar, CA, 92093, US); ESENER, Sadik, C. (743 San Mario Drive, Solana Beach, CA, 92075, US); MESSMER, Davorka (8746 Villa La Jolla

Drive, #51La Jolla, CA, 92037, US); LIND, Johan, Ulrik (Victor Bendix Gade 14, Copenhagen E, DK-2100, DK); POHAKU, Kristina (4031 Casita Way, San Diego, CA, 92115, US); YANG, Jian (7675 Palmilla Drive, Apt. 6304San Diego, CA, 92122, US).